UNIVERSITÀ DEGLI STUDI DI FIRENZE
Facoltà di Scienze Matematiche, Fisiche e Naturali

Tesi di laurea in fisica

EXPLORING THE PHASE DIAGRAM OF A DISORDERED BOSE GAS

Lorenzo Gori

Relatore: Prof. Giovanni Modugno
Correlatore: Prof. Massimo Inguscio
Correlatore esterno: Prof. Jörg Müller

CONTENTS

Introduction

In the last years Bose-Einstein condensates (BECs) in optical lattices have been the subject of intense experimental and theoretical research. The enormous interest shown in such area of physics relies on the fact that BECs widen the horizons of the quantum world as they are observable macroscopic objects that behave according to the laws of quantum mechanics.

Moreover, Bose-Einstein condensates are extremely versatile tools as they can be manipulated by means of off-resonant laser light. The possibility to trap ultracold quantum gases in ideal periodic potentials, that is without defects and lattice vibrations, allowed to experimentally study fundamental problems related to condensed matter physics, like, for instance, the quantum theory of transport of electrons in metals.

Besides allowing to control with accuracy the optical lattice parameters, such for instance its depth and spacing, the laser light offers the possibility to introduce and control disorder in the system. The versatility of ultracold Bose gases is further highlighted by the fact that the interactions between the atoms that constitute a BEC can be controlled as well.

This thesis work deals with the experimental investigation of the behaviour of a ^{39}K BEC in an optical lattice when both a controlled disorder, by means of a quasi-periodic optical lattice, and a controlled interaction, by means of Feshbach resonance, are applied to the system. This study was carried out at the European Laboratory for Nonlinear Spectroscopy of the University of Florence. In addition, part of the thesis work has consisted in the design and realization of an original portable spectrum analyzer, to help in the daily practice of running a complex laser cooling experiment. This part of the work was done during a six months stage at the Niels Bohr Institute of Physics in Copenhagen. The thesis is organized as follows:

In the first chapter we introduce, from a theoretical point of view, the main features of Bose-Einstein condensates, focusing in particular on the possibility to tune their interactions. Moreover, we give a basic physical description of periodic and disordered optical potentials.

In the second chapter we introduce the disordered Bose-Hubbard model describing the behaviour of a gas of interacting particles in a disordered optical lattice. We present an overview of the possible quantum phases of the system and in particular we describe how, depending on the interplay between disorder and interaction, the zero-temperature system undergoes phase transitions, driven by quantum fluctuations, from conductive to insulating regimes and vice-versa.

In the third chapter, after briefly introducing the main theoretical features at the base of the homebuilt laser portable spectrum analyzer we describe in a detailed way how it has been designed, mounted and tested.

In the last chapter we present first a description of the experimental setup that has been implemented in order to investigate the quantum phases theoretically described in chapter 2. We then describe the measurements, performed at different levels of disorder and interaction strength, of the momentum distribution of the atomic sample. Such measurements provide a first evidence of the phase diagram of the disordered bosons both in the regime of weak and strong interactions.

CHAPTER 1

Bose-Einstein condensates in optical lattices

Contents

In this first chapter we will introduce the two main ingredients that have been employed in the experiments described in this thesis, that is Bose-Einstein condensates and optical potentials. In section 1.1 we will report a brief theoretical introduction on the physics of the BECs, particularly focusing on the possibility to tune their interactions, while in section 1.2 we will describe how both periodic and disordered potentials can be implemented by means of laser light and how the behaviour of a BEC is affected by such optical potentials.

1.1 Bose-Einstein condensation

Bose-Einstein condensation is a pure quantum phenomenon that occurs as a macroscopic number of identical bosons in thermal equilibrium occupy the same quantum (ground) state. As a result, quantum effects become relevant on a macroscopic scale. This condition, which was predicted in 1925 by A. Einstein and S. N. Bose [1][2], was experimentally achieved in 1995 in a dilute gas of ^{87}Rb atoms [3]. Later on, many other atomic samples, among which ^{39}K, have been brought to the condensation[1].

In order to qualitatively understand how the phase transition to the Bose-Einstein condesate occurs, let's consider (figure 1.1a) a gas of atoms in thermal equilibrium with a thermal velocity v and a density $n = d^{-1/3}$, d being the mean distance between the particles. At room temperature T_R, the atoms of the dilute gas are point-like particles and can therefore be spatially distinguished (classical phase). At lower temperatures (figure b), the wave-like behaviour of matter must be taken into account and the spatial extension of a particle can be suitably described in terms of its De Broglie wavelength:

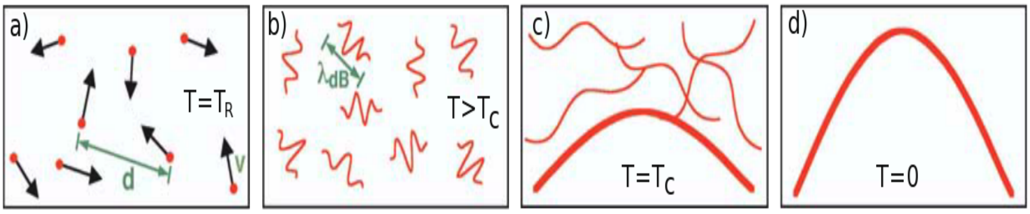

Figure 1.1: Phase transition to the BEC. (**a**) Classical distinguishable particles d apart at room temperature T_R. (**b**) Spatial extension λ_{DB} of the wave functions associated to the particles at $T < T_c$. (**c**) wave functions overlap ($\lambda_{DB} \approx d$): a macroscopic fraction of undistinguishable bosons start condensing at $T = T_c$. (**d**) Giant wave of matter (pure BEC) at $T = 0$. Figure adapted from [4].

$$\lambda_{DB} = \frac{h}{\sqrt{2\pi\, m k_B T}} \tag{1.1}$$

---

[1] The other samples that have been condensed are ^{23}Na, ^{7}Li, H, ^{85}Rb, ^{4}He*, ^{41}K, ^{133}Cs, ^{174}Yb and ^{52}Cr.

where m is the mass of the atoms, T is the gas temperature and h and k_B are respectively the Planck and Boltzmann constants. As the temperature of the system decreases, the width λ_{DB} of the wave function associated to the particles increases according to 1.1[2]. For low enough temperatures (figure c), when $\lambda_{DB} \approx d$, the wave functions start overlapping and consequently the particles are not distinguishable any longer.

Depending on the quantum nature of the particles, i.e. whether fermionic (half-odd integer spin) or bosonic (integer spin), two different phenomena can occur as the gas is cooled down below a critical temperature T_c. Fermions, in agreement with the Pauli exclusion principle, occupy different energy levels starting from the ground state and with increasing energy (degenerate Fermi gas). Bosons, which conversely may occupy the same position and the same single-particle state, form a macroscopic matter wave oscillating in phase as a unique coherent object (BEC). Ideally, for $T = 0$ (figure d), all the particles fall in the ground state and a pure Bose-Einstein condensate without any thermal component is formed.

It is important to note that Bose-Einstein condensation is a pure quantum phenomenon as it is driven only by quantum statistics which gives rise to a sort of effective potential[3], attractive in the case of bosons (while repulsive in the case of fermions). As a matter of fact this phase transition does not depend on the interactions between particles that, instead, may reduce the quantum effects and eventually lead to the destruction of the BEC.

The qualitative description of the Bose-Einstein condensation just shown can be made more quantitative in terms of the *phase-space density* $n\lambda_{DB}^3$, which is a parameter that describes the degree of quantum-mechanical behaviour of the system. For a system of non interacting particles (ideal Bose gas) the BEC phase transition can be analytically shown [5] to occur when

$$n\lambda_{DB}^3 = 2.612 \tag{1.2}$$

---

[2] Note that this is in agreement with the Heisenberg principle as the reduction in the particle velocity uncertainty at low temperatures results in a increase in its position uncertainty, that is in its De Broglie wavelength.

[3] It's not a real potential since it depends on temperature.

For a gas of ^{87}Rb at room temperature and pressure of 1 Atm, $n\lambda_{DB}^3 \approx 10^{-8}$, that is eight orders of magnitude lower than the condition 1.2 for the phase transition[4]. In principle, such a condition could be satisfied both by increasing the density n and by decreasing the temperature T, being $\lambda_{DB} \propto T^{-1/2}$ (see equation 1.1). Nevertheless, for normal densities, at sufficiently low temperatures all the known interacting systems, with the exception of helium, become solid (see the P-T phase diagram of figure 1.2, on the left). In order to avoid such an undesired transition to the solid phase, very dilute samples[5] have to be employed and, consequently, the atoms have to be cooled down to very low temperatures. In figure 1.2 (on the right) a plot of the De Broglie wavelength λ_{DB} (blue line) as a function of the temperature T is shown together with the mean inter-particle distance $d \simeq 200\,\mathrm{nm}$ (red line) corresponding to a typical obtainable experimental density ($n \simeq 10^{14}\,\mathrm{cm}^{-3}$).

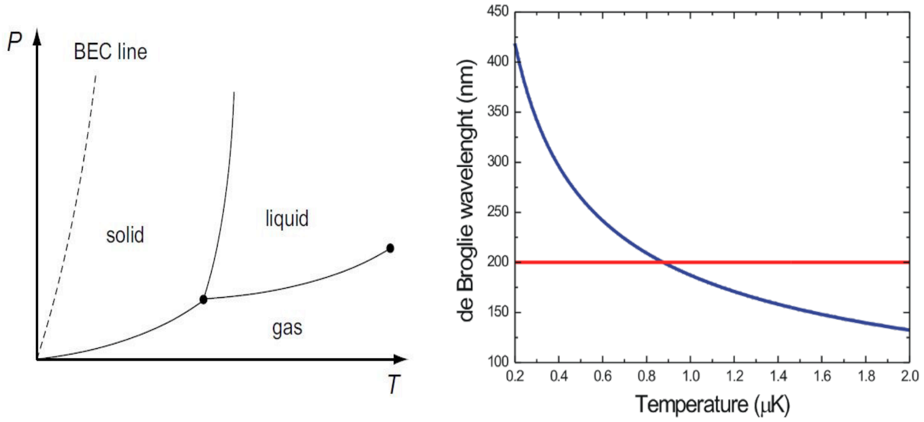

Figure 1.2: (**left**) P-T phase diagram showing the bounderies between the gaseous, liquid and solid phases. The dashed line corresponds to the BEC phase transition for an ideal gas. Figure taken from [6]. (**right**) De Broglie wavelength λ_{DB} (blue line) as a function of the temperature T and mean inter-particle distance $d \simeq 200\,\mathrm{nm}$ (red line) corresponding to a density $n \approx 10^{14}\,\mathrm{cm}^{-3}$. The intersection of the two lines corresponds to a critical temperature $T_c \lesssim 1\,\mu\mathrm{K}$.

---

[4] The experimental steps to cool down the atoms and therefore to increase the phase space density up to the order of unity are described in section 4.1.

[5] Note that the lower the pressure, the lower the probability of inelastic three-body collisions and the higher the lifetime of the metastable Bose-condensed phase.

For such a dilute gas the critical temperature T_c - corresponding to the intersection of the two lines - is of the order of $1\,\mu$K or even less.

1.1.1 BEC of an ideal trapped gas

In the experiments the BEC is always produced in a confining external potential, either magnetic or optical (see subsection 1.2). In this subsection we will thus briefly discuss the main features of a system of N non interacting identical bosons subject to a 3D anisotropic harmonic potential $V_{ext} = \sum_{i=x,y,z} \frac{1}{2} m\omega_i^2 x_i^2$ (ω_i being the frequency trap along the i direction) which well approximates the experimental confining potentials. In particular here we will limit ourselves to report the physical quantities of interest – such as the number of condensed atoms $N_0(T)$ and the condensate density distribution $n(\boldsymbol{x})$ – referring the reader to [7] for their derivation.

As for the *condensate fraction*, it depends on the temperature T as follows

$$\frac{N_0(T)}{N} = \left(1 - \frac{T}{T_c}\right)^3 \tag{1.3}$$

where the critical temperature T_c is given by $T_c \simeq \frac{\hbar\omega_{ho}}{k_B} N^{1/3}$, $\omega_{ho} = (\Pi_i \omega_i)^{1/3}$ being the geometric average of the trapping frequencies. It is interesting to note that the result 1.3 differs from the known case of a bosonic gas in a box for the exponent equal to 3 instead of 3/2. A plot of eq. 1.3 is shown in figure 1.3 where the condensate fraction for a Bose gas in the box is also reported as a comparison. As mentioned in the previous subsection, at the critical temperature T_c, a finite number of particles starts condensing; as the temperature decreases, this number increases to the extent that at $T = 0$ all the N bosons occupy the harmonic ground state.

In the fully condensed state at $T = 0$, the wave function of the N-particle system is given by the product of the ground state wave functions (normalized

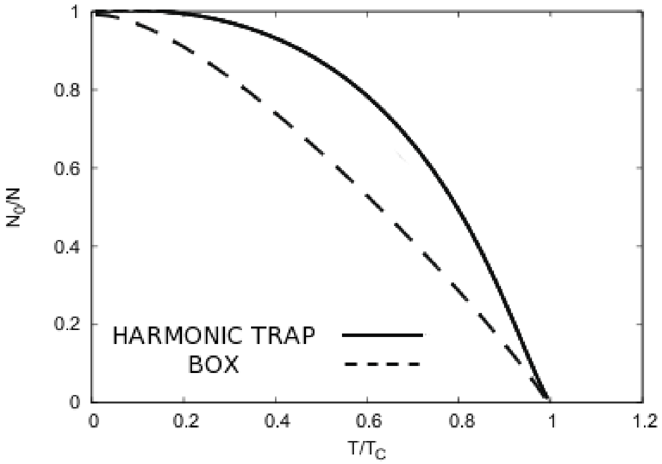

Figure 1.3: Condensate fraction as a function of the temperature for a gas of non interacting bosons in a 3D harmonic potential (dashed line) and in a box (continuos line). Below the critical temperature T_c a finite number of particles occupies the ground state (BEC phase transition). Figure adapted from [8].

to 1) of the single-particle harmonic oscillator[6]

$$\phi_0(\boldsymbol{x}) = (\sqrt{\pi}\, a_{ho})^{-3/2}\, e^{-1/2 \sum_i (x_i/a_{ho})^2} \qquad \text{with} \qquad a_{ho} = \sqrt{\hbar/m\omega_{ho}} \tag{1.4}$$

a_{ho} being the harmonic oscillator length, i.e. the width of the gaussian function ϕ_0. An important consequence of the macroscopic quantum behaviour of the BEC is that the quantum probability distribution $|\phi_0|^2$ is strictly related to the BEC density distribution[7] as

$$n_0(\boldsymbol{x}) = N_0\, |\phi_0(\boldsymbol{x})|^2 \tag{1.5}$$

which is a quantity that is measurable in the experiments.

As compared with the BEC confined in a box, which shows a phase transition only in momentum space[8], the condensation for a gas confined in a

---

[6] Note that since we are assuming that the N identical particles are not interacting, i.e. indipendent, the energy of the whole system is simply given by the sum of the energy of the single particles - which for the harmonic oscillator is $\epsilon_n = \sum_i (n_i + 1/2)\hbar\omega_i$ - and the total wave function, by the product of their wave functions $\phi_0(\boldsymbol{x})$.

[7] Note that the density distribution 1.5 satisfies the normalization condition for which the total number of condensed atoms is $N_0 = \int d\boldsymbol{x} |n_0|^2$.

[8] A BEC in a box is delocalized all over the volume, meaning that in coordinate space it can't be distinguished by the non condensed component.

harmonical trap occurs with a narrowing of the density distribution both in momentum and coordinate space.

According to the Ginzburg-Landau theory [5], the density distribution 1.5 of the ground state can be thought of as an *order parameter* that describes the degree of symmetry of the system. Such an order parameter, which is zero for $T > T_c$ (disordered phase), becomes non-zero for $T < T_c$ (ordered BEC phase) as a result of a spontaneous symmetry breaking[9]. From a mathematical point of view, the BEC phase transition is classified as a *continuous phase transition* since the order parameter $n_0(\boldsymbol{x})$ – whose dependance on T is contained in N_0 – varies in a continuous way around T_c (see figure 1.3).

1.1.2 BEC of an interacting trapped gas

So far the interactions between particles have been neglected and only the problem of the ideal Bose gas – for which the thermodynamic behaviour around T_c is completely governed by quantum statistics – has been considered. In order to correctly describe the behaviour of real systems, interactions have to be taken into account and the theory of many-body systems has to be employed. In this subsection the wave equation describing the behaviour of an interacting BEC – the so-called *Gross-Pitaevskii equation* [9][10][11] – will be shown reporting the conditions under which this can be derived from the many-body theory.

In dilute cold gases[10] only binary collisions are relevant and the two-body interaction potential $v(\boldsymbol{x}-\boldsymbol{x'})$ can be written in terms of a contact pseudo-potential as:

$$v(\boldsymbol{x}-\boldsymbol{x'}) = g\,\delta(\boldsymbol{x}-\boldsymbol{x'}) \qquad \text{with} \qquad g = \frac{4\pi\hbar^2}{m}\,a \tag{1.6}$$

where a is the scattering length. The *scattering length*, which is positive in

---

[9] The symmetry breaking is spontaneous as it occurs without the action of any external force but only by changing the temperature.

[10] The diluteness condition for a cold gas is $d \gg a$, that is the mean inte-particle distance d has to be much greater than the range a of the two body potential.

the case of repulsive interactions and negative in the case of attractive ones[11], is the only relevant parameter when describing the collisional properties of a system at very low energies (refer to subsection 1.1.3 for details).

At very low temperatures ($T \approx 0$), when a macroscopic number of atoms is condensed in the ground state (i.e. $N_0 \gg 1$), a *mean field* approach[12] can be used and the energy associated to the BEC wave function Ψ_0 turns out to be

$$E[\Psi_0] = \int d\boldsymbol{x} \left[\frac{\hbar^2}{2m} |\nabla \Psi_0(\boldsymbol{x}, t)|^2 + V_{ext}(\boldsymbol{x}) |\Psi_0(\boldsymbol{x}, t)|^2 + \frac{g}{2} |\Psi_0(\boldsymbol{x}, t)|^4 \right] \quad (1.7)$$

where the first term is the kinetic energy E_{kin}, the second one the potential energy E_{pot} and the third one the interaction energy E_{int}[13]. Minimizing the energy 1.7 with respect to infinitesimal variations of Ψ_0, yields the *Gross-Pitaevskii equation* (GPE):

$$i\hbar \frac{\partial}{\partial t} \Psi_0(\boldsymbol{x}, t) = \left[-\frac{\hbar^2}{2m} \nabla^2 + V_{ext}(\boldsymbol{x}) + g |\Psi_0(\boldsymbol{x}, t)|^2 \right] \Psi_0(\boldsymbol{r}, t) \quad (1.8)$$

As a consequence of interactions the wave equation 1.8 shows a non linear term in the condensate order parameter Ψ_0. Note that in absence of this term, which describes the condensate self-interaction, the GP equation reduces to the linear Schrödinger equation, characterized by the density distribution 1.5.

The stationary solutions of eq. 1.8 can be obtained by using the ansatz $\Psi_0(\boldsymbol{x}, t) = e^{-i\mu t/\hbar} \psi_0(\boldsymbol{x})$, where μ is the condensate *chemical potential*[14]. By

---

[11] In the following only positive a will be considered since for $a < 0$ a condensate is stable only for a very small number of atoms. As a matter of fact, above a certain critical number, the condensate collapses due to three-body inelastic collisions caused by the attractive interaction.

[12] According to the mean field theory, the many-body system of N interacting particles, which is very difficult to solve exactly, can be replaced by a one-body problem by treating the bosons collectively i.e. in terms of the single order parameter Ψ_0.

[13] Note that the quantity E_{rel}=E_{kin}+E_{int}, which is called *release energy*, is the energy available during the ballistic expansion of the condensate, when the trap potential V_{ext} is switched off (see section 2.2).

[14] Multiplying eq. 1.9 by $\psi_0^*(\boldsymbol{x})$ and integrating in $d\boldsymbol{x}$, yields $\mu = E/N + E_{int}/N$ ($E = E_{kin} + E_{pot} + E_{int}$ being the total energy of eq. 1.7): the condensate chemical potential, thus, differs from the total energy per particle E/N by the quantity E_{int}/N; the latter term being related to the fact that the GPE is not linear.

substituting this expression in eq. 1.8 we get the *time-indipendent GPE*

$$\left[-\frac{\hbar^2}{2m}\nabla^2 + V_{ext}(\boldsymbol{x}) + g|\psi_0(\boldsymbol{x})|^2\right]\psi_0(\boldsymbol{x}) = \mu\psi_0(\boldsymbol{x}). \tag{1.9}$$

Thomas-Fermi approximation

The time-independent GPE can be analytically solved in the limit of strong interactions, that is when $N\,a \gg a_{ho}$ and the interaction term $g|\Psi_0(\boldsymbol{x})|^2$ dominates on the kinetic one. By neglecting the term $-\frac{\hbar^2}{2m}\nabla^2$ (*Thomas-Fermi approximation*), the differential eq. 1.9 becomes an algebraic equation from which we get the condensate density distribution

$$n_0(\boldsymbol{x}) = |\psi_0(\boldsymbol{x})|^2 = \frac{1}{g}[\mu - V_{ext}(\boldsymbol{x})] \tag{1.10}$$

valid for $\mu > V_{ext}(\boldsymbol{r})$. For an harmonic confining potential the density distribution 1.10 assumes the shape of an inverted *parabola*:

$$n_0(\boldsymbol{x}) = \frac{\mu}{g}\left[1 - \sum_i \left(\frac{x_i}{R_i^{TF}}\right)^2\right] \qquad \text{with} \qquad R_i^{TF} = \sqrt{\frac{2\mu}{m\omega_1^2}} \tag{1.11}$$

R_i^{TF} being the *Thomas-Fermi radius* in the i direction. Figure 1.4 shows how the repulsive interaction between atoms causes a broadening of the condensate density distribution.

1.1.3 Tuning the interaction: Feshbach resonances

As mentioned in the previous subsection, in a bosonic gas at low temperatures the effective interaction between atoms can be characterized by a single quantity, the scattering length a. In this subsection we will show how it is possible to tune the intensity of the scattering length, and thus the intensity of the interactions[15], by means of Feshbach resonances. First studied in nuclear physics [12][13][14], Feshbach resonances later on became important in atom physics [15][16][17] as they offer the possibility to tune the interactions in a controlled way simply by changing a magnetic field.

---

[15] We remind that the type of interaction is determined by the sign of the scattering length, $a > 0$ resulting in repulsive interactions, while $a < 0$ in attractive ones.

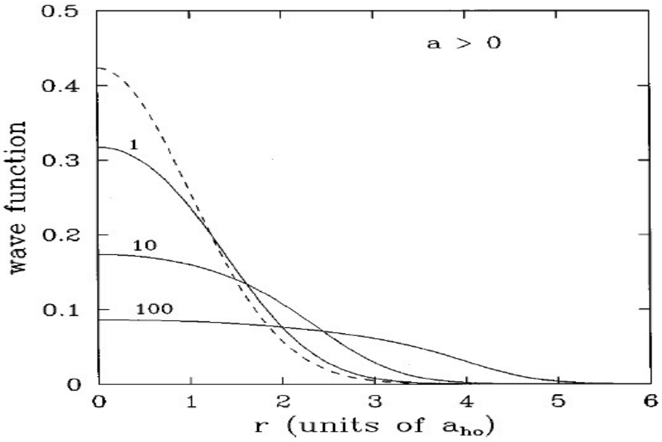

Figure 1.4: BEC density distribution for several positive values of the scattering length a. For $a = 0$ (dashed line) the BEC density distribution has a narrow gaussian shape. As a increases the repulsive interactions cause a broadening of the density distribution, which in the strongly interacting regime is approximately an inverted parabola (Thomas Fermi approximation). Note that the edges of the parabolic distribution are actually smoothed since in these regions the kinetic energy term dominates on the interaction energy one. Figure adapted from [7].

In order to describe the basic idea of Feshbach resonance, we consider (see figure 1.5) two diatomic molecular potential curves, $V_{op}(R)$ (ground state) and $V_{cl}(R)$ (excited state), corresponding to two spin configurations for atoms[16]. For large internuclear distances R, the potential $V_{op}(R)$ corresponds to the energy of the two free atoms[17] (dashed line), which is chosen here as energy reference ($V_{op}(\infty) = 0$). As the two atoms collide with a very small incident energy E_{inc}, the level $V_{op}(R)$ - called *open channel* - is energetically accessible for a collisional process. The other potential $V_{cl}(R)$, which is not accessible (*closed channel*), may however have a bound molecular state close to 0. If now the two atoms have the possibility to make a (temporary) transition to this bound molecular state, then their scattering cross section

---

[16] In priciple, a molecule has several potential curves corresponding to the different hyperfine and Zeeman levels. For simplicity, we consider here only one excited state, which is appropriate for an isolate resonance.

[17] Neglecting the Zeeman effect, the energy at $R \to \infty$ is exclusively determined by the sum of the hyperfine energies of the two free atoms.

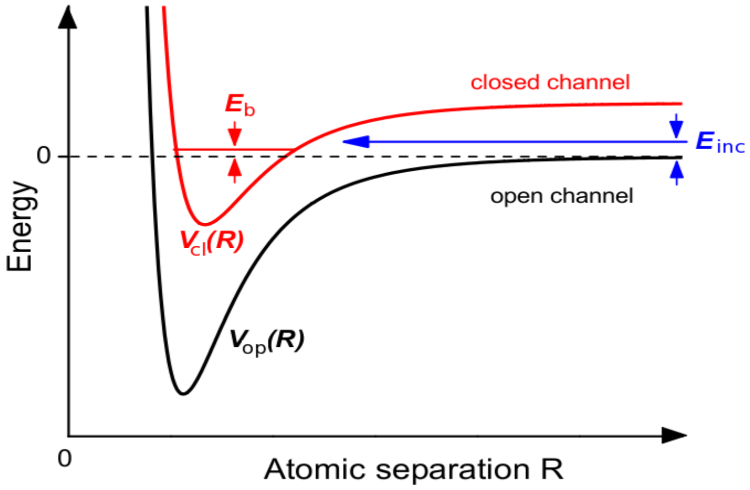

Figure 1.5: Basic model for Feshbach resonances. The scattering resonance occurs when two atoms colliding at energy E_{inc} in the open channel $V_{op}(R)$, resonantly couple to a molecular bound state with energy E_b, supported by the closed channel potential $V_{cl}(R)$. The relative energy of the two levels is controlled via magnetic field when the corresponding magnetic moments are different. Figure adapted from [18].

can extremely increase. The (Feshbach) resonance may indeed take place as the energy level of the closed channel can be tuned, with respect to the open one, by varying a magnetic field. As a matter of fact, provided that the states corresponding to the two channels have different magnetic moments, i.e. they have a different response (Zeeman shift) to the applied magnetic field B, this one can be tuned in such a way that the energy E_b of the bound molecular state approaches E_{inc}.

Near a Feshbach resonance, the magnetic field dependance on the scattering length a is given by [19]

$$a(B) = a_{bg}\left(1 - \frac{\Delta}{B - B_0}\right) \tag{1.12}$$

where B_0 is the *resonance center*, Δ the *resonance width* and a_{bg} the *background scattering length*, i.e. the scattering length far from the resonance. A plot of the scattering length a as a function of the magnetic field B is reported in figure 1.6. The figure shows the ^{39}K resonance at $B_0 \simeq 400\,\mathrm{G}$, that

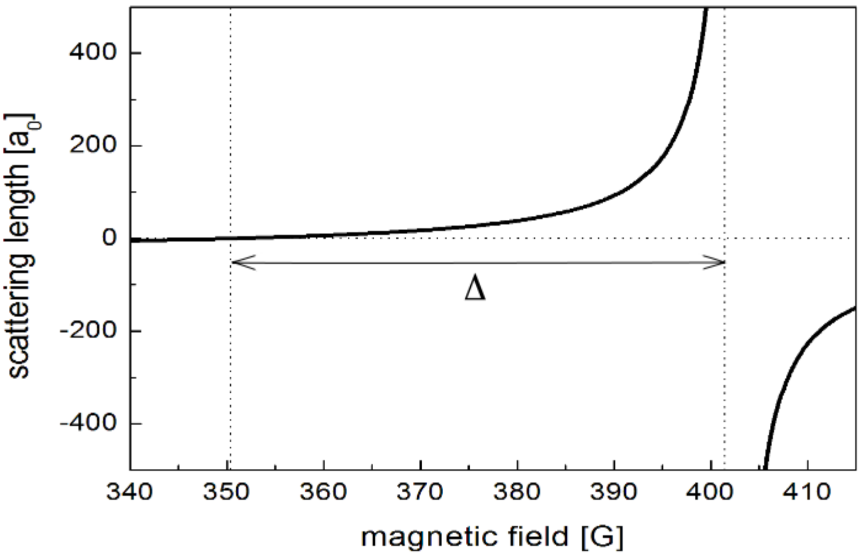

Figure 1.6: Magnetic field dependence of the scattering length between the ^{39}K Feshbach resonance at $B_0 \simeq 400\,\mathrm{G}$ and the zero-crossing $B_{zc} \simeq 350\,\mathrm{G}$. Note that the small ratio a_{bg}/Δ ($\approx \frac{1}{2}\,a_0/G$) allows to annul the interactions of a ^{39}K BEC with high degree of accuracy. Figure adapted from [20].

is also used in our experiment[18].

An important point of a Feshbach resonance is the *zero-crossing magnetic field* $B_{zc} = B_0 + \Delta$, i.e. the value of B at which a vanishes. The behaviour of the scattering length in proximity of B_{zc}, as derived by eq. 1.12, is given by

$$a(B) = \frac{a_{bg}}{\Delta}(B - B_{zc}) \qquad \text{for} \qquad B \to B_{zc} \tag{1.13}$$

The parameter that is important in order to control the interaction around the value $a = 0$, is the ratio a_{bg}/Δ: the smaller this ratio, the better the accuracy for tuning the interaction. For the resonance shown in figure, whose width is $\Delta \simeq 52\,\mathrm{G}$ and $a_{bg} \simeq -29\,a_0$ (a_0 being the Bohr radius), the sensitivity around $B_{zc} = 350\,\mathrm{G}$ is $da/dB \simeq 0.56\,a_0/G$. This means that with a stability, for instance, of 1 G for the magnetic field, the interactions of the BEC can be nulled with an uncertainty of about half a Bohr radius.

---

[18] As shown in section 4.1 the resonance at $B_0 \simeq 400\,\mathrm{G}$ is accessible when the BEC is in the substate $|F = 1, m = 1>$, where F and m respectively label the hyperfine and Zeeman levels of the ^{39}K ground state.

1.2 Optical potentials

In the first section the basic features of the Bose-Einstein condensate have been introduced. This system represents an ideal tool for the study of many fundamental problems of matter physics as its quantum effects are macroscopically observable and the main parameters of such a system can be "easily" controlled by means of laser light. After briefly discussing how neutral atoms can be trapped by optical dipole forces, in this section we will focus on the role that periodic and disordered optical potentials play in the context of BEC theory. Since a system of ultracold bosonic atoms in a optical lattice can be thought of as a *quantum simulator* for ideal condensed matter systems (e.g. electrons in crystals without impurities and vibrations), the theory of single particles in periodic potentials will be recalled (subsection 1.2.1). In subsection 1.2.2 then, the laser techniques used to produce disordered lattices – which better reproduce the imperfections of real systems – will be described.

Optical dipole forces

One of the main ways to trap and confine a gas of neutral atoms is to use optical dipole potentials[19]. The conservative dipole potentials are based on the interaction between the atomic electric dipole moment $\boldsymbol{d}$, induced by an electric field $\boldsymbol{E}$, and the field itself, namely $V_{dip} = -\frac{1}{2} < \boldsymbol{d} \cdot \boldsymbol{E} >$. It can be shown [21] that if the (laser) light interacting with the neutral atoms is far-off resonance – i.e. the detuning $\Delta = \omega - \omega_0$ between the field frequency ω and the atomic resonance frequency ω_0 is much larger than the atomic radiative linewidth Γ – then the *dipolar potential* can be expressed as follows

$$V_{dip}(\boldsymbol{x}) = \frac{3\pi c^2}{2\omega_0^3} \frac{\Gamma}{\Delta} I(\boldsymbol{x}) \tag{1.14}$$

---

[19] Besides optical traps, there are other two ways to capture neutral atoms: via *radiation-pressure* and via *magnetic trap potentials*. The formers, operating with laser light near resonance, are dissipative and are used to cool thermal atoms down to $T \approx 10\,\mu$K. The latter ones, are conservative and with typical trap depths of the order of $100\,mK$. Note that when Feshbach resonances are employed to tune the interactions, as in our case, magnetic traps can not be used, as they would be affected by the Feshbach magnetic field.

c being the speed of light in vacuum and $I(\boldsymbol{x}) = |\boldsymbol{E}(\boldsymbol{x})|^2$ being the light intensity, which in general will be position-dependent. Moreover, under the same assumption, the *scattering rate* due to the far-detuned photon absorption (and subsequent spontaneous reemission) by the atoms, turns out to be

$$\Gamma_{sc}(\boldsymbol{x}) = \frac{3\pi c^2}{2\hbar\omega_0^3}\left(\frac{\Gamma}{\Delta}\right)^2 I(\boldsymbol{x}) \tag{1.15}$$

Equations 1.14 and 1.15 show that:

- *Red detunings* ($\Delta < 0$) yield attractive interactions ($V_{dip}(\boldsymbol{x}) < 0$), meaning that the light intensity maxima correspond to the potential minima. Conversely, for *blue detunings* ($\Delta > 0$), the light intensity maxima correspond to the potential maxima, as the interaction is repulsive ($V_{dip}(\boldsymbol{x}) > 0$).
- $V_{dip} \propto I/\Delta$ whereas $\Gamma_{sc} \propto I/\Delta^2$; This means that for the optical trap to be efficient, both Δ and I must be suitably large, in such a way that the scattering rate Γ_{sc} is negligible with respect to the trap potential V_{dip}, and at the same time V_{dip} is sufficiently high.

In the experiments, dipole traps are produced by using red-detuned gaussian laser beams that are focused by suitable lenses on pre-cooled[20] atoms (see figure 1.7 on top). These ones undergo an attractive force towards the beam focus (intensity maximum) corresponding to a minimum of the potential V_{dip}. The cylindrically shaped trap produced by such a laser beam is usually well approximated by a 3D harmonic potential with a trapping frequency along the radial direction $\omega_r \propto \sqrt{V_0}/w_0$ ($V_0 = V_{dip}(0)$ being the *trap depth* and w_0 being the *waist* of the gaussian laser beam) much higher than that along the beam direction[21].

---

[20] Since optical dipole traps rely on an interaction with far-detuned light (i.e. large Δ), in agreement with eq. 1.14 their typical depths are relatively low (usually below 1 mK).

[21] Note that in order to suitably confine the atoms also in the beam direction, usually two crossed focused laser beams are used [22]. This configuration provides a quasi-isotropic confinement with a trapping frequency along the beams directions only $\sqrt{2}$ times smaller than that in the orthogonal one.

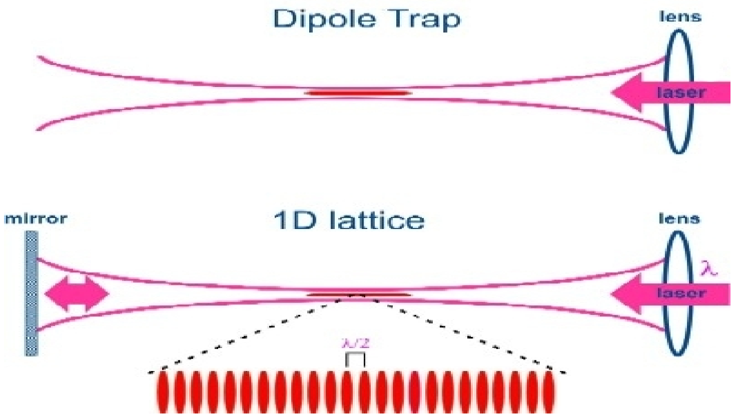

Figure 1.7: (**top**) Optical dipole trap. Neutral atoms are captured by a red detuned focused laser beam which produces a cylindrically shaped dipole potential with high confinement along the radial direction. (**bottom**) 1D optical lattice. The stationary wave resulting from the interference with the retro-reflected beam, produces an array of 2D disk-like trapping potentials with spacing $d = \lambda/2$.

1.2.1 Optical lattices

The scheme just shown for the optical trap can be easily developed to build a periodic optical potential, i.e. an *optical lattice*. The idea (see figure 1.7 on bottom) is to retro-reflect a laser beam with a mirror in such a way that a standing wave, resulting from the interference of the two counter-propagating beams, forms. Formally, if we call $\boldsymbol{E}_1$ and $\boldsymbol{E}_2$ the sinusoidal fields associated to the two counter-propagating beams – supposed to have same wave number $k = 2\pi/\lambda$, same modulus E_0 and same polarization – then the time-averaged interference pattern is given by $I(x) = |\boldsymbol{E}_1 + \boldsymbol{E}_2|^2 = I_0\, cos(kx)^2$ with $I_0 = 2E_0^2$. Replacing this expression in eq. 1.14 yields the interaction potential exerted by the stationary wave on the atoms, i.e.

$$V_{latt}(x) = V_0\, cos^2(kx) \qquad \text{with} \qquad V_0 = \frac{3\pi c^2}{2\omega_0^3}\,\frac{\Gamma}{\Delta}\, I_0 \tag{1.16}$$

This perfect sinusoid constitutes an optical lattice with period $d = \lambda/2$ and depth V_0, which is usually expressed in terms of recoil energies[22] as the di-

---

[22] The recoil energy $E_r = \frac{\hbar^2 k^2}{2m}$ is the kinetic energy with which an atom initially at rest recoils when it absorbs a photon with momentum $\hbar k$. This energy can also be thought

mensionless quantity

$$s = \frac{V_0}{E_r} \qquad \text{with} \qquad E_r = \frac{\hbar^2 k^2}{2m} \tag{1.17}$$

The potential minima (if $\Delta < 0$, otherwise the maxima) can be used to trap[23] the atoms with axial confining frequency $\omega_x \propto \sqrt{V_0}/\lambda$ very high, for each lattice site.

As shown in figure 1.8, $2D$ and $3D$ optical lattices can also be produced by superimposing 2 or 3 orthogonal pairs of counter-propagating laser beams. For a $2D$ optical lattice (a), the atoms are trapped to an array of tightly confining $1D$ potential tubes, whereas in the $3D$ case (b) the optical lattice can be approximated by a $3D$ simple cubic array of tightly confining harmonic-oscillator potentials at each lattice site.

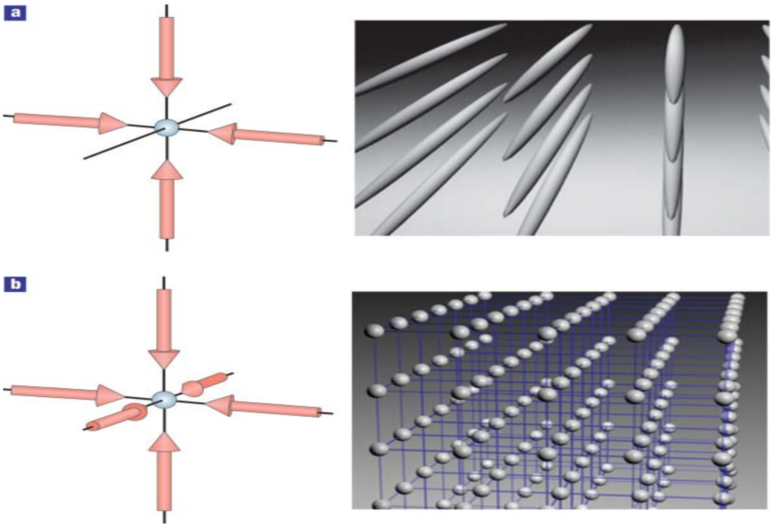

Figure 1.8: (**a**) $2D$ optical lattice: array of 1D potential tubes. (**b**) $3D$ optical lattice: 3D simple cubic array of harmonic oscillator potentials. Figure taken from [23].

---

of as the ground state energy $E = \frac{\hbar^2 \pi^2}{2m\, d^2}$ of a particle confined within a 1D-box of length $d = \lambda/2$, i.e. the lattice spacing.

[23] The trapping of the atoms in the optical lattice takes place provided that they are cold enough, i.e their energy $k_B T \ll V_0$.

The Bloch theorem

Let's now consider the theory – extensively developed in the context of solid state matter for electrons in crystals [24] – of a single particle in a periodic potential. Such a theory can be used to describe the behaviour of a non interacting BEC – which as seen in subsection 1.1.1 can be thought of as a single object – in an optical lattice.

In the 1D case, which we will consider for simplicity, the stationary *Schrödinger equation* for a single particle moving in a periodic potential $V_{latt}(x) = V_{latt}(x + d)$, is

$$H\psi(x) = \left(-\frac{\hbar^2}{2m}\frac{\partial^2}{\partial x^2} + V_{latt}(x)\right)\psi(x) = E\psi(x) \tag{1.18}$$

According to the *Bloch theorem* the solutions of eq. 1.18 are plane waves e^{iqx} modulated by a function $u_{n,q}(x)$ that has the same periodicity of the potential, i.e

$$\psi_{n,q}(x) = e^{iqx}\, u_{n,q}(x) \qquad \text{with} \qquad u_{n,q}(x) = u_{n,q}(x + d) \tag{1.19}$$

The eigenvalues $E_n(q)$ and the corresponding eigenfunctions $\psi_{n,q}(x)$ of the Hamiltonian H are labelled by two quantum numbers: n, that is the *band index* and q, that corresponds to the *quasi-momentum* $\hbar q$[24]. For a given q, there are many solutions $E_n(q)$, identified by the index n.

The periodicity of the direct lattice induces a periodicity also in the *reciprocal lattice*, whose elementary cells – called Brillouin zones – are equally spaced with period $G = 2\pi/d$. Due to such periodicity in the reciprocal space, only the *first Brillouin zone* (ranging from $q = -G/2$ to $q = G/2$) is relevant: out of it the following relations for $E_n(q)$ and $\psi_{n,q}(x)$ hold:

$$E_n(q + G) = E_n(q) \qquad \text{and} \qquad \psi_{n,q+G}(x) = \psi_{n,q}(x) \tag{1.20}$$

Thus for a given n, $E_n(q)$ is a continuous function periodic in q, commonly referred to as *energy band*. This term arises from the fact that the periodicity

---

[24] As compared with the momentum p for a free particle ($V_{latt}(x) = 0$), due to the not complete invariance of the potential $V_{latt}(x)$, $\psi_{n,q}(x)$ is not an eigenfunction of the momentum operator and thus the quasi-momentum $\hbar q$ is not its expectation value.

of the potential $V_{latt}(x)$ affects the energy spectrum in such a way that some zones are allowed (energy bands) and other are forbidden (energy gaps).

By using a perturbative approach, the eigenvalues $E_n(q)$ of 1.18 can be obtained [25] in the limit of weak potential – for which the corresponding wavefunctions $\psi_{n,q}(x)$ are nearly plane waves – and in the limit of strong potentials, for which the corresponding wavefunctions are localized in the lattice sites (see tight binding model in subsection 1.2.1). Figure 1.9 shows,

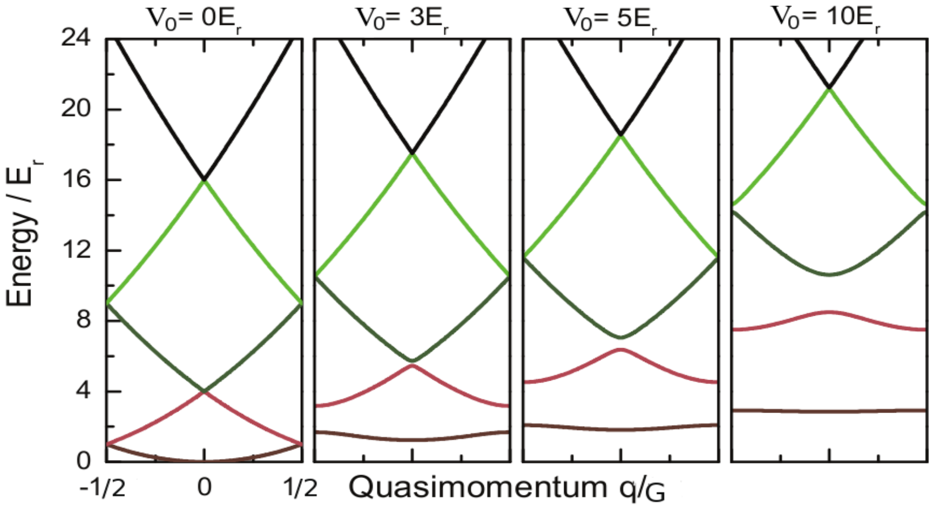

Figure 1.9: Lowest five Bloch energy bands $E_n(q)$ for increasing potential depths V_0. The higher the depth V_0, the higher the energy gap and the lower the energy band width. Note that as $E_n(q)$ is a periodic function only the first Brillouin zone, is considered. Figure adapted from [26].

in a *reduced-zone scheme*, the lowest five Bloch energy bands $E_n(q)$ for increasing potential depths V_0. Note that for $V_0 = 0$ (free particle), $E_n(q)$ corresponds to a parabola reduced to the first Brillouin zone and there are no energy gaps. As the depth V_0 increases the energy gap increases and the energy width decreases.

Tight-binding model

As mentioned previously, as the the potential depth V_0 increases, the Bloch waves – which in the weak potential limit are nearly plane waves –

become more and more localized around the lattice sites. In this regime of strong potential, which is known as *tight binding regime*, it is thus convenient to express the Bloch wavefunction for a given n as a sum of orthogonal and normalized set of wavefunctions maximally localized at each lattice site:

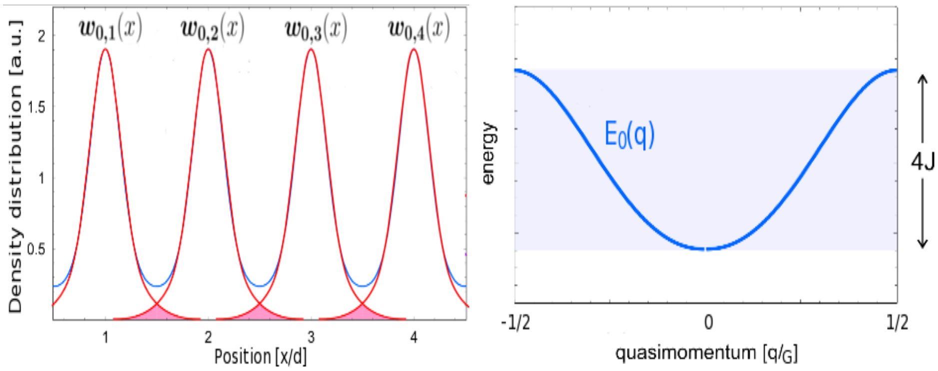

Figure 1.10: (**left**) Density distributions for the localized Wannier functions $w_{0,j}(x)$ (red) and for the extended Bloch wave function (blue) in the tight-binding limit. The overlap defining the tunneling coupling J is highlighted in red. (**right**) Lowest energy band $E_0(q)$ in the first Brillouin zone. Note that the width of the band is $4J$.

$$\psi_{n,q}(x) = \sum_{j=-\infty}^{j=\infty} e^{ix_j q}\, w_n(x - x_j) \tag{1.21}$$

where $w_{n,j}(x)$ is the so-called *Wannier function* – usually well approximable with a gaussian function – localized at the site x_j. In this tight-binding approximation only the overlap integral

$$J = -\int dx\, w_n^*(x) \left[-\frac{\hbar^2}{2m}\nabla^2 + V_{latt}(x) \right] w_n(x + d) \tag{1.22}$$

between the Wannier functions of neighboring sites is considered. Such an overlap is highlighted in red in figure 1.10 (on the left) where the density distributions for the localized Wannier functions (red) and for the extended Bloch wave function (blue), are shown. The quantity J, also referred to as *tunneling energy*, represents thus the probability for a particle to jump from one lattice site to a neighbor one.

As for the energy spectrum, in the limit of high potential depths V_0, the energy bands are narrower and the energy gap between the first and second band is quite large (see figure 1.9). Since the resulting excitation probability to higher bands is very small, only the lowest energy band $E_0(q)$ is usually considered (see figure 1.10 on the right). Such an energy band is totally determined by the tunneling energy J, being related to it as

$$E_0(q) = E_0 - 2Jcos(qd) \tag{1.23}$$

where E_0 is the energy at the center of the band, whose width is $\Delta E_0 = 4J$.

Dynamics in an optical lattice

In this subsection we will review the main features related to the dynamics of a Bloch wawefunction in the presence of an external field[25], as described by the *semiclassical model*. It is possible to demonstrate [25] that the velocity as a function of the quasimomentum q for a particle in the band n, i.e. the *Bloch velocity*, is given by:

$$v_n(q) = \frac{1}{\hbar} \frac{\partial E_n(q)}{\partial q} \tag{1.24}$$

Note that $v_n(q)$, which is strictly related to the first derivative of the band energy $E_n(q)$, approaches 0 at the band edges where $E_n(q)$ is flat (see figure 1.9). In agreement with the semiclassical model, we will assume that the external force F_{ext} acting on the system varies slowly on the scale length d of the periodic potential, and that it is weak enough not to induce inter-band transitions (i.e. $n = cost$). Under these assumptions F_{ext} has the only effect of changing the particle mean position x and the quasimomentum $\hbar q$, without affecting the energy spectrum of the system, set by the lattice potential V_{latt}. In particular, the temporal evolution of x and q are:

$$\dot{x} = \frac{1}{\hbar} \frac{\partial E_n(q)}{\partial q} \; ; \qquad\qquad \hbar \dot{q} = F_{ext} \tag{1.25}$$

---

[25] Besides the gravity force, which gives rise to the famous Bloch oscillations, a typical example of external field is that of the harmonic trapping potential needed to confine the atoms in every experiment.

where the first equation is simply a restatement of 1.24. As for the second equation, we observe that the effect of the external force is to change the quasimomentum: this is the analogy of the *second Newton's law* of dynamics with the only difference that the quasimomentum $\hbar q$ and the external force F_{ext} respectively replace the momentum p and the total force acting on the system (the latter being implicitly included in the energy spectrum E_n). By using both equations 1.25, one gets $\ddot{x} = \frac{\partial v_n(q)}{\partial q}\dot{q} = \frac{1}{\hbar}\frac{\partial^2 E_n(q)}{\partial q^2} F_{ext}$. This relation can be thought of as the second Newton's law of dynamics if one identifies the quantity

$$m_n^*(q) = \frac{1}{\hbar^2}\left[\frac{\partial^2 E_n(q)}{\partial q^2}\right]^{-1} \tag{1.26}$$

with the *effective mass* of a particle subject to the external force F_{ext}. Note that the effective mass m^* is related to the curvature of the energy bands and reduces to the real mass m in the case of the parabolic free particle spectrum.

In the tight binding approximation, not only the energy spectrum 1.23 but also the dynamics is totally determined by the tunneling energy J, the Bloch velocity $v_0(q)$ and the effective mass $m_0^*(q)$ being related to the first and second derivatives of $E_0(q)$: by using equations 1.24 and 1.26 for the J-dependent energy spectrum 1.23, one easily gets

$$v_0(q) = \frac{2Jd}{\hbar} sin(qd) \qquad\qquad m_0^*(q) = m\left(\frac{E_R}{J}\right)\frac{1}{\pi^2 cos(qd)} \tag{1.27}$$

1.2.2 Disordered optical potentials

In subsection 1.1.3 we described how it is possible to tune the interactions of a BEC by using Feshbach resonances. We want to introduce now the second key ingredient that will allow us (see sections 2.1 and 4.4) to suitably describe the behavior of real systems, i.e. the *disorder*. The possibility to control the disorder in ultracold bosonic systems with laser light is quite remarkable, especially as compared with the real systems in nature, where conversely the disorder – which is intrinsically present[26] – can not be

---

[26] Note that the disorder plays a key role in nature as it, for instance, affects the transport properties of electrons in crystals [27].

controlled.

In this subsection the two main laser techniques to produce disordered optical potentials, that is the *laser speckles* and the *quasiperiodic optical lattices*, will be described.

Laser speckles

The laser speckles is a laser technique that takes advantage of a rough surface to produce a random intensity distribution of light. Observed in the early 60s in reflection, this light scattering process is now usually performed in transmission from a diffuser (see figure 1.11a). The speckle pattern (b) arises from the interference – constructive here, destructive there – between the partial waves, randomly shifted in phase, scattered from the various facets of the diffuser rough surface [29][30][31]. As the speckle-induced disorder is stable on time, i.e. on the typical experiments time scale, it can be characterized by only two parameters, namely its intensity standard deviation σ_I and its lengthscale Δx (see figure 1.12). As the dipole potential produced by a laser beam is proportional to its intensity (eq. 1.14), the intensity pattern $I(x)$ shown in figure results in an analogously disordered optical potential for the atoms.

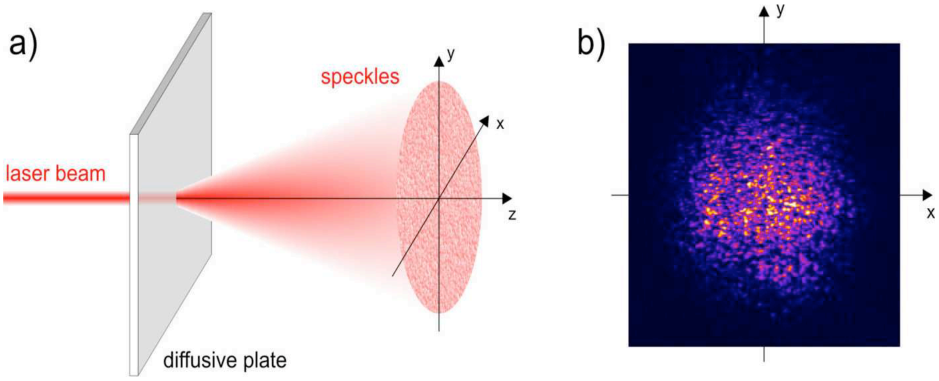

Figure 1.11: Laser speckles. A laser beam impinging on a diffusive plate (**a**) gives rise to a random intensity distribution of light (**b**). Figure taken from [28].

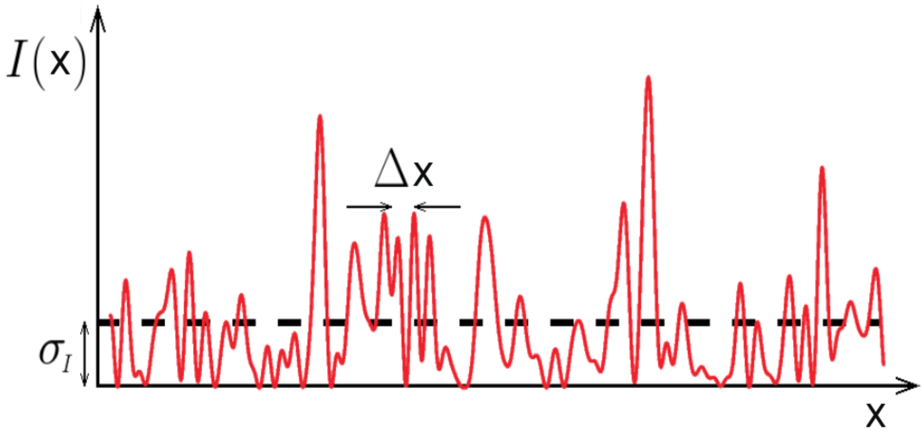

Figure 1.12: Intensity distribution along one direction of the speckle pattern. The intensity standard deviation σ_I, which characterizes the amplitude of the disorder, and its lengthscale Δx are reported. Figure adapted from [20].

As for the disorder lengthscale Δx, it is given by the diffraction limit related to the optical system employed to produce the laser speckles, i.e.

$$\Delta x \approx l \, \frac{\lambda}{D} \tag{1.28}$$

where λ is the laser wavelenght, l the distance between the diffusive plate and the target atoms, and D the diameter of the lens placed next to the diffuser. Note that the larger the laser beam size on the diffusive plate, the higher the number of effective scatters and the lower the speckle grain size.

We stress here that in our experimental setup the optical access to the atom cell is quite limited, the minimum distance we could set the diffuser from the atoms being $l \simeq 20\,\text{cm}$. With a laser with wavelength $\lambda \approx 1\,\mu\text{m}$ and beam diameter $D \simeq 5\,\text{cm}$, we would get a speckle grain size $\Delta x \approx 4\,\mu\text{m}$ that is not small enough compared with the size of our BEC ($10 \div 20\,\mu\text{m}$). For this reason, in order to produce the disorder, we employed a quasi-periodic optical lattice (see next subsection), whose "grain size" Δx is quite smaller as it is given by the lattice constant $d \approx \frac{1}{2}\mu m$.

Quasi-periodic 1D optical lattices

A quasi-periodic optical potential can be obtained by superimposing to an optical lattice with wavelength λ_1 a weaker one with an incommensurate wavelength λ_2, i.e. such that the ratio $\beta = \frac{\lambda_1}{\lambda_2}$ is an irrational number [32][33]. Let us define the periodic potentials with wavelength λ_1 and λ_2 respectively as the *main lattice* V_1 and the *secondary lattice* V_2 (see figure 1.13 on the top); the quasi-periodic optical lattice, also known as dichromatic lattice, is then given by $V(x) = V_1(x) + V_2(x)$, i.e. according to 1.16 and 1.17, by

$$V(x) = s_1 E_{r1} cos^2(k_1 x) + s_2 E_{r2} cos^2(k_2 x) \tag{1.29}$$

where $k_i = 2\pi/\lambda_i$ $(i = 1, 2)$ are the lattice wavenumbers and s_i are the lattice heights in units of the recoil energies E_{ri}. A plot of eq. 1.29 for $s_1 = 10$ and $s_2 = 1$ is shown in figure 1.13 (on the bottom) where the modulation induced by the secondary lattice at the beating frequency $c\,(k_2 - k_1)$ is highlighted with a dashed line.

Provided that $s_2 \ll s_1$ and β is an irrational number, the secondary lattice induces a perturbation in the main one, resulting in an inhomogeneous and non-periodic shift of the energy minima. In other words, the effect of the secondary lattice is to produce a sequence of wells $D = d/(\beta - 1)$ apart, whose lattice sites at the bottom have different potential heights. This shift of the energy minima is in a range of size $s_2 \beta^2$, thus proportional to the secondary lattice height s_2.

Moreover, it is possible to demonstrate [34] that the perturbation induced by the secondary lattice does not change significantly the position of the lattice sites, i.e. if $s_2 \ll s_1$ the position of the dichromatic lattice sites are $x_j \simeq d \cdot j$, d being the period of the main lattice.

Finally we note that the disorder introduced by using a dichromatic lattice is not a pure random disorder as it has a quasi-periodic structure, characterized by the frequencies ck_1, ck_2 and $c(k_2 - k_1)$. However the quasi-periodic potential breaks the translational invariance of a perfect lattice, and it can be thus used to study the physics of disordered systems.

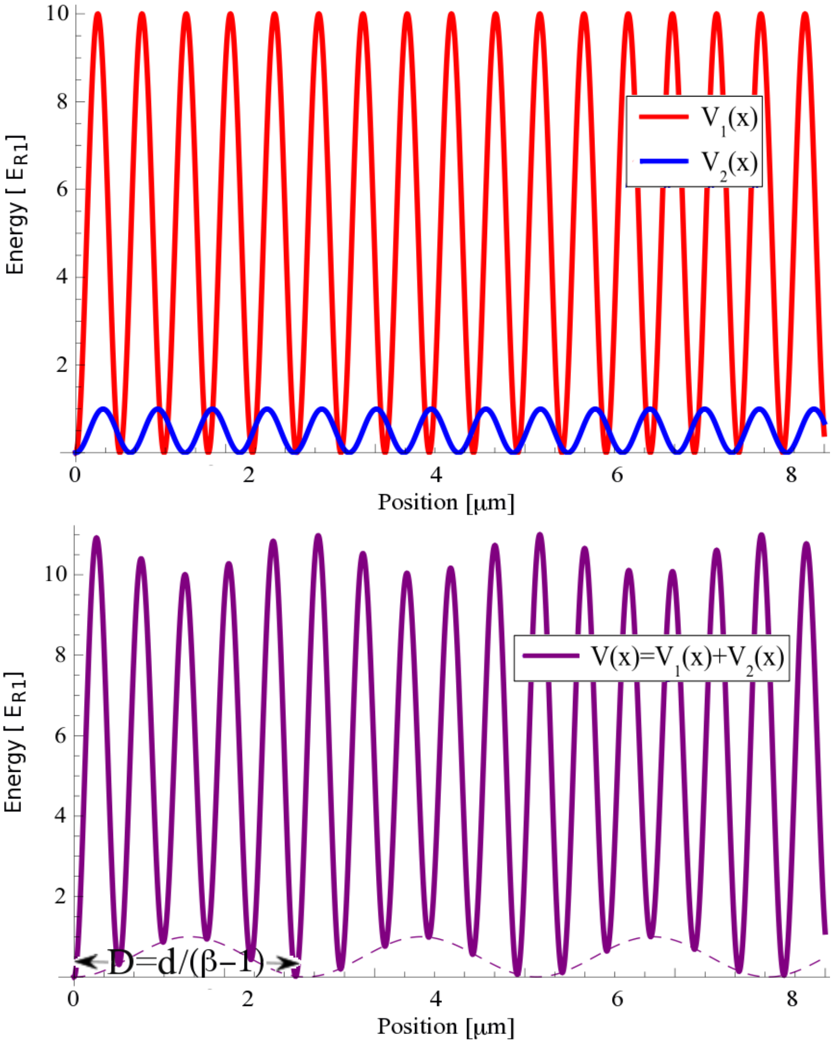

Figure 1.13: Quasi-periodic optical lattice (**bottom**) as a result of the superposition between two perfect lattices (**top**), one with $s_1 = 10$ and $\lambda_1 = 1064\,\mathrm{nm}$ (red) and the other with $s_2 = 1$ and $\lambda_2 = 862\,\mathrm{nm}$ (blue). The modulation (dashed line) induced by the secondary lattice produces a sequence of wells D apart, whose lattice sites with lower energy are at different potential heights.

CHAPTER 2

Disordered Bose-Hubbard model: Δ - U phase diagram

Contents

The many-body physics of interacting bosons in a lattice can be reproduced by the Bose-Hubbard (BH) model [35]. Such a model describes a zero-temperature system of bosons in an optical lattice assuming that each minimum of the periodic potential can be locally approximated by an harmonic potential well and that all the particles occupy the fundamental vibrational state of the lattice sites. This model is particularly powerful as it allows to take into account quantum correlations between particles in the regime of strong interactions. The effect of disorder, which is our main interest, can be introduced in this model as well.

After formally introducing the main features of the BH model, in this chapter we will describe the several regimes of physical interest. Starting from the condition of null disorder, we will describe firstly the interaction-induced transition from a conductive to an insulating phase both in the ideal case of an homogeneous system (section 2.2) and in the inhomogeneous experimental case with the presence of a trap potential (subsection 2.2.2). In section 2.3 we will then consider the effect of disorder starting from the case of null interaction: above a disorder threshold value a transition to another insulating phase will be shown to take place (Anderson localization). The delocalizing effect of weak interactions will be reported as well (subsection 2.3.1). Finally, in section 2.4 we will consider the disordered strong-interaction regime where a glassy insulating phase, called Bose-glass, is expected to appear.

2.1 The Bose Hubbard model

The quantum state of a gas of identical interacting bosons in an optical lattice V_{latt} and in the presence of an external potential V_{ext}, can be described [36] by the second quantization Hamiltonian

$$\hat{H} = \int d^3x\, \hat{\psi}^\dagger(\boldsymbol{x}) \left[-\frac{\hbar^2\nabla^2}{2m} + V_{latt}(\boldsymbol{x}) + V_{ext}(\boldsymbol{x}) + \frac{g}{2}\hat{\psi}^\dagger(\boldsymbol{x})\hat{\psi}(\boldsymbol{x}) \right] \hat{\psi}(\boldsymbol{x}) \tag{2.1}$$

where $\hat{\psi}(\boldsymbol{x})$ is a boson field operator and the coefficient g is linearly related to the scattering length a according to eq. 1.6. As shown in subsection 1.2.1 a Bloch wavefunction describing the quantum state of a particle in a lattice can be expressed as a superposition of Wannier functions localized at the lattice sites. This kind of description is particularly convenient when one wants to describe atom-atom on-site interactions. Moreover, under the assumption that the energies involved in the system are small enough not to induce inter-band excitations, we can restrict ourselves to consider only the lowest energy band $n = 0$; the boson field operators can then be written in terms of Wannier functions (omitting the band index) as follows

$$\hat{\psi}(\boldsymbol{x}) = \sum_i \hat{a}_i w(\boldsymbol{x} - \boldsymbol{x}_i) \tag{2.2}$$

$\hat{a}_i$ being the annihilation operator of one boson at the i-th lattice site and $w(\boldsymbol{x} - \boldsymbol{x}_i)$ being the Wannier function localized at the i-th site position x_i. By substituting this equation in 2.1 and considering only the tunneling between neighboring sites, one can obtain the disordered *Bose-Hubbard Hamiltonian*

$$\hat{H}_{DBH} = -J \sum_{\langle i,j \rangle} \hat{a}_i^\dagger \hat{a}_j + U \sum_i \frac{\hat{n}_i(\hat{n}_i - 1)}{2} + \sum_i \epsilon_i \, \hat{n}_i \tag{2.3}$$

where $\hat{a}_i$ and $\hat{a}_i^\dagger$ are the boson annihilation and creation operators satisfying the canonical commutation relation $[\hat{a}_i, \hat{a}_j^\dagger] = \delta_{ij}$, $\hat{n} = \hat{a}_i^\dagger \hat{a}_i$ is the number operator representing the number of particles at the i-th lattice site, and the symbol $\langle i, j \rangle$ indicates that the sum has to be considered only between nearest neighbor sites. As for the quantities J, U and ϵ_i, they are particularly important as they define the energy scales of the system:

- $J = -\int d^3x \, w^*(\boldsymbol{x} - \boldsymbol{x}_i) \left[-\frac{\hbar^2}{2m} \nabla^2 + V_{latt}(x) \right] w(\boldsymbol{x} - \boldsymbol{x}_j)$ is the *tunneling energy* which, as described in subsection 1.2.1, is related to the overlap between the Wannier functions localized at the i-th and j-th sites. As it represents the probability for an atom to hop from one site to another it can be thought of as an index of the delocalization of the particles throughout the lattice.

- $U = \frac{4\pi\hbar^2}{m} a \cdot \int d^3x \, |w(\boldsymbol{x})|^4$ is the *on-site interaction energy*, i.e. the energy related to the repulsive ($a > 0$) interaction between two atoms at the same lattice site. Note that in the BH Hamiltonian U is multiplied, for each lattice site, by the number of atom pairs $\frac{\hat{n}_i(\hat{n}_i - 1)}{2}$, in agreement with the fact that a site with $n_i = 0, 1$ does not contribute to the total interaction energy. Note also that interactions among atoms of different sites are here neglected.

- $\epsilon_i = \int d^3x\, V_{ext}(\boldsymbol{x})|w(\boldsymbol{x}-\boldsymbol{x}_i)|^2 \approx V_{ext}(\boldsymbol{x}_i)$ is the lattice *site energy offset*. This energy contribution to the system may arise from two factors: the first one is the external trap potential, which usually varies smoothly across the lattice such that the energy ϵ_i within each lattice site can be assumed constant; the second factor is the disorder, which can be produced by means of the laser techniques discussed in the previous chapter. In the case of a quasi-periodic optical lattice, $\epsilon_i \in [-\Delta, \Delta]$ where $2\Delta \simeq \beta^2 s_2 E_{r2}$ is the energy range of the disorder induced by the secondary lattice of depth s_2 [37].

We want to calculate now the integrals J and U and express them in terms of the optical lattice depth which is the parameter that can be controlled in the experiments. Let us consider an optical lattice of the form 1.16 in the 3D case, i.e. $V_{latt} = \sum_j E_r s_j\, sin^2(kx_j)$ with $j = x, y, z$. Under the assumption that around each minimum of the lattice potential this one can be approximated by an harmonic potential well ($sin^2 x \approx x^2$), the corresponding Wannier functions at each site i can be approximated as follows

$$w_i(\boldsymbol{x}) = \prod_{j=1}^{3} \left(\frac{k s_j^{\frac{1}{4}}}{\sqrt{\pi}} \right)^{\frac{1}{2}} e^{-\frac{\sqrt{s_j}}{2}(k\,x_j)^2} \tag{2.4}$$

i.e. Gaussian functions whose width decreases as the optical lattice depth s_j increases. With such an approximation for $w_i(x)$, it is possible to analytically calculate the above integrals for J_j (along each direction $j = x, y, z$) and U:

$$J_j = \frac{4}{\sqrt{\pi}} E_r\, s_j^{3/4}\, e^{-2\sqrt{s_j}}\ ; \qquad U = \sqrt{\frac{8}{\pi}}\, E_r k\, a \left(\prod_{j=1}^{3} s_j \right)^{1/4} \tag{2.5}$$

From equations 2.5 we observe that increasing the optical lattice depth s_j yields to an increase of the ratio U/J_j since it corresponds to:

- an exponential drop of the tunneling energy J_j as a consequence of the higher barrier that the particles have to hop in order to tunnel from one site to another.

- an increase in the interaction energy U as a consequence of the tighter confinement of the particle density distribution within each lattice site.

To sum up, the quantum phase of the system depends on the interplay between the just described three energy scales: the tunneling energy J_j (related to s_j), the interaction energy U (related to s_j and the scattering length a) and the disorder parameter Δ (related to s_2).

2.2 Homogeneous case: SF to MI phase transition

Let us start considering the ideal case of a translationally invariant 1D system in which there is no trap potential and no disorder; as the site energy level ϵ_i is constant all over the lattice, we can neglect the last term in the BH Hamiltonian 2.3 which thus reduces to

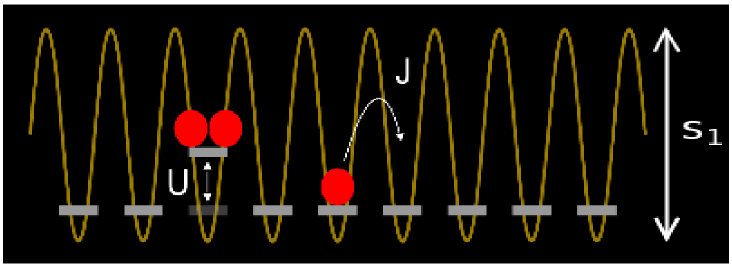

Figure 2.1: Homogeneous Bose-Hubbard model ($\epsilon_i = cost$). The energy of the system increases of the amount U, due to the repulsive interaction between two atoms sharing the same site, and decreases of the amount J, due to a particle hop from one site to another. Note that the higher the potential depth s_1, the larger the ratio U/J.

$$\hat{H}_{BH} = -J \sum_{\langle i,j \rangle} \hat{a}_i^\dagger, \hat{a}_j + U \sum_i \frac{\hat{n}_i(\hat{n}_i - 1)}{2} \tag{2.6}$$

The Bose-Hubbard model in the homogeneous case is illustrated in figure 2.1. Depending on the ratio U/J between the two remaining energy terms the system may show two quantum phases with different and well defined features, i.e. the superfluid (SF) phase and the Mott insulator (MI) phase.

When $U \ll J$, that is the first term in eq. 2.6 is the dominant one, each atom is delocalized throughout the lattice and the system is said to be a *superfluid*. Let us define the Bloch lowest energy state of a single delocalized particle as the superimposition $\sum_i \hat{a}_i^\dagger|0\rangle$ of the wavefunctions localized on each lattice site; the ground state of the system of N identical bosons can be then written as

$$|\Psi_{SF}\rangle = (\sum_i \hat{a}_i^\dagger)^N|0\rangle \tag{2.7}$$

that is the product of the N single-particle delocalized states. The system is thus described by one macroscopic wavefunction whose phase is consequently constant and well defined on each lattice site. As a consequence, the density distribution of the atoms after a free expansion[1] from the lattice, shows sharp peaks $\hbar G = 2\hbar k$ apart resulting from the interference of the phase coherent matter wave (see figure 2.2).

In a superfluid, thus, while for each site the phase is perfectly defined, the number of particles per site is not determined and exhibits Poissonian fluctuations. This is in agreement with the Heisenberg uncertainty principle for which the phase operator $\hat{\phi}_i$ and the number operator $\hat{n}_i$ are conjugate variables that obey to the commutation relation $[\hat{\phi}_i, \hat{n}_i] = i$.

When $U \gg J$, that is the second term in eq. 2.6 is the dominant one, the atoms cannot move from one site to another as particle number fluctuations are not energetically favorable any longer. This system is said to be a *Mott insulator*. The strong repulsive interaction forces the particles not to share the same sites, leading to an homogeneous and well defined distribution of the particles across the lattice. For a given chemical potential μ, the particle

---

[1] After a free expansion (*time-of-flight*) of a few tenths of ms, the spatial density distribution $|\Psi(\boldsymbol{x})|^2$ of a non-interacting BEC approaches the density distribution $|\Psi(\boldsymbol{p})|^2$ in the momentum space. This is regardless of the shape of the trapping potential. In the particular case of a BEC initially confined in an optical lattice with period d, the matter wave shows interference peaks approximately $1/d$ apart which recall the interference pattern of a diffraction grating. In that case, the lower the slits aperture, the larger the number of peaks; correspondently here, the smaller the width of the confined Wannier functions (i.e. the higher the lattice height), the larger the number of peaks.

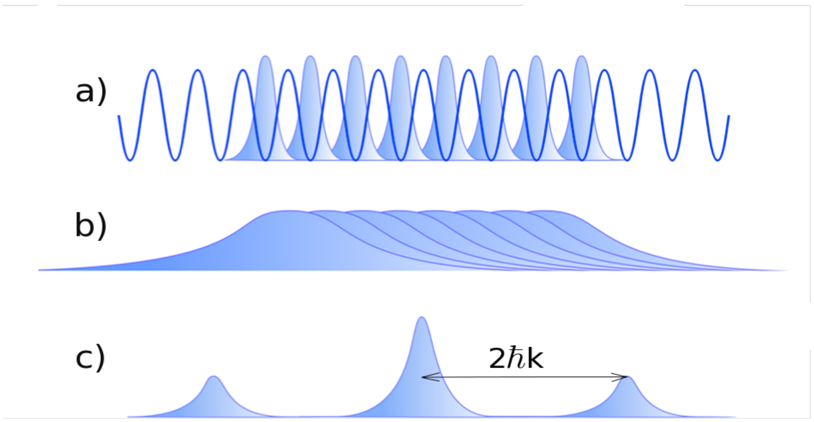

Figure 2.2: Interference pattern of the momentum density distribution after a free expansion from an optical lattice. (**a**) If the lattice height is low enough such that $J \gg U$, the Wannier functions localized at each site are phase locked to each other due to the tunneling. (**b**) When the optical lattice is switched off, the Wannier wavefunctions are free to expand. The narrower the initial (spatial) density distribution, the broader the final (momentum) density distribution. (**c**) The phase-locked expanded functions interfere each other giving rise to sharp peaks $2\hbar k$ apart, whose envelope is given by the single site density distribution.

number per site is thus well determined and the ground state of the system is given by the product of the single-site Fock states:

$$|\Psi_{MI}\rangle = \prod_i (\hat{a}_i^\dagger)^n |0\rangle \tag{2.8}$$

$n \in \mathbb{N}$ being the homogeneous site filling.

While the particle number per site is perfectly determined, there is no phase correlation (no overlap) between the Wannier functions localized at each site. As a result, no macroscopic phase coherence holds.

The SF to MI phase transition with ultracold atoms was first observed by Greiner et al. [38] by increasing the lattice height s_1 (and thus the ratio U/J). The time-of-flight fluorescence images of figure 2.3, show, for increasing depths of a $2D$ optical lattice, the progressive loss of phase coherence in the momentum density distribution (bottom row). Simultaneously, the high resolution in-situ images (top row), show the progressive reduction of atom

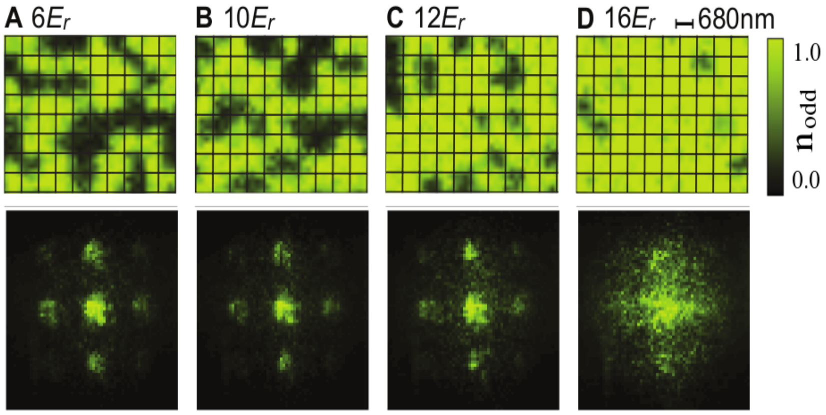

Figure 2.3: (**top row**) Single-site imaging of atom number fluctuations across the SF to MI phase transition. The In-situ fluorescence images are taken for increasing 2D-lattice heights from a region of 10 by 8 lattice sites within the n=1 Mott shell that forms in a deep lattice. Sites occupied with odd or even atom numbers appear in the images respectively as full or empty sites. This is the case of the SF regime (**A** and **B**), whereas in the MI regime, occupancies other than 1 are highly suppressed (**D**). (**bottom row**) Corresponding fluorescence images after free expansion of the cloud in the 2D optical lattice: the phase coherence is progressively lost moving from **A** to **D**. Figure adapted from [39].

number fluctuations across the $2D$ optical lattice.

The phase diagram of figure 2.4 shows the boundaries between the SF and MI phases at $T = 0$, as a function of the ratios μ/U and J/U [35]. In the MI phase ($J/U \ll 1$), for a given value of the chemical potential μ[2], the site filling n is well defined (integer number). In particular, as the chemical potential μ increases, the site filling n discontinuously increases. In the SF phase ($J/U \gg 1$), instead, for a given μ, the site filling $\bar{n}$ is defined only on average (poissonian number fluctuations). Note that for larger μ, and thus for larger site fillings n, the phase transition from MI to SF occurs at a smaller critical value $(J/U)_c$.

---

[2] The chemical potential μ, for a given temperature $T < T_c$, is a positive value depending only on the average particle density. In subsection 2.2.2, the role of μ will be played by an effective chemical potential μ_i taking into account the local inhomogeneities of the system.

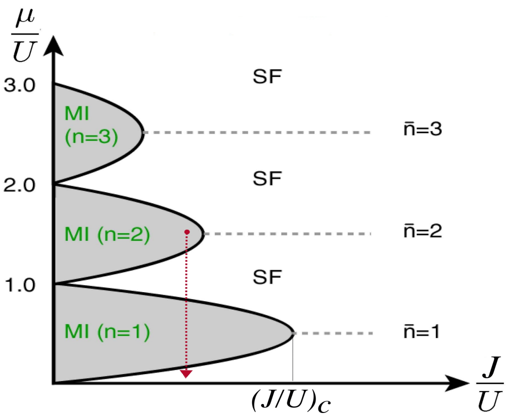

Figure 2.4: Phase diagram of the SF to MI transition in a homogeneous system as a function of the ratios μ/U and J/U. The MI lobes are characterized by a constant occupancy n and thus a vanishing compressibility K (corresponding to a discontinuous energy spectrum). In the SF phase the occupancy is defined only on average and, due to its gapless spectrum, the system is compressible. Note that the larger the average occupancy $\bar{n}$, the larger the interaction energy $(J/U)_c$ required to enter the corresponding MI domain. Figure adapted from [35].

2.2.1 Excitation energy spectrum and compressibility

So far we have compared the SF and MI phases referring only to the particle number fluctuations and the phase coherence properties. There are other two important features that characterize the two quantum phases, i.e. the excitation energy spectrum and the compressibility.

As it happens in solid state physics, the conductivity properties of the system are strictly related to its excitation energy spectrum: like the electrons in the metals, the atoms in the SF phase are capable to move from one site to another due to their *gapless energy spectrum*: when even a weak external force is applied to the system, the atoms start moving as they can be excited to states with energy very close to that of the original state by changing the momentum of some atoms by a small amount.

Conversely, in the MI phase where the atoms are not free to move, the energy spectrum is discontinuous with a gap of the order of U. In an homogeneous system[3], as sketched in figure 2.1, removing an atom from a site

---

[3] As we will see in section 2.4, an inhomogeneous system like a disordered one, shows

and adding it to a neighbor one with the same occupancy, has an energy cost equal to the on-site interaction energy U (see also the phase diagram 2.4 in the limit $J \to 0$). Figure 2.5 shows an experimental energy spectrum [40]

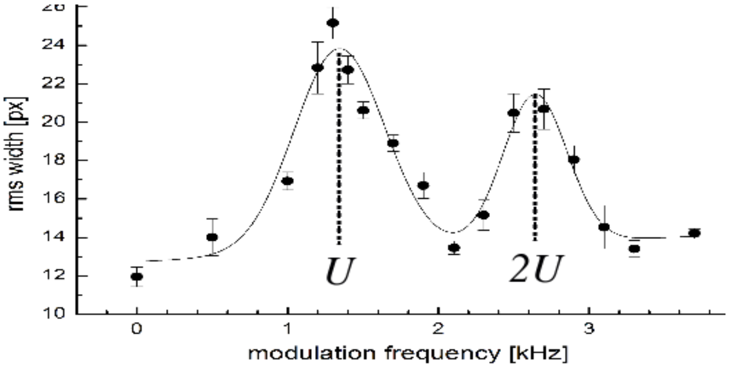

Figure 2.5: Excitation energy spectrum for a MI. The two peaks at the excitation energies U and $2\,U$ correspond to the hop of an atom to a site respectively with the same occupancy and with an occupancy difference of one atom (at the boundary between two MI domains). Figure adapted from [40].

with two peaks at the excitation energies U and $2\,U$. The former corresponds to the hop of an atom to a site with the same occupancy, the latter corresponds to the hop of an atom to a site with different site occupancy, which, as we shall see in the next subsection, is present at the boundary between two MI domains due to the inhomogeneity of the confined sample.

As for the compressibility, it is a measure of the density change as a response to an energy change; formally

$$K = \frac{\partial n}{\partial \mu} \tag{2.9}$$

The MI lobes of the phase diagram 2.4 are characterized by a constant site filling n and, consequently, a compressibility $K = 0$: a system in the MI phase is thus incompressible. This fact is a direct consequence of the discontinuous nature of the energy spectrum. The SF, whose energy spectrum is gapless,

---

a completely different energy spectrum.

is instead compressible: a small change in the energy of the system results in a change in the average particle number per site.

In table 2.1 the features of the SF and MI phases are summarized.

Superfluid $(J \gg U)$	*Mott-insulator* $(U \gg J)$
Long-range phase coherence	No phase coherence
Poissonian number fluctuations	No number fluctuations
Gapless excitation spectrum	Gap in the excitation spectrum
Compressible	Not compressible

Table 2.1: Superfluid and Mott-insulator phases.

2.2.2 Inhomogeneous case: shell structure

So far only the ideal homogeneous system for which $\epsilon_i = const$, has been considered. In this subsection we will take into account the experimental situation in which a local energy variation is always introduced by the presence of an external potential, due at least to the confining force exerted by the focused beams that form the optical lattices. The term $\sum_i \epsilon_i n_i$ in the BH Hamiltonian 2.3 must thus not be neglected any longer. Due to the energy

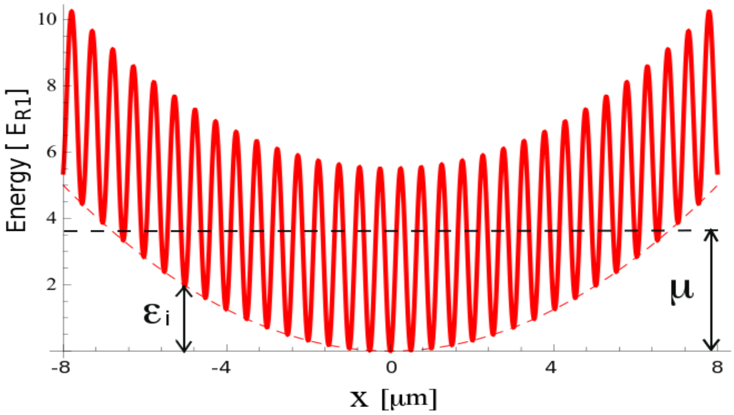

Figure 2.6: Optical lattice potential in the presence of an harmonic trap. The local effective chemical potential $\mu_i = \mu - \epsilon_i$ decreases moving from the lattice center to the edges.

offsets ϵ_i, the system can be thought to be characterized by a local effective chemical potential $\mu_i = \mu - \epsilon_i$ slowly varying through the lattice; With reference to figure 2.6, for an harmonic trapping potential, μ_i is maximum for the atoms at the center of the trap and progressively decreases moving towards the edges. According to the phase diagram of figure 2.4 (red dashed line), for a given value $J/U < (J/U)_c$, the atoms alternate different phases depending on their position across the lattice: moving from the center of the trap towards the edges, MI shells alternate to SF shells, the formers being characterized by a lower and lower occupation number (see figure 2.7 on the left). In the limit case of $J = 0$, only MI phases hold and the density profile

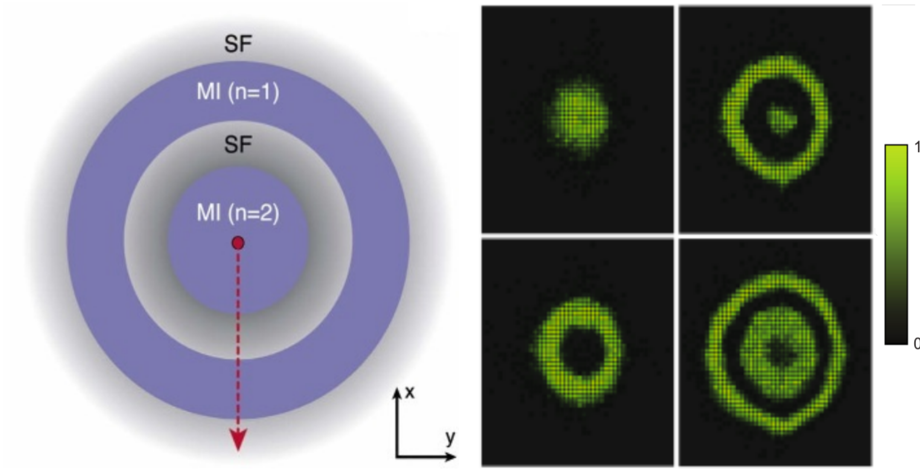

Figure 2.7: (**left**) Spatial distribution of the alternating MI and SF phases for a system confined in a harmonic trap with $J/U < (J/U)_c$. (**right**) Single-site images of the MI shell structure ($J \rightarrow 0$) for increasing atom number. Full (empty) shells contain an even (odd) atom number per site. Figures adapted from [41][39].

has a step-like structure, also known as wedding cake or shell structure, with integer occupation number of all sites, highest occupation numbers being at the center of the trap. Figure 2.7 (on the right) shows experimental images of the shell structure for increasing atom number [39]. Note that the larger the number of atoms, the larger the number of MI shells.

2.3 Non-interacting disordered system: Anderson localization

In this section we will first take into account a non interacting system and we will see how its transport properties are affected by the presence of disorder. In particular we are interested in the phenomenon, first studied by P.A. Anderson more than 50 years ago [42], of localization of particles and waves in disordered media. Anderson studied the transport of electrons in crystals by using a single-particle tight-binding model with random on-site energies: he showed that the transport, i.e. the diffusion of an initially localized wavepacket, is suppressed if the disorder amplitude Δ exceeds a critical value of the order of the tunneling energy J[4].

In the following we will see how the original idea of Anderson can be developed [44] to study the disorder induced localization of a quantum wavefunction in a quasi-periodic optical lattice (see subsection 1.2.2). It has been proven that this system shows a transition from extended to localized states analogous to the Anderson transition for a pure random disorder. The main difference is that with a quasi-periodic lattice the transition occurs already in 1D [33][45], whereas in the case of pure random disorder, 2D or 3D systems are required [46].

Let us consider a non interacting system ($U = 0$) in a 1D quasi-periodic optical lattice of the form 1.29. The BH hamiltonian 2.3 takes then the form (*Aubry-André Hamiltonian* [45])

$$\hat{H}_{AA} = -J \sum_{\langle i,j \rangle} \hat{a}_i^\dagger, \hat{a}_j + \sum_i \epsilon_i \, \hat{n}_i \qquad \text{with} \qquad \epsilon_i = \Delta \, cos(2\pi\beta \, i). \tag{2.10}$$

where the second term contains the quasiperiodic shift of the on-site energies due to the secondary lattice. $J \approx e^{-2\sqrt{s_1}}$ and $\Delta \simeq s_2 E_{r2} \beta^2/2$ are thus the two relevant energies which, as previously discussed, can be controlled

---

[4] Due to the high electron-electron and electron-phonon interactions, the transition between extended and localized states studied by Anderson for non-interacting electrons has not been directly observed in crystals [27]. Nevertheless, owing to the importance and the general validity [43] of his discovery, in 1977 Anderson was awarded the Nobel Prize in Physics.

independently by changing the heights s_1 and s_2 of the main and secondary lattice potentials, respectively.

As mentioned in subsection 1.2.2, when the ratio of the two lattice wavenumbers $\beta = \lambda_1/\lambda_2$ is an irrational number, the system displays features of a quasi-disorder system. If the disorder amplitude Δ is large enough, for the system is energetically convenient that the atoms are localized in correspondence of the energy minima: an atom jumping from a site to a neighbor one results in an energy cost for the system of the order of Δ (see the second term of equation 2.10). In particular, if the inverse of the golden ratio is used, $\beta = (\sqrt{5}-1)/2$, the model shows a "metal-insulator" phase transition from extended to localized states exactly at $\Delta/J = 2$ [45]. By diagonalizing the Hamiltonian the ground state wavefunction can be obtain. Figure 2.8 shows a typical density distribution, as a function of Δ/J, for $\beta = 1.1972...$ (corresponding to our experimental parameters). Note that due to the quasi-periodic nature of the potential, the localized states are $D \approx 5\,d$ apart, d being the period of the main lattice. Moreover, due to the limited degree of

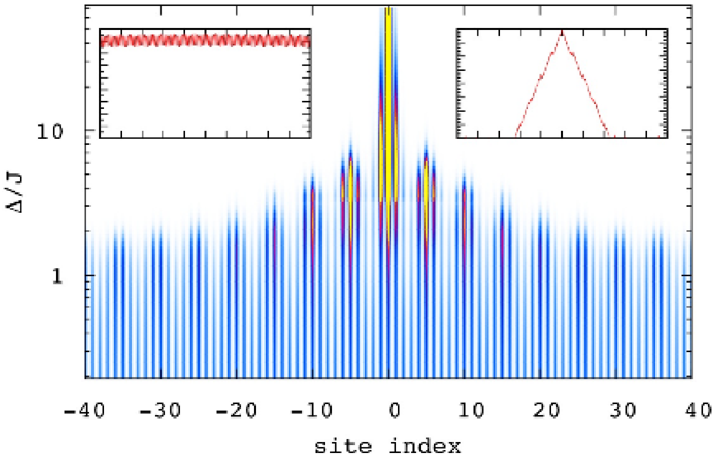

Figure 2.8: Density distribution as a function of Δ/J (vertical axis) for a quasi-periodic optical potential with $\beta = 1.1972...$. For small values of Δ/J the state is delocalized over many lattice sites (left inset). For $\Delta/J \approx 7$ the state becomes exponentially localized on lengths smaller than the lattice constant (right inset). Figure adapted from [20].

"irrationality" of the β used, the transition doesn't occur exactly at $\Delta/J = 2$ but is broadened and shifted towards larger values.

Absence of diffusion

The transport properties of the system have been experimentally investigated [47], by suddenly switching off the main harmonic confinement and letting the atoms expand along the one-dimensional dichromatic lattice. Figure 2.9a shows the in-situ absorption images of the BEC spatial density distribution for increasing evolution times. In the regular lattice ($\Delta = 0$) the eigenstates of the potential are extended Bloch states, and the system expands ballistically along the lattice (vertical) direction. For large disorder ($\Delta/J \geq 7$), there is no diffusion any longer: in this regime the BEC can be described as the superposition of several localized eigenstates whose individual extensions are less than the initial size of the condensate. In the crossover between these two regimes a ballistic expansion with reduced speed can be observed. Figure 2.9b shows the width of the atomic distribution af-

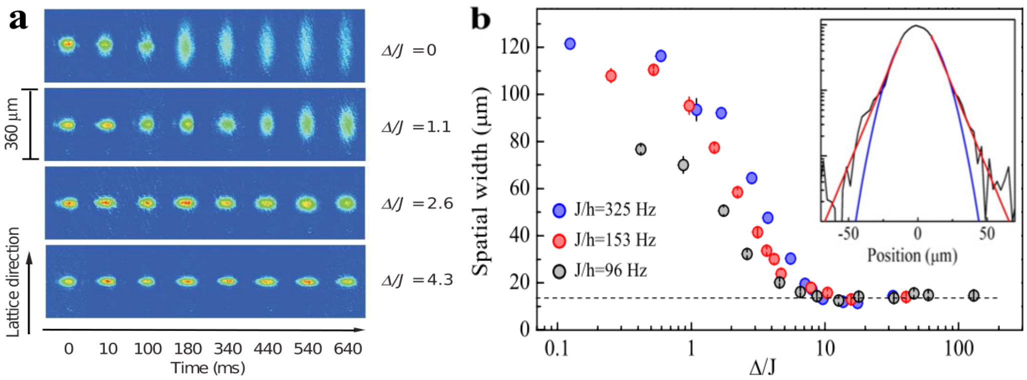

Figure 2.9: (**a**) In situ absorption images of the BEC diffusing along the quasi-periodic lattice for various values of Δ and with $J/h = 153\,\text{Hz}$. For $\Delta/J \geq 7$ the size of the BEC remains at its original value, reflecting the onset of localization. (**b**) Axial size of the condensate after 700 ms of diffusion, for three different values of the tunneling energy J in units h. The dashed line indicates the initial size of the condensate. The inset shows the exponential decay of the tails in the localized regime; a fit with an exponential function (red curve) and with a gaussian function (blue curve) are also reported. Figures adapted from [20].

ter 700 ms of diffusion as a function of the rescaled disorder strength Δ/J, for three different values of J. In all three cases, the system approaches the localized regime at the same disorder strength, providing clear evidence of the scaling behaviour of the Aubry-André model.

In this regime, the eigenstates of the hamiltonian in equation 2.10 are exponentially localized [48], and the tails of diffusing wave packets are expected to behave like stretched exponentials (see the inset of figure 2.9b).

Broadening of the momentum distribution

Information on the eigenstates of the system can also been extracted from the analysis of the momentum density distribution $P(k)$. The width of $P(k)$ is inversely proportional to the spatial extent of the condensate in the lattice. As mentioned in subsection 2.2, this can be measured by releasing the atoms from the lattice and imaging them after a ballistic expansion.

A comparison between the experimental and the theoretical momentum distributions $P(k)$ for increasing values of Δ/J is reported in figure 2.10. Without disorder, the typical grating interference pattern can be observed,

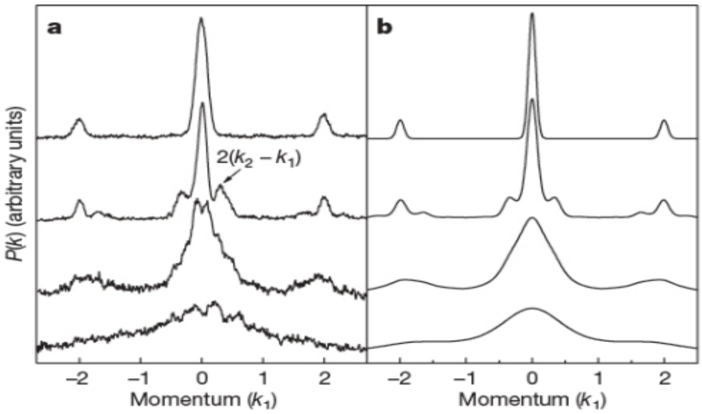

Figure 2.10: Experimental (**a**) and theoretical (**b**) momentum distributions $P(k)$ for increasing Δ/J (0, 1.1, 7.2 and 25, from top to bottom). The interference pattern of a regular lattice observed at $\Delta = 0$ is at first modified by the appearance of peaks at the beating between the two lattices, and then increasingly broadened. Momentum is measured along the horizontal axis in units of $k_1 = \pi/d$. Figure adapted from [20].

the three peaks at $k = 0, \pm 2k_1$ reflecting the periodicity of the primary lattice. The tiny width of the peak at $k = 0$ indicates that the wavefunction is spread over many lattice sites [49]. For weak disorder, the eigenstates of the hamiltonian in equation 2.10 are still extended, and additional momentum peaks appear at momentum space distances $\pm 2(k_1 - k_2)$ from the main peaks, corresponding to the beating of the two lattices. As Δ/J further increases, $P(k)$ broadens and its width eventually becomes comparable with that of the Brillouin zone, $\pm G/2 = \pm k_1 = \pm \pi/d$, indicating that the extension of the localized states has decreased down to the order of the lattice spacing d.

2.3.1 Delocalizing the system with a weak interaction

So far the effect of disorder has been considered only in the non-interacting regime. In this section we will thus describe how introducing a weak repulsive interaction can affect a disordered system.

While disorder tends to localize non-interacting particles in the absolute lowest energy state, giving rise to Anderson localization (see figure 2.11a), weak repulsive interactions can counteract this effect drastically changing the features of the system [50]. In particular, a weak[5] repulsion can "screen" the disorder [51] and bring the system back to a coherent, extended superfluid (d), passing through an intermediate glassy phase (b,c). In the evolution from an Anderson insulator to a superfluid we can think of two different stages:

- A very weak interaction pushes the bosons out of the lowest localized states, thus increasing the overall size of the system. The many-body states are however very close to the single-particle ones, and there is no coherence between distant or even neighbouring states. This regime is often addressed as an Anderson (or Lifshitz) glass in literature [52][53][54].

---

[5] As we shall see in the next section, a strong repulsion can instead induce a very complex competition between the disorder, the interaction energy and the kinetic energy, resulting in a non-trivial strongly correlated glassy phase (the so-called Bose glass).

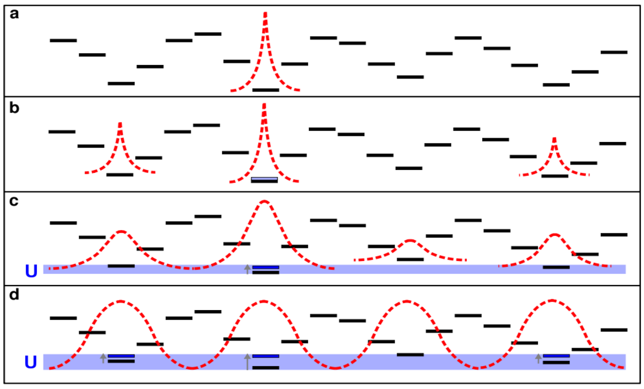

Figure 2.11: Schematic of the interaction-induced delocalization in a quasi-periodic optical lattice. (**a**) non-interacting regime ($U = 0$): for sufficiently large Δ the wavefunctions are exponentially localized and only the absolute lowest energy level is populated. (**b**) *Anderson glass*: with a very weak interaction several lowest energy levels are populated. (**c**) *Fragmented BEC*: due to the repulsive interactions several lowest energy levels become almost degenerate and the corresponding wavefunctions are modified giving rise to locally coherent fragments, though long-range phase coherence is not yet restored. (**d**) BEC: for large interaction strengths the energy minima are degenerate and a coherent extended wavefunction is formed. Figure taken from [50].

- For larger interaction energies (of the order of a tenth of Δ), the energy minima – where most of the atoms are localized and thus the effect of the interaction is larger – start becoming degenerate and consequently the many-body wavefunctions may occupy a few neighbouring sites. Here the system can locally be superfluid, but, globally, it is still an insulator. This regime is often addressed as fragmented BEC [54] (or weakly interacting Bose glass [35][37][55]).

Momentum distribution and correlation function

The transition from the insulating phase (Anderson glass) to the superfluid one of the disordered Bose gas has been investigated [50] by studying the momentum density distribution $|\Psi(k)|^2$ and, more conveniently, the associated correlation function $g(x) = \int \Psi^*(x+x')\Psi(x')dx'$, for U increasing from zero up to values of the order of J. Figure 2.12 shows an example of $|\Psi(k)|^2$ and the corresponding $g(x)$ for both a non-interacting system (on the left)

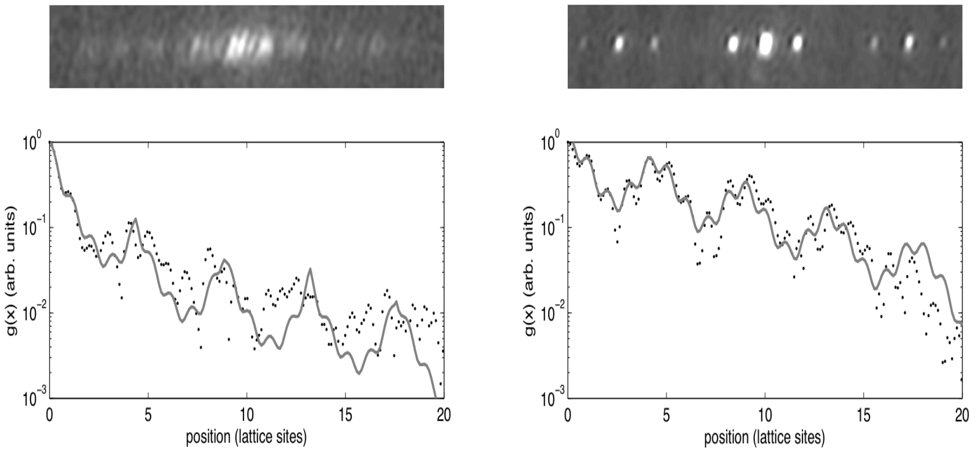

Figure 2.12: Momentum distribution for a non-interacting system (**left**) and for an interacting one (**right**). The derived correlation function $g(D)$ shows a fast decay (with a modulation of wavelength D) in the first case, and a much slower decay in the second case. Figure adapted from [56].

and for an interacting one (on the right). From the momentum density distribution, one can see that while the non-interacting system doesn't show any phase coherence, when the interaction is added the typical SF interference pattern is restored.

As for the correlation function $g(x)$, this shows a characteristic modulation at the lattice spatial frequency $1/d$, a second deeper modulation at the quasiperiodic frequency $1/D$, and an overall decay which is related to the long-range coherence properties of the system. The theoretical expectations in the presence of an external harmonic confinement are of an exponentially decaying $g(x)$ in an insulating phase, and a gaussian $g(x)$ in the superfluid phase, with an increasing decay length for decreasing localization. A qualitative indication of this behavior can be obtained by the evolution of the correlation function at exactly one quasiperiod, $g(D)$. Figure 2.13 shows $g(D)$ as a function of the ratios Δ/J and U/J both in the experimental (left) and the theoretical case (right) [50]. One can note for example how for vanishing interaction, $g(D)$ is saturated at a large value (blue) for $\Delta < 2J$, where the system is superfluid, while it gradually decreases when Δ increases

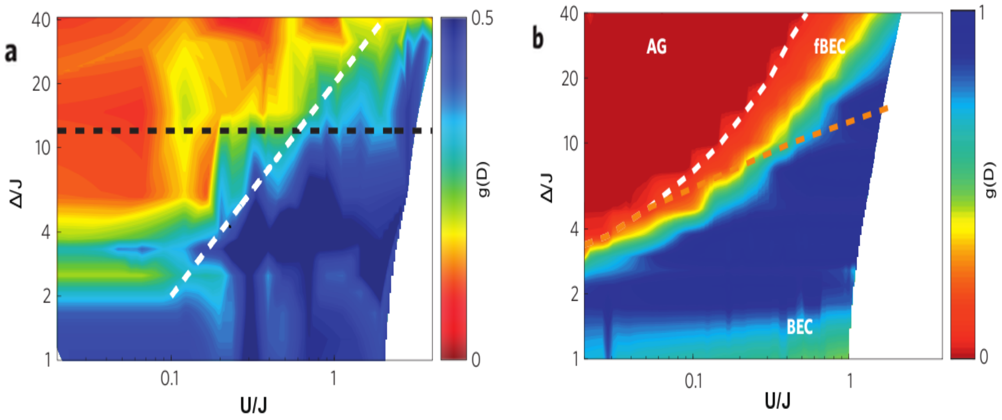

Figure 2.13: The experimental (left) and theoretical (right) evolution of the correlation function $g(D)$ as a function of the disorder strength and the interaction energy. The various regimes identified by the theoretical analysis are an Anderson glass (AG), a fragmented condensate (fBEC) and a superfluid (BEC). Figure adapted from [50].

to the Anderson localization regime (red-orange). This is in agreement with what has been previously discussed about the metal-insulator transition in the quasiperiodic lattice. Interestingly, for a given Δ and increasing U (black dashed-line), $g(D)$ increases again to reach almost the same value that it has at $\Delta = 0$. This is an evidence that the repulsive interaction tends to delocalize the system, bringing it back towards a superfluid.

It is interesting to note that the white line $U = 0.05\,\Delta$ in the experimental panel of figure 2.13 – which corresponds to the interaction energy being equal to the standard deviation of the quasiperiodic lattice lowest energy levels – nicely matches the center of the crossover from the glassy phase to the superfluid one. This quantitatively confirms the screening argument [51], according to which a sufficiently large interaction energy can screen the disorder making the lowest-lying energy levels become degenerate and thus making the corresponding bosonic wavefunctions phase lock each other to form a superfluid.

2.4 Strongly-interacting disordered system: BG phase

In this section the regime of strong interaction in the presence of disorder will be discussed. We will see that in such a regime a quantum phase not very different from the insulating Anderson glass analyzed in the previous section, is expected to appear [35]. In particular, we will focus our description on the transition that the system, with a given strong-interaction U, undergoes when the disorder amplitude Δ is gradually added. As discussed in section 2.2, when the system is homogeneous ($\epsilon_i = 0$), its properties are totally determined by the competition between the tunneling energy J and the interaction energy U (see figure 2.14a). In particular in the limit of strong interactions ($U \gg J$), the system is characterized by MI domains, each of them with an integer site occupation n determined by the local effective chemical potential. When a weak disorder $\Delta < U$ is added to the system (figure 2.14b), the MI lobes are expected [35] to shrink, their size being given

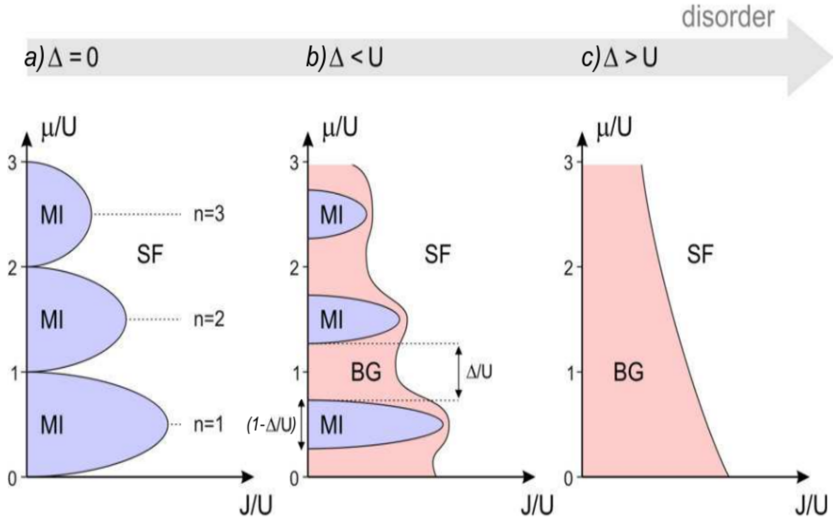

Figure 2.14: Phase diagram for an interacting disordered system as a function of the ratios μ/U and J/U. Depending on the interplay between the energy scales J, U and Δ, three quantum phases can be identified: a superfluid (SF), a Mott-insulator (MI) or a Bose-glas (BG) phase. Figure adapted from [57].

by $1-\Delta/U$, and progressively make room to another quantum phase, known as *Bose glass* phase. For larger disorders, when $\Delta \geq U$ (figure 2.14c), the MI lobes should completely disappear and, for a sufficiently small J, only the BG phase should hold.

A Bose Glass (BG) phase can be thought of as something in between a MI and a SF phase. Like a MI, the BG is insulating since it doesn't have long-range phase coherence. Like a SF, it has a gapless excitation spectrum (see next subsection) and consequently a finite compressibility. It is important to note that the coexistence of these two properties, i.e. insulating and gapless excitation spectrum, is not in contradiction: despite the zero energy gap, excitations only occur locally giving rise to regions of local superfluidity with short-range phase coherence but, globally, the BG remains insulating.

We also stress here that such features are in general typical of *glass*. As a matter of fact the quantum phase we referred to as AG in the previous section discussing about the weak-interaction regime is not different from the BG phase just described, since both are insulating and incompressible. Figure 2.15 shows a phase diagram as a function of the ratios Δ/J and U/J, obtained by numerically solving the Bose-Hubbard problem in the particular cases of occupancy $n = 1$ (left) and $n = 0.5$ (right) [37]; note that besides the MI and the SF phases, a unique glassy phase, indicated as BG, is present for large disorder amplitudes Δ, both in the weak and strong-interaction regime.

It is also interesting to note that since an integer occupancy n is required for the MI phase to form, in the case $n = 0.5$ only the SF and BG phases exist. In particular, above the threshold $\Delta/J = 2$ the system enters the BG phase as a consequence of the localizing effect of the disorder discussed in subsection 2.3. This is true except for the small U/J zone where, as discussed in subsection 2.3.1, the weak interaction delocalizes the system and consequently the SF-BG transition threshold is higher.

As for the $n = 1$ case, a MI phase instead forms for strong interactions (see subsection 2.2) and as the disorder amplitude Δ equals the interaction energy U (see dashed line), the excitation energy spectrum becomes gapless.

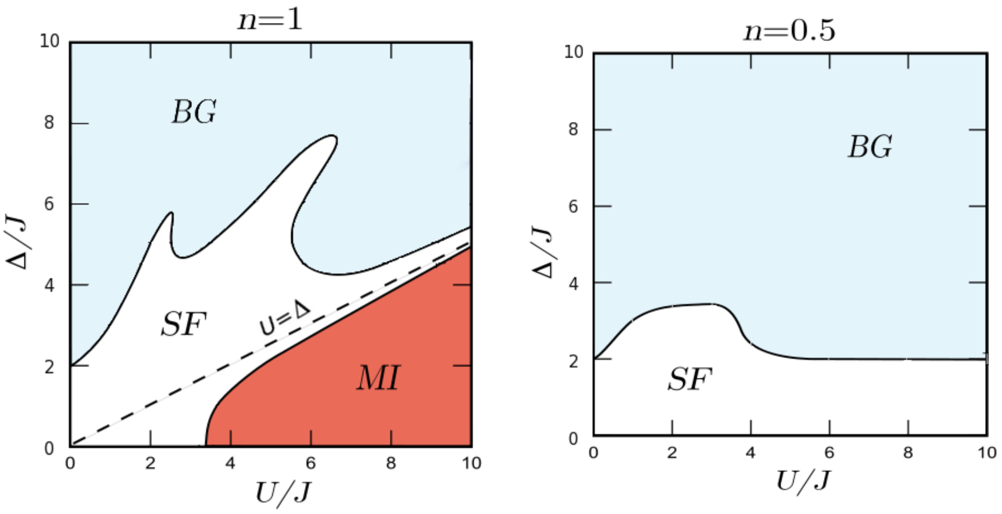

Figure 2.15: Phase diagrams as a function of the ratios Δ/J and U/J obtained by numerically solving the Bose-Hubbard problem for an occupancy $n = 1$ (**left**) and $n = 0.5$ (**right**); the dashed line in the case $n = 1$ indicates the disorder amplitude $\Delta = U$ above which for $U \gg J$ the MI energy gap vanishes. Figures adapted from [37].

We conclude this subsection stressing that in the experiments, due to the trap confinement, the number of atoms per site n in general varies along the optical lattice, meaning that we aspect a phase diagram that might be a combination of the two pictures of figure 2.15.

2.4.1 Gapless excitation energy spectrum

Let us now try to understand the gapless nature of the excitation spectrum in the BG phase. This will automatically explain why its compressibility, which has been defined in eq. 2.9, is non zero. With reference to figure 2.16a we first consider the limit case of a homogeneous MI ($J \to 0, \Delta = 0$): as explained in subsection 2.2.1, the lowest excitation energy is $\Delta E = U$ corresponding to the energy cost of an atom jumping from one site to a neighbor one with same occupancy (see also figure 2.5). Introducing disorder (figure 2.16b) yields random energy differences $\Delta_i \in [-\Delta, \Delta]$ between neighboring sites. As a result, the energy cost due to an atom jumping from one site to a

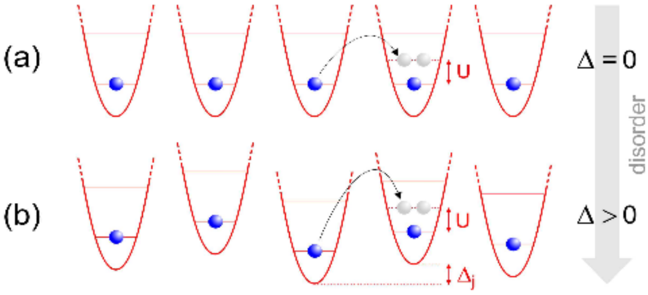

Figure 2.16: (**a**) In a homogeneous MI the energy cost for an atom jumping from one site to a neighbor one with same occupancy is $\Delta E = U$. (**b**) If some disorder is introduced the energy cost for such a process becomes $\Delta E_i = U \pm \Delta_i$, Δ_i being the disordered-induced energy difference between neighboring sites. Figure adapted from [57].

neighbor one is now position dependent as $\Delta E_i = U \pm \Delta_i$. This means that in the full BG regime, when $\Delta \geq U$, an infinite-sized system can be excited at arbitrarily small energies as the energy gap approaches zero[6].

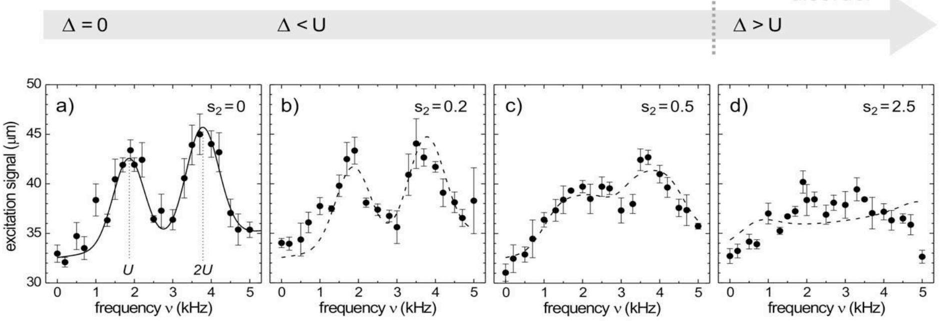

Figure 2.17: Excitation energy spectra of a strongly-interacting system for increasing height s_2 of the disordering lattice potential. (**a**) Excitation peaks in the MI phase ($\Delta = 0$) as in figure 2.5. (**b - d**) The characteristic excitation peaks progressively broaden and eventually, for $\Delta > U$, the energy spectrum becomes almost flat. Figure adapted from [57].

This vanishing energy gap in the excitation spectrum for the BG phase has

---

[6] Note that the excitation energy spectrum of a real finite-sized system, even though very small, always has a gap.

been experimentally investigated by [57]. Figure 2.17 shows the progressive broadening and eventually flattering of the MI excitation energy peaks as the disorder amplitude Δ increases.

Time of flight measurements performed at a given disorder amplitude $\Delta > U$, and for increasing height s_1 of the main lattice, have then shown a progressive loss of phase coherence of the system, indicating a transition from a SF to an insulating phase. The combination of these two results, i.e. gapless excitation spectrum and no phase coherence, has been a first experimental evidence of the existence of the BG phase [57].

2.5 Realization of quasi-1D systems

Most of the models and experiments we have presented in this Chapter are one-dimensional (1D). Let us now briefly discuss how such a regime can be reached in an experiment. At zero temperature, and for weak interactions, one can realize a quasi-1D system "simply" by superimposing a 1D disordered optical lattice along one of the axes of a 3D harmonic trap. Since the potential is separable along the longitudinal and radial directions, one can study the phenomena related to the disordered potential independently of the radial motion of the atoms. The atoms ideally populate the ground state energy level of the radial harmonic trap, while performing their complex dynamics along the disordered optical lattice. This was for example the strategy of the previous experiments on Anderson localization performed in our "BEC2" laboratory [47][50] and discussed in subsections 2.3 and 2.3.1.

This very simple technique fails when one wants to explore the regime of strong interactions. In this case, indeed, the interaction mixes the spatial degrees of freedom and the resulting interaction energy is redistributed along all three directions. As a matter of fact, the previous attempt to characterize the phase diagram of disordered bosons by tuning the scattering length of ^{39}K atoms [50] was limited to the regime of weak interactions. The reason is that the radial harmonic energy $\hbar\omega_r$ was comparable to the hopping energy J, and therefore an interaction energy $U > J$ would have brought the radial distribution in the Thomas-Fermi regime, where, as discussed in subsection 1.1.2, it acquires an interaction-dependent width. The radial broadening of the atomic distribution, in turn, lowers the density and the interaction energy itself. With this geometry it is actually impossible to achieve interaction energies larger than the radial harmonic one.

This problem can of course be overcome by using a much stronger radial confinement, such as the one that can be obtained by slicing the radial distribution into the very tight traps provided by an auxiliary 2D optical lattice. We will give a detailed description on the actual implementation of such a geometry in the Chapter describing the experiments (subsection 4.2.1). Here we want just to discuss how the picture above described changes when the radial confinement of the quasi-1D systems is provided by a very tight optical lattice, say with $s \approx 30$. Using equation 2.5 (one should introduce there also the zero-point energy $E_0 = \hbar\omega/2 = \sqrt{s_1} E_r$) one finds in this case that the tunnelling energy is very small, $J/h \sim 0.1\,\mathrm{Hz}$, and the on-site oscillation frequency is very large $\omega_r \approx 25\,\mathrm{kHz}$. On the one hand, this implies that on a realistic timescale for an experiment ($\lesssim 1\,s$) the atoms cannot tunnel from one site to the next, i.e. they can have an appreciable dynamics only along the axial direction. On the other hand, one finds that the radial energy becomes the dominant energy scale, $\hbar\omega_r \gg U, J$. Under these conditions the interaction energy can be made much larger than the tunneling one, and the regime of strong interactions, $U \gg J$, can be reached. This is the regime of interest for our experiments.

We would like to point out that an indefinite increase of the radial confinement would bring the quasi-1D gas into a regime of extreme interactions, the so-called Tonks-Girardeau regime [58][59][60]. It is indeed possible to see [61] that if the length of the radial harmonic oscillator becomes comparable to the scattering length, then the nature of the two-body collisions change, since the collision energy can no longer be distributed in the radial directions, but only in the axial one. This has in turn a drastic impact on the properties of a zero-temperature system, which can show a ”fermionization” phenomenon where basically the individual bosons tend to avoid each other and get segregated in limited spatial regions along the 1D system. The experiments we have performed are however out of this regime, and we will not give a detailed description of its properties. We want just to note that one can in principle define a parameter that measures the closeness to such regime of very strong interactions:

$$\gamma \approx \frac{2aa_{\parallel}}{a_{\perp}^{2}N}\,, \tag{2.11}$$

where a is the scattering length, $a_{\parallel}$ and $a_{\perp}$ are the longitudinal and radial harmonic lengths, respectively, and N is the atom number. One enters the extreme-interactions regime when $\gamma \gg 1$. In our case instead is $\gamma \simeq 0.5$.

CHAPTER 3

Realization of a laser portable spectrum analyzer

Contents

In this chapter we will describe the features of a homebuilt laser portable spectrum analyzer (LPSA) and we will show how this is used to monitor the stability of the several diode lasers employed to produce the BEC. Such spectrum analyzer is the result of a part of this thesis work, performed at the Niels Bohr Institute (NBI) in Copenhagen in the group of Prof. Eugene Polzik and Prof. Jörg Müller. Presently in use at the NBI laboratories, the portable spectrum analyzer in principle is suitable for being used at our laboratory at LENS as well.

3.1 Introducing the LPSA

The laser portable spectrum analyzer allows to investigate the features of a laser beam as it is coupled to the analyzer by means of an optical fiber.

Besides a Rubidium cell[1] – which allows to perform *saturation spectroscopy* and analyze the absolute frequency of the signal – the heart of the setup is a confocal *Fabry-Pérot interferometer*. With a $Finesse \approx 1000$, the Fabry-Pérot allows a resolution ($\gamma \approx 1\,\mathrm{MHz}$) larger than that one of the natural linewidth (of the order of a few tenths of MHz).

The idea at the base of this project is to study the spectrum purity of the lasers (in particular the slave lasers) used for the production of a BEC. The aim is to check whether the slave lasers do "follow" in frequency or not the master laser which feeds them, and find out the possible presence of uncontrolled sidebands. Another function of the LPSA is to assess whether the diode laser, used to probe at various frequencies the BEC during the experiments, is single or multi-mode.

For the (upstream) coupling into the optical fiber to be easier, a setup involving a *laser pointer* – whose beam is downstream coupled – has also been implemented: the laser pointer beam produces in fact a bright trace for the alignment of the counterpropagating laser beam that must be analyzed.

Besides the mechanical design of the optical cavity and the laser pointer mounts, the project required the design and the construction of an electronic circuit. The main parts of this electronic circuit are: a triangle *ramp generator* (with adjustable amplitude and offset) for scanning the piezoelectric transducer mounted on one of the Fabry-Pérot mirrors; a circuit for the DC-DC conversion from 24V (voltage provided by the wall power supply needed to scan at least one Free Spectral Range) to 3V for the laser pointer supply.

Furthermore the project required the construction of three *photodetectors* (also supplied at 24V by the above mentioned circuit): two of them for detecting the Rb cell and the Fabry-Pérot signals, the third one – with adjustable sensitivity – for monitoring the light coupled into the optical fiber.

To sum up, what is needed for the LPSA to work is simply an oscilloscope for the display of the three signals coming from the photodetectors and the

---

[1] Note that in principle the cell of Rubidium might be replaced with one of another sample, like, for instance, Potassium which in addition to Rubidium is used in our laboratory at LENS.

two signals (trigger and ramp) coming from the triangle ramp generator.

3.1.1 Basics of Fabry-Pérot interferometer

A scanning Fabry-Pérot interferometer makes use of the optical transmission characteristics of an optical cavity (Fabry-Perot) as a very selective filter to scan across the optical spectrum of a laser.

For an easier understanding of the Fabry-Pérot basic features, we will now assume both the laser beam wavefront and the cavity mirror shape to be flat. The description of the actual gaussian shape of the beam in a curved mirror interferometer will be introduced and discussed later (subsection 3.1.1).

Let us consider a beam with frequency ν and intensity I_{IN} impinging (perpendicularly) on an interferometer consisting of two identical mirrors with *reflectivity* R and separated by a distance L. We are interested in the *transmission function* I_T/I_{IN} – that is the ratio of the transmitted to the incident beam intensity – as a function of ν, R and L. The dependance on the frequency ν is connected with the type of *interference* occurring between the multiple reflections of the beam bouncing back and forth inside the cavity. Constructive interference – which corresponds to high transmission peaks – occurs when a beam with wave-number $k = 2\pi/\lambda$, after a *round trip* $2L$[2], is in *phase* with itself; in other words, the resonant condition is achieved when the phase shift $\delta = k \cdot 2L$ is an integer multiple of 2π. As a consequence the steady waves resonating in the cavity are those with wavelengths and frequencies:

$$\lambda = \frac{2L}{n} \qquad \nu = \frac{c}{2L} \cdot n \tag{3.1}$$

with $n = 0, 1, 2...$ and c speed of light[3]. This means that in frequency space the resonant peaks are shifted each other by a constant quantity (*Free Spectral*

---

[2] If we consider a cavity in a medium with index of refraction n_r, then the path length $2L$ must be replaced by the optical path length $2Ln_r$.

[3] Since usually the wavelength λ of a laser beam is of the order of $1\,\mu m$, for a cavity length $L \approx 10\,\text{cm}$, the number of longitudinal modes resonating into the cavity is $n \approx 10^5$.

Range[4])

$$FSR = \frac{c}{2L} \tag{3.2}$$

By going through the math, in the absence of losses[5], one can find [62] that the transmission function, also known as *Airy function*, is given by:

$$\frac{I_T}{I_{IN}} = \frac{1}{1 + (2F/\pi)^2 \sin^2(\delta/2)} \tag{3.3}$$

where F is a dimensionless quantity related to the quality of the cavity – and for this reason named *Finesse* – that depends on the mirrors reflectivity R[6] as:

$$F = \frac{\pi\sqrt{R}}{1-R} \simeq \frac{\pi}{1-R} \tag{3.4}$$

where the approximation is valid for high reflectivity mirrors ($R \simeq 1$). For instance for a reflectivity $R = 99\%$ the Finesse is $F \approx 300$, while for the interferometer used in the present work for a nominal reflectivity $R = (99.75 \pm 0.1)\%$ – theoretically[7] – we get:

$$F_{th} = 1255^{+838}_{-359} \tag{3.5}$$

According to 3.3, at resonance ($\delta = 2\pi\, n$) – for lossless mirrors – all the light is transmitted ($I_T = I_{IN}$)[8]. The *phase shift* can be expressed in terms of length or frequency as follows:

$$\delta = k \cdot 2L = 2\pi \frac{\nu}{FSR} \tag{3.6}$$

A plot of the Airy function in terms of frequency is shown in figure 3.1. Note

---

[4] The FSR reciprocal $\tau = 2L/c$ is the round trip time, that is the time needed for the light to go back and forth in the cavity.

[5] The *losses* Σ in the Fabry-Pérot are due to both *absorption* from whatever inside the cavity – mirrors, medium – and *diffraction* (when the beam size is not negligible with respect to the mirrors aperture). Note that the higher the Finesse, the higher the losses. If one takes into account the losses, then equation 3.3 has to be multiplied by the factor $T^2/(1-R)^2 < 1$ where T is the mirror transmissivity and, for the energy conservation law, $1 - R = T + \Sigma$.

[6] If the mirrors are different R is the geometric mean reflectivity of the two mirrors: $R = \sqrt{R_1 R_2}$.

[7] In chapter 3.4 we will se how some factors can lead to a lower experimental value for the Finesse.

[8] Out of resonance ($\delta = 2\pi[\,n + 1/2\,]$), the transmission function doesn't vanish but approaches to the background value $1/[1 + (2F/\pi)^2$ which decreases as the Finesse increases.

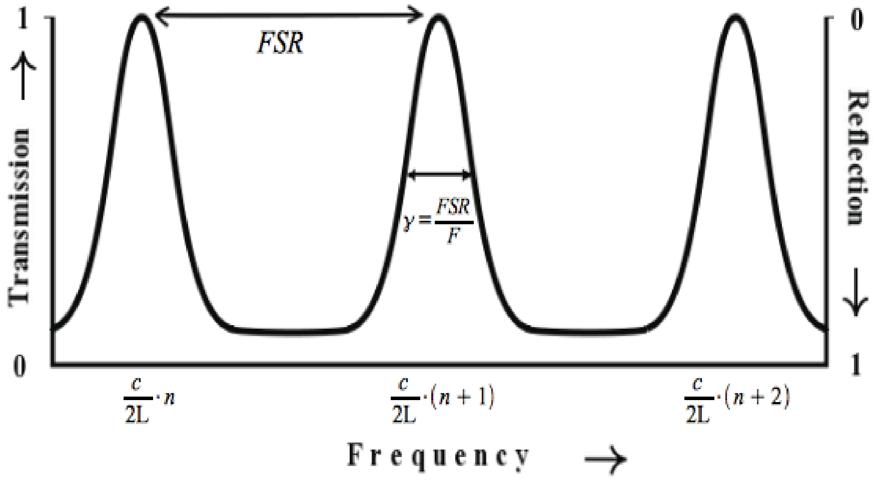

Figure 3.1: Transmission and reflection signal as a function of frequency for a Fabry-Pérot interferometer in absence of losses. Note that the peaks – which can be thought of as Lorentzian functions – are one FSR apart and that the higher the Finesse, the narrower the linewidth γ.

that in the absence of losses, the signal reflected by the interferometer $\frac{I_R}{I_{IN}}$ is the complement of the transmission signal, such as (*energy conservation law*)

$$\frac{I_R}{I_{IN}} + \frac{I_T}{I_{IN}} = 1 \tag{3.7}$$

As for the signal inside the cavity $\frac{I_C}{I_{IN}}$, this can be obtained by simply dividing the Airy function 3.3 by the mirror transmissivity T (which takes into account the output intensity reduction due to the transit of the beam through the last mirror):

$$\frac{I_C}{I_{IN}} = \frac{1}{T} \cdot \frac{I_T}{I_{IN}} \tag{3.8}$$

Since usually T is a very small value (typically ranging from around 1% down to 1 ppm), the signal in the cavity, at resonance, can be much more intense than the incident one (which, as we saw, at resonance and in the absence of losses is equal to the transmitted one).

One can show[9] that by expanding the Airy function 3.3 around a peak

---

[9] For small displacement ($\delta\nu \ll FSR$) around the peak center the sin function in the

center, for a small frequency *detuning* $\Delta\nu$, the peak has the shape of a Lorentzian function:

$$L = \frac{1}{1 + (\frac{2\,\Delta\nu}{\gamma})^2} \tag{3.9}$$

whose *linewidth* γ ($FWHM$) is connected to the FSR and the *Finesse* by the fundamental relationship

$$\gamma = \frac{FSR}{F} \tag{3.10}$$

For instance, for the interferometer used in this work ($F_{th} \approx 1300$) the theoretic linewidth is $\gamma_{th} \approx 600\,\mathrm{MHz}$. Obviously, the lower the linewidth, the higher the *resolution* of the interferometer.

It's interesting to note that the peak linewidth is strictly related to the cavity *decay* (or *storage*) *time*

$$\tau_s \simeq \frac{1}{2\pi\,\gamma} \tag{3.11}$$

that is the time after which the energy stored in the cavity without input decreases by a factor $1/e$[10].

In conclusion one can think of the transmission signal (equation 3.3, figure 3.1) as a series of Lorentzian functions, each one separated from the others – in frequency space – by one FSR and with a linewidth that is inversely proportional to the Finesse which in turns increases, according to equation 3.4, with the mirror reflectivity R.

TEM_{pl} modes in a symmetric spherical mirror cavity

So far we have considered only the flat mirror cavity that has the advantage of supporting only the longitudinal modes since the higher order transverse modes TEM_{pl}[11], in this configuration, turn out not to be stable.

Airy equation can be approximated with its argument and by using 3.6 in equation 3.3 one gets the result 3.9.

[10] Note also that the ratio of the storage time to the round trip time τ is connected to the number of round trips N_{rt} and to the Finesse F by the simple relationship $N_{rt} \approx (\tau_s/\tau) \simeq F/(2\pi)$.

[11] In cylindrical coordinates, the transverse mode patterns of a laser beam are described by the Gaussian-Laguerre TEM_{pl} modes where p and l are integers respectively labeling the number of rings and the number of bars across the pattern.

The flat mirror cavity, however, has the drawback that it is the most difficult to be aligned and the actual resolution – which for this configuration is strongly alignment dependent – is usually much less[12]. For this reason spherical mirrors usually result to be more suitable.

When describing the resonant modes in a spherical mirror cavity, one must take into account that the laser beam wavefront is not flat but its phase in general is given by:

$$\phi(z) = kz - (2p + l + 1)\arctan\frac{z}{z_R} \tag{3.12}$$

where z is the beam propagation direction and $z_R = (\pi\, w_0^2)/\lambda$ is the Rayleigh length. With respect to the first (plane wave) term there is a phase shift which depends on the transverse modes order (i.e. on the mode indices p, l)[13]. For constructive interference to occur, the phase shift from one mirror to the other – which also will be mode number dependent – must be a multiple of π. By using this condition in equation 3.12, after some manipulations it turns out that the resonance frequencies inside a spherical cavity with equal mirrors are:

$$\nu_{n\,p\,l} = \frac{c}{2L}\left[n + \frac{2p+l+1}{\pi} arccos\left(1 - \frac{L}{R_C}\right)\right] \tag{3.13}$$

According to the second term of the equation, which depends on the radius of curvature R_C[14], the transverse TEM_{pl} modes with the order index $k = 2p+l$[15] are frequency shifted – with respect to the longitudinal TEM_{00} mode

---

[12] Furthermore, the very precise alignment and well collimated beam needed to achieve high resolution, causes the beam to be reflected directly back into the laser, possibly destabilizing it.

[13] By replacing $(2p + l)$ with $(m + n)$ – where the indices m and n are integers labeling the number of bars in the x and y directions – the beam phase expressed for a rectangular geometry is obtained.

[14] Note that for a flat mirror cavity ($R_C = \infty$) the second term of equation 3.13 vanishes and we get the previous result with the only longitudinal modes spacing $c/(2L)$. Note also that in the general case of asymmetric cavity mirrors with radii of curvature R_{C1} and R_{C2}, the argument of *arccos* in 3.13 must be replaced by $\sqrt{(1 - L/R_{C1})(1 - L/R_{C2})}$.

[15] Note that the resonant frequencies depend on $k = 2p + l$, not on p and l separetely; therefore, different transverse modes with same k are *degenerate*.

– by the quantity:

$$\Delta\nu_k = \frac{c}{2L} \cdot \frac{k}{\pi} \arccos\left(1 - \frac{L}{R_C}\right) \tag{3.14}$$

As shown in figure 3.2, for a near planar or long-radius cavity ($R_C \gg L$),

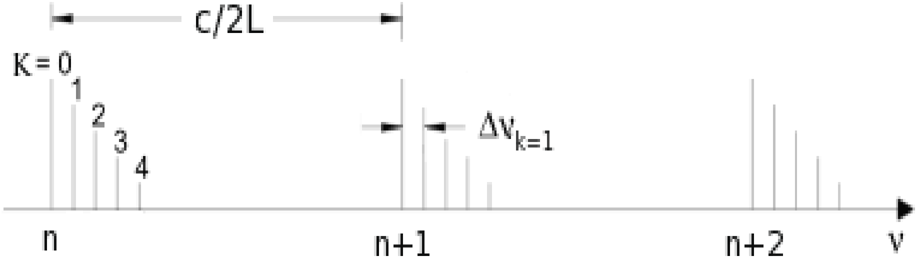

Figure 3.2: Resonant-mode spectrum for a near planar ($R_C \gg L$) optical cavity. The spectrum is composed of the TEM_{00} (longitudinal) modes – spacing $c/(2L)$ – surrounded by the less and less intense, degenerate, transverse modes identified by the order index $k = 2p+l$ and equally spaced by the quantity $\Delta\nu_{k=1}$. Figure adapted from [63].

the frequency shift 3.14 is small compared to the FSR (frequency distance between the longitudinal modes). Therefore, in this case[16], the spectrum is composed of the relatively high longitudinal modes surrounded by a set of equally spaced, degenerate, (transverse) higher order modes.

Confocal configuration

Even though the laser beam is a gaussian TEM_{00} beam, without *mode matching* – that is preferential coupling into a single mode – many transverse modes of the interferometer may be excited, making the display quite useless[17].

---

[16] In subsection 3.4.1 will be shown the experimental case of $L \gtrsim R_C$ where the transverse mode spectrum looks a bit different.

[17] The number of the higher modes resonating into the cavity can be easily of the order of 100 for a big size of the beam impinging on the input mirror and in absence of mode matching and of a good alignment (beam offset from the axis).

A way to avoid the problem is to use a cavity configuration (i.e. a particular cavity length L with respect to R_C) in which some of the (transverse) higher order modes have the same frequency as the (longitudinal) TEM_{00}[18] modes. The *degeneracy condition* is that the *arccos* term in equation 3.13 equals π/N with $N = 1, 2, 3...$

The most important and common configuration – which has also been used

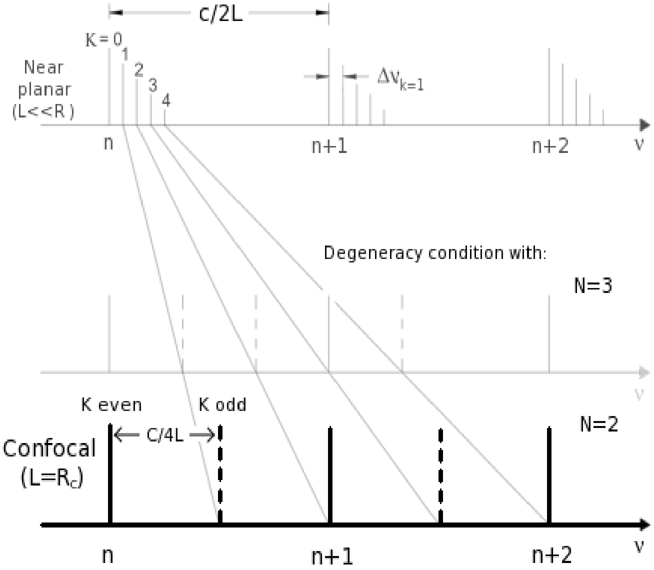

Figure 3.3: Resonant-mode spectrum for a confocal ($L = R_C$) optical cavity (bottom). The even higher order modes are degenerate with the longitudinal modes. The odd higher order modes fall halfway between the longitudinal modes cutting the FSR of the cavity in half to $c/(4L)$. This mode degenerate spectrum ($N = 2$) is shown as a result of the shifting of the transverse modes as the length L of the cavity – initially in a near planar configuration (top) – increases. The degeneracy condition with $N = 3$ (center) is shown as well. Figure adapted from [63].

in the present work (see chapter 3.4) – is the *confocal configuration* ($L = R_C$) where both the mirrors have the focus in the center of the cavity[19]. In figure 3.3 it can be seen how the frequencies of the transverse modes move with

---

[18] Note that, since transverse and longitudinal modes have the same characteristics, the resolution of the ideal interferometer is not affected by the fact that each peak representing a longitudinal mode of the input laser may actually be built up of contributions from multiple transverse modes excited in the cavity.

respect to those of the longitudinal modes as the optical cavity length L is changed leading to degeneracy conditions such as the confocal configuration $(N = 2)$. In such a configuration the frequency shift for the k^{th} higher order mode is:

$$\Delta\nu_k = \frac{c}{4L} \cdot k \tag{3.15}$$

meaning that the transverse modes with:

- *even* k are degenerate with the longitudinal modes.
- *odd* k fall halfway between the longitudinal modes cutting the FSR of the cavity in half to $c/(4L)$.

Such a FSR corresponds to the fact that a paraxial beam (i.e. one parallel to the optical axis) entering the confocal cavity off-center, returns to its original position after travelling the cavity four times in a zig-zag pattern (figure 3.4). However, if the beam is very well aligned to the optical axis, either the modes with even k or those with odd k will be excited, leading again to a $FSR = c/2L$.

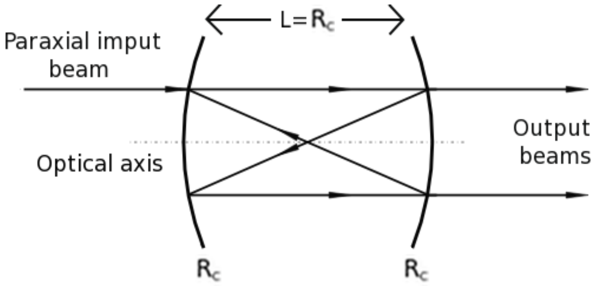

Figure 3.4: Zig-zag pattern of a laser beam propagating in a confocal optical cavity: the paraxial (off-centered) beam overlaps with itself after a path of $4L$. Note that the beam produces two spots on the mirrors. Figure adapted from [63].

3.1.2 Basics of Saturation spectroscopy

In high precision experiments the saturation spectroscopy is a technique that allows to overcome the problem of the Doppler broadening of the atomic lines, thus enabling the observation of the otherwise coverd atomic *hyperfine structure*[20].

The *Doppler broadening* of the atomic lines is due to the thermal agitation of the atoms in a gas. If we indicate with V_x the atoms speed along the laser beam direction, the laser frequency ν_L in the atoms reference frame is given by (*Doppler effect*):

$$\nu'_L = \nu_L \left(1 - \frac{V_x}{c}\right) \tag{3.16}$$

So only the atoms with $V_x = 0$ absorb the laser radiation when its frequency ν_L coincides with that one of the actual transition (let's call it ν_0). Vice-versa, the atoms with $V_x \neq 0$ can be at resonance with laser radiation at different frequencies from ν_0.

The resulting absorption pattern, in agreement with the atomic Maxwell velocity distribution, is a gaussian-like pattern characterized by a FWHM

$$\gamma_D = \nu_0 \sqrt{\frac{8\,ln2\;k_B T}{Mc^2}} \tag{3.17}$$

whit k_B Boltzman constant, M atomic mass and T absolute temperature. For a Rb gas, for instance, at room temperature we get a Doppler broadening $\gamma_D \approx 500\,\mathrm{MHz}$ which is actually greater than the hyperfine structure peaks separation ($\approx 100\,\mathrm{MHz}$).

Sub-Doppler spectroscopy

The sub-Doppler spectroscopy technique consists in overlapping, on the sample under investigation, two counterpropagating beams with the same frequency (ν_L). The atoms with a certain velocity component V_x along the beams direction "see" one of the two beams red-shifted in frequency and the other blue-shifted. Only the atoms with velocity $V_x = 0$ "see" the two

---

[20] In an analogous way of the *fine structure* energy levels – which arise from the $\boldsymbol{L} \cdot \boldsymbol{S}$ coupling of the (orbital $\boldsymbol{L}$ and spin $\boldsymbol{S}$) angular momenta related to the valency electrons – the energy levels splitting, called hyperfine structure, arises from the magnetic dipole coupling $H_{MD} = -\boldsymbol{\mu_I} \cdot \boldsymbol{B_J} \propto \boldsymbol{I} \cdot \boldsymbol{J}$ where $\boldsymbol{I}$ and $\boldsymbol{\mu_I} \propto \boldsymbol{I}$ are respectively the nuclear spin and the correspondent magnetic momentum while $\boldsymbol{J}$ and $\boldsymbol{B_J} \propto \boldsymbol{J}$ are respectively the total angular momentum and the magnetic field produced by the valency electrons on the nucleus.

beams with the same frequency. When the laser frequency coincides with the transition one ($\nu_L = \nu_0$), then both beams interact with the same atomic velocity class, that is the one with $V_x = 0$. Therefore, in correspondence of the frequency of interest ν_0, the absorption from the atoms (with $V_x = 0$) of the beam used for the investigation (called *probe beam)* is reduced because of the *saturation* induced by the other beam (called *pump beam)*: the atoms which have been excited by the pump beam are not able anymore (for a time equal to their *mean life*) to absorb the probe beam. As a result, a small Lorentzian peak "dug" within the larger gaussian peak (*Lamb dip*), appears.

3.2 Experimental setup

The 40 cm x 40 cm experimental setup of the LPSA is illustrated in figure 3.5. Once the laser light has been coupled into the optical fiber (OF), the

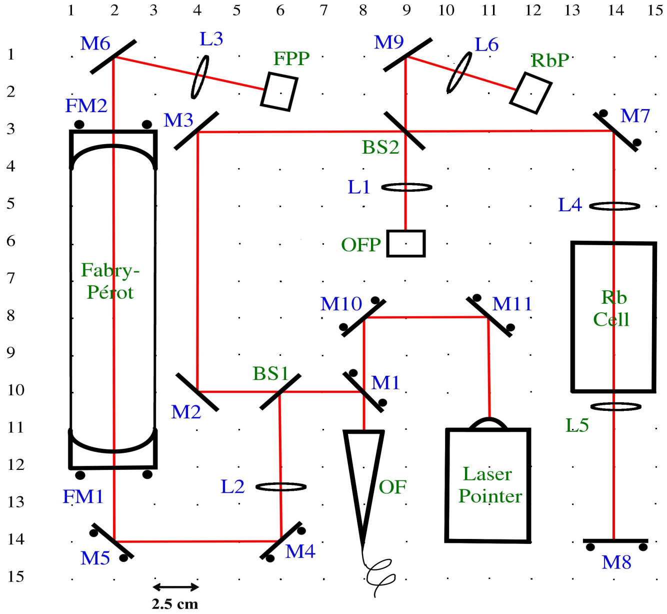

Figure 3.5: Experimental setup of the LPSA. Three main blocks can be seen: the interferometry and the spectroscopy ones and the part with the laser pointer. The size of the whole breadboard is 40 cm *x* 40 cm.

beam, which is reflected by the mirror M1[21], is split off by a 50/50 beam splitter ($BS1$): the reflected part is sent to the Fabry-Pérot interferometer (section 3.2.1) while the transmitted one is sent to a second beamsplitter ($BS2$): the transmitted beam reaches the spectroscopy setup (section 3.2.2), while the reflected one is focused (by the lens $L1$) into a photodetector (OFP). This photodetector, which has a changeable sensitivity[22], allows to monitor how much light is coupled into the optical fiber and therefore at disposal for the spectroscopy and the interferometry measurements.

3.2.1 Fabry-Pérot interferometer

A picture and a description of the Fabry-Pérot interferometer are presented in figure 3.6; for a design and a technical description of the optical cavity mount the reader is referred to appendix A. Still in the figure, the beam path – only for the interferometry part – is highlighted in red: the beam reflected by $BS1$ is sent and focused into the optical cavity by the mirrors $M4$ and $M5$ and the lens $L2$. The transmitted signal is then detected by the photodetector FPP after being focused by the short focal length lens $L3$.

Alignment of the optical cavity

The detected transmission signal – and therefore the status of the coupling – can be monitored on a oscilloscope while sweeping the cavity length with a triangle ramp signal[23] fed to the piezoelectric transducer which the mirror $FM1$ is mounted on.

In general, before – and so decoupled by – the two adjustable turning mirrors needed for the alignment, two lenses are required for a good *mode*

---

[21] As it will be shown in section 3.2.3, the mirror $M1$, whereas is reflective for IR light, it allows visible light to be transmitted.

[22] A complete description of the photodetector is presented in section 3.3.3.

[23] A description of the triangle ramp generator providing the signal to scan the cavity is reported in section 3.3.1. Note that one could get an analogous transmission signal by directly scanning the laser frequency but this could more easily cause the laser not to emit in single mode.

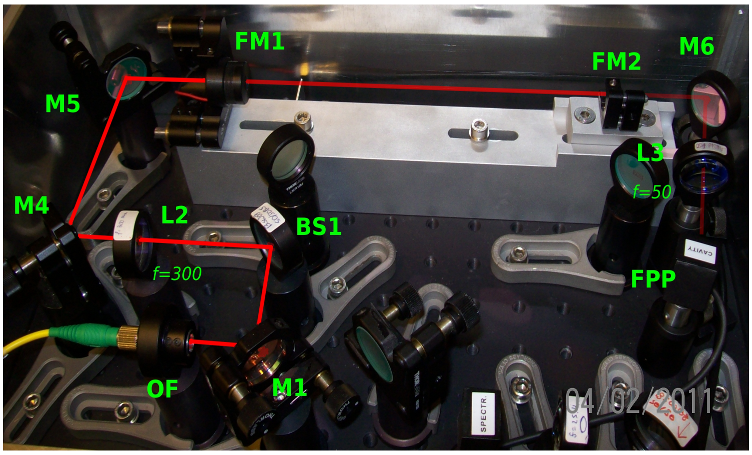

Figure 3.6: Picture of the Fabry-Pérot interferometer. The interferometer is composed of two equal spherical mirrors facing each other and with a radius of curvature of 20 cm; the mirror $FM1$ is mounted on a piezoelectric for sweeping the cavity length. The mirror $FM2$ sits on an extra mount which has the possibility to slide along a runner in order to provide the desired configuration: confocal when the extra mount is roughly at half of the runner and not confocal otherwise. The beam path relating only to the interferometry setup is highlighted in red.

matching. In this case, however, our single mode fiber provides a well collimated and round shaped beam which can nicely match the cavity mode with the use of only one lens ($L2$) sitting at a distance from the mirrors focus roughly equal to its focal length $f = 300\,\mathrm{mm}$. In other words, the mode matching has been achieved because the beam size and the lens focal length were such that the wavefront radius of curvature in correspondence of the input mirror $FM1$ approximately equaled that of the mirror itself[24].

In order to align the laser beam to the optical cavity, the mirrors $M4$ and $M5$ have been adjusted such that the beam hits the center of the cavity

---

[24] The wavefront radius of curvature for a gaussian beam propagating along the z direction is $R(z) = z\,[1 + (z_R/z)^2]$ where $z_R = \pi {w_0}^2/\lambda$ is the Rayleigh length: the wavefront is plane in the waist ($z = 0$) and becomes spherical for $z \gg z_R$. Since for a confocal cavity the mirror radius of curvature R_C equals the cavity length L, the mode matching condition is given by $R(L/2) = L$. This condition, for the given values $L = 200\,\mathrm{mm}$ and $\lambda = 780\,\mathrm{nm}$ sets the value of the waist w_0 at about $160\,\mu\mathrm{m}$. This means therefore that for a beam size $w_l \simeq 500\,\mu\mathrm{m}$ in correspondence of the lens, the focal length has to be chosen as $f = \frac{\pi\ w_l\ w_0}{\lambda} \simeq 300\,\mathrm{mm}$.

mirrors $FM1$ and $FM2$ respectively, and also such that the beam reflected by the first cavity mirror $FM1$ hits the furthest mirror ($M4$) at the same point as the incoming beam. After doing that the two mirrors before the interferometer have not been touched anymore and only the four degrees of freedom given by the cavity mirrors have been used.

For an interferometer to be aligned the beam axis must pass through the center of curvature of the two cavity mirrors, this means that each of the two mirrors must be perpendicular to the beam axis. In order to do that $FM1$ has been adjusted in such a way that the spots on its internal surface – due to the beam transmitted by $FM1$ and due to the back reflections from $FM2$ – overlapped. In an analogous way $FM2$ has been adjusted as well.

As the cavity mirrors – that were previously set roughly 20 cm apart – are not exactly in a confocal configuration, the transmission peaks look a bit asymmetric with a tail on one side. The cavity length has therefore been adjusted in such a way that the overlapping modes were completely degenerate.

When a first nice alignment is done, the (higher order) odd modes – which according to equation 3.15 in the transmission signal fall exactly in between the TEM_{00} modes and have their same height – start getting less intense in favour of the fundamental modes which consequently get higher. With fine adjustments the odd peaks can be reduced more and more to the extent of almost vanish. However, how much these modes can be reduced also depends on the quality of the mode matching. In section 3.4.1 (figure 3.13) will be shown a transmission signal where the ratio of the odd to the even mode peak height is less than 3%.

3.2.2 Saturation spectroscopy

Again with reference to figure 3.5 the beam transmitted by the beamsplitter $BS2$ is aligned and focused – by means of the mirror $M7$ and the lens $L4$ – into the cell containing Rb vapour. After being recollimated by the lens $L5$ the beam is reflected by the mirror $M8$ in such a way that it retraces the same path backwards to the beamsplitter: the transmitted part of the beam is unused while the reflected part is detected by the photodetector RbP after being focused by the lens $L6$. So in this very simple scheme the backreflected beam acts as a *probe* for the atoms saturated by the incoming beam (*pump beam*).

3.2.3 Laser pointer: trace for the alignment

As mentioned in chapter 3.1, for the LPSA to be a handy and practical tool, an additional setup involving a laser pointer[25] has been implemented: with reference to figure 3.7, the laser pointer produces a red (650 nm) and intense (≈ 40 mW) light beam which is coupled – by using the adjustable turning mirrors $M11$ and $M10$ – into the optical fiber. Note that the mirror $M1$, whose optical coating is active in the IR range and therefore for the

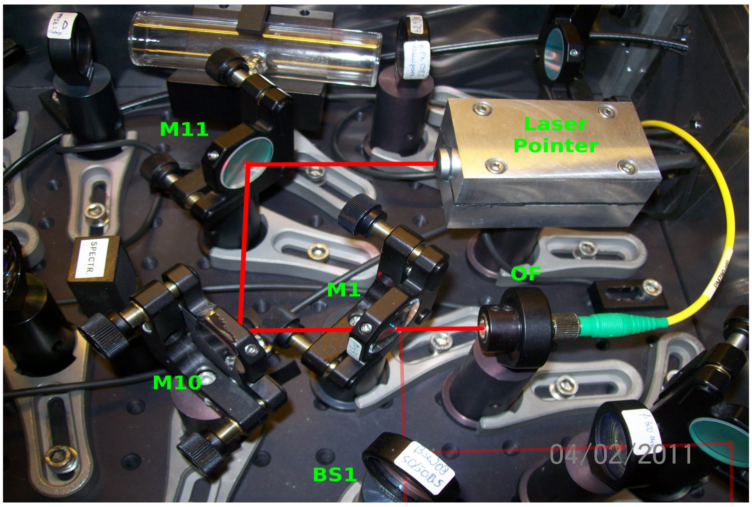

Figure 3.7: Picture of the laser pointer. The beam path of the visible light (650 nm) coming from the laser pointer and coupled into the optical fiber (OF) is highlighted in red. Instead, a semitransparent red is used to highlight the IR light coming from the optical fiber and reflected from the mirror $M1$ towards the optical cavity and the Rb cell.

---

[25] A description of the electronic circuit which supplies the laser pointer is given in section 3.3.2 while a design of the laser pointer mount can be found in appendix A.

light coming from the optical fiber, is quite transparent for the red light coming from the backside. With a coupling efficiency of about 70%[26] the optical fiber output can be used as a bright trace for the alignment of the (counterpropagating) laser beam that has to be analyzed: as long as the beam under investigation is not too diverging and doesn't quite match the fiber mode, the coupling into the optical fiber can be easily achieved by:

- using an adjustable turning mirror (together with an adjustable mount for the optical fiber) to overlap the counterpropagating beams in two points and get a signal on a scope connected to the photodetector OFP (see figure 3.5).
- improving the coupling by walking the beam.

3.3 Electronic circuit

A picture with a block diagram of the electronic circuit is shown in figure 3.8 while the correspondent circuit layout is reported in appendix B. The whole circuit is supplied by a 24 V AC wall power supply. A circuit – whose schematic is shown in appendix B – converts the AC signal into a DC signal which is then used to supply:

1) the triangle ramp generator (section 3.3.1). The triangle ramp signal is sent both to the Fabry-Pérot and – together with its trigger signal – to the oscilloscope.

2) a DC-DC converter which provides the opportune voltage for the laser pointer (section 3.3.2) to work.

3) the 3 photodetectors (section 3.3.3). The output signals from the photodetectors are conveniently low-pass filtered and then sent to the oscilloscope.

---

[26] Despite all the power losses due to the IR coating mirrors – roughly 80% efficiency for each reflection and 60% efficiency after the transmission – and due to the fiber coupling, the output power might still be too high/dangerous (about 9 mW), therefore if needed, a small on purpose made misalignment of the beam can provide the desired power.

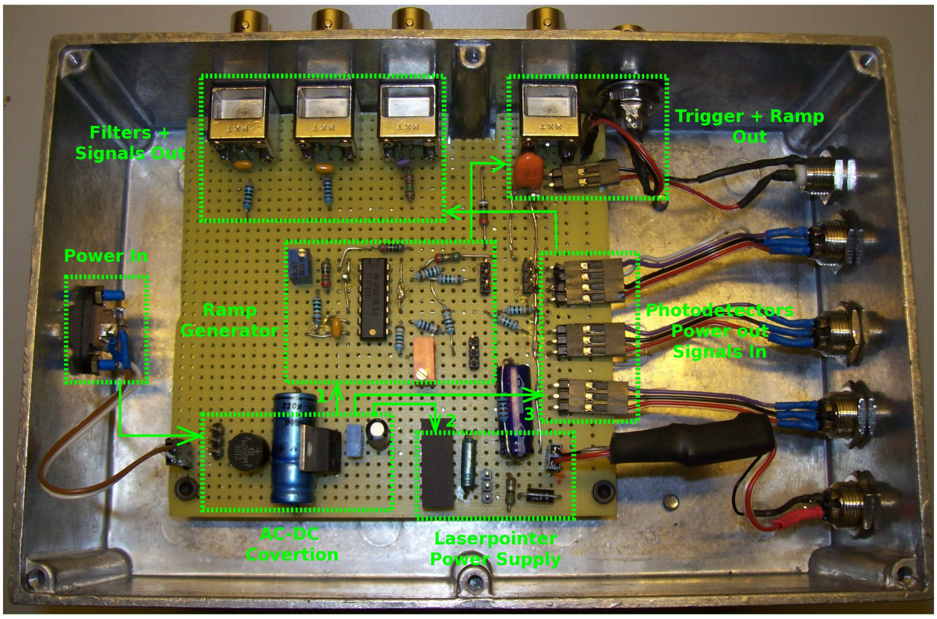

Figure 3.8: Picture of the electronic circuit. A block diagram of the circuit is highlighted in green. All the connectors for the cables going to the breadboard and to the oscilloscope can be seen respectively on the right and on the top.

3.3.1 Triangle ramp generator

The circuit schematic of the triangle ramp generator is shown in figure 3.9.

The whole circuit works with the use of only one IC – i.e. a quad operational amplifier ($TL074$) – supplied with 24 V. The first two operational amplifiers (op-amps) cooperate to provide both a *triangle ramp* ($OP2$ output) – which is needed for scanning the cavity length of the Fabry-Pérot interferometer – and a square wave ($OP1$ output), which is used as a trigger signal. The last two op-amps make the triangle ramp adjustable in *amplitude* ($OP3$) and in *offset* ($OP4$). The 1/2 voltage divider (bottom left) produces a 12 V signal which is used – instead of GND – as a *reference voltage* for all the op-amps.

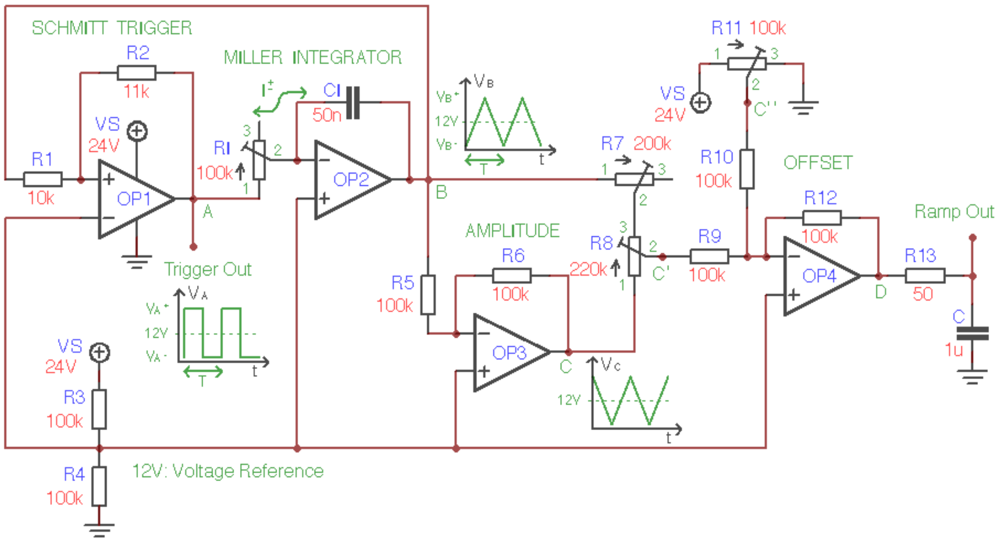

Figure 3.9: Schematic of the triangle ramp generator circuit. The first two operational amplifiers generate a square and a triangle wave signals. The last two ones make the triangle ramp adjustable respectively in amplitude and in offset. The reference voltage is set to 12 V.

Schmitt trigger and Miller integrator

The op-amp $OP2$ is a current integrator – also known as *Miller integrator* – that generates linear voltage ramps by *charging* and *discharging* the capacitor C_I with the constant current flowing through the resistance R_I given by (*Ohm's law*[27]):

$$I^{\pm} = \frac{V_A^{\pm} - 12\,V}{R_I} \tag{3.18}$$

The polarity of the current depends on the two possible constant outputs $V_A^{\pm}$ of the op-amp $OP1$. We will go back to $OP1$ in a while, for the moment let's simply consider the fact that $V_A^{+} \approx 24\,\mathrm{V}$ is larger than the voltage reference 12 V and that $V_A^{-} \approx 0\,V$ is smaller. If we assume that at a certain time $OP1$ is in the output state V_A^{-}, the corresponding negative current I^{-} flowing

---

[27] Note that the $OP2$ negative input is not at (virtual) ground but is set at the reference value 12 V of the positive input.

through C_I is integrated by $OP2$ producing a positive linear ramp:

$$\Delta V_B = -\int_{T/2} \frac{I^-}{C_I}\, dt = \frac{12\,V - V_A^-}{R_I C_I} \cdot \frac{T}{2} \tag{3.19}$$

where $T/2$ is the time of integration. If we suppose that after this time the $OP1$ output switches to V_A^+ (and as we will se this is exactly what the Schmitt trigger does), then $OP2$ will start producing the other half of the triangle ramp (again given by equation 3.19 but with opposite sign). When after an equivalent amount of time ($T/2$), $OP1$ switches again to V_A^-, a new cycle of period T starts.

For the piezoelectric to scan at least a FSR of the cavity, a ramp amplitude $|\Delta V_B| \approx 24\,\mathrm{V}$ is required. By using this value in equation 3.19 and solving for the reciprocal of T one gets a *ramp frequency*:

$$f \approx \frac{1}{4R_I C_I} \tag{3.20}$$

The $100\,k\Omega$ trimmer R_I therefore allows to choose the desired frequency: for a given capacitance $C_I = 50\,\mathrm{nF}$, R_I has been set (at approximately $50\,k\Omega$) in such a way to have a ramp frequency $f = 100\,\mathrm{Hz}$. Such a frequency is neither too high[28] for the piezoelectric to follow it nor too slow for having a convenient display on an analog oscilloscope.

Let's now consider the *Schmitt trigger* (i.e. the op-amp $OP1$) which, as we mentioned, produces a square wave signal. This happens because the op-amp $OP1$ behaves as a *comparator* for the two input signals V_+ and V_-[29]: when V_+ is larger than V_-, $OP1$ greatly amplifies this difference, bringing its output to its maximum value V_A^+ i.e. approximately the op-amp's positive power supply voltage (24 V). Analogously when V_+ becomes smaller than V_- the $OP1$ output switches to its minimum value V_A^- i.e. approximately the

---

[28] As it will be shown in section 3.3.3 (equation 3.27), the higher the scanning frequency f, the higher the photodetector bandwidth needed to resolve the Fabry-Pérot transmission signals.

[29] Note that, unlike all the other three op-amps in the circuit, $OP1$ doesn't have a negative feedback and therefore in general V_+ will be different than V_-.

negative power supply voltage ($0\,V$). As V_- is set to $12\,\mathrm{V}$, the positive input

$$V_+ = V_B \frac{R_2}{R_1 + R_2} + V_A \frac{R_1}{R_1 + R_2} \tag{3.21}$$

is a combination of both the feedbacks from the output state V_A and from the integrator output V_B[30]. Since the $OP1$ output states are two (V_{A^+} and V_{A^-}), there are two[31] values (*thresholds* V_{B^+} and V_{B^-}) for the input V_B that satisfy the switching condition $V_+ = V_-$, i.e.:

$$V_{B^\pm} = V_- \frac{R_1}{R_1 + R_2} - V_{A^\mp} \frac{R_1}{R_2} \tag{3.22}$$

In other words, as soon as the Miller integrator output V_B reaches the threshold V_{B^+} (V_{B^-}), the Schmitt trigger output switches to its high (low) value V_{A^+} (V_{A^-}) which in turn produces - as we saw - a ramp inversion.

Finally, R_1 and R_2 have been chosen different, because with the same value one of the two thresholds, let's say V_{B^+}, would be higher than the rail value V_{A^+}[32] (i.e. the maximum value for the op-amps), meaning that the integrator would start saturating without ever reaching the threshold and consequently the Schmitt trigger would never be able to perform the switching, preventing therefore the ramp inversion. To sum up, with R_2 slightly[33] bigger than $R1$, according to equations 3.22, one reduces the distances of the thresholds values V_{B^+} and V_{B^-} from the center value ($12\,\mathrm{V}$), preventing the integrator from saturating.

Amplitude and offset

For the triangle ramp to be suitable for the measurements (chapter 3.4), it must be adjustable both in amplitude and in offset. For the first aim, again

---

[30] Equation 3.21 can be obtained by considering that for the Ohm's law $V_+ = V_B - iR_1$ where $i = (V_B - V_A)/(R_1 + R_2)$ is the current flowing both through R_1 and R_2.

[31] Without (positive) feedback ($R_2 = \infty \implies i_2 = 0 \implies V_+ = V_B$) there would be only one threshold (i.e $V_{B_{th}} = V_-$) meaning that the square signal in this case would be irreparably compromised by the noise which would make the comparator switch continuously.

[32] Since the rails V_{A^+} and V_{A^-} are slightly asymmetric with respect to the center value 12V, if one puts $R_1 = R_2$ in equation 3.22, then finds out that for $|V_{A^-} - V_-| > |V_{A^+} - V_-|$, V_{B^+} is larger than V_{A^+}, while in the opposite case V_{B^-} is smaller than V_{A^-}.

[33] Note that if R_2 is chosen too big with respect to R_1, than the ramp amplitude $V_{B^+} - V_{B^-}$ becomes too small, compromising the suitable cavity length scan.

with reference to figure 3.9, the op-amp $OP3$ – together with a trimmer (R_7) and a one turn potentiometer (R_8) – has been used: $OP3$ works in the inverting configuration with unitary gain ($R_6 = R_5$) producing therefore a specular voltage around 12 V of the integrator output V_B, i.e[34].

$$V_C = 24\,V - V_B \tag{3.23}$$

Let's suppose for a moment to short R_7 (wiper in pin 1). In this case the amplitude of the R_8 output ranges from the maximum value of the V_A signal when the wiper is in pin 3, to 0 V (flat signal still centered at 12 V) when the wiper is at the center of the potentiometer. So in principle this configuration could work, nevertheless when the R_8 wiper is pushed toward pin 1 the ramp amplitude (flipped with respect to the 12 V reference) starts increasing again up to its maximum (V_C signal). This inconvenience can be overcome by setting the R_7 wiper in such a way that the lower limit of the amplitude is reached when the potentiometer R_8 is turned all the way through (i.e. with the wiper in 3). In this way, furthermore, the whole sensitivity of the potentiometer is used.

In order to add an *offset* to the adjustable amplitude triangle ramp, the op-amp $OP4$ – together with a 10 turns potentiometer (R_{11}) – has been used. The op-amp sums the two signals $V_{C'}$ and $V_{C''}$ after respectively the R_8 and R_{11} potentiometers, as follows[35]:

$$V_D = (24\,V - V_{C'}) + V_{off} \qquad\qquad V_{off} = 12\,V - V_{C''} \tag{3.24}$$

The term in brackets, again, is simply the specular image around 12 V of the adjustable amplitude triangle ramp $V_{C'}$. The second term (V_{off}) is the offset

---

[34] Equation 3.23 is obtained by considering that with $R_6 = R_5 = R$ for the Ohm's law $V_C = V_- - iR$ where $i = (V_A - V_-)/(R)$ is the current flowing both through R_5 and R_6 and V_- is the op-amp negative input which the op-amp itself tries to keep equal to the positive input i.e. 12 V.

[35] Equation 3.24 can be obtained by considering that for the Ohm's law $V_D = V_- - i_{12}R_{12}$ where V_- is the op-amp negative input which equals the positive input (12 V), and $i_{12} = i_9 + i_{10} = (V_{C'} - V_-)/R_9 + (V_{C''} - V_-)/R_{10}$ is the sum of the currents flowing respectively through R_9 and R_{10}. With $R_{12} = R_9 = R_{10}$ the result 3.24 is obtained.

contribution coming from the potentiometer R_{11}: this contribution ranges from $-12\,\mathrm{V}$ (wiper in 1) to $+12\,\mathrm{V}$ (wiper in 3).

Finally, the triangle ramp signal adjustable in amplitude and offset, passes through a low pass filter with a cutoff frequency $f_c = 1/(2\pi\, R_{13}C) = 2\,KHz \gg f$ which reduces the high frequency noise without appreciably smoothing the ramp edges[36].

3.3.2 Laser pointer power supply

The laser pointer that has been used as trace for the alignment to the optical fiber (section 3.2.3), is made in such a way to work with two batteries of $1.5\,\mathrm{V}$ each. To let the laser pointer work with the supply at disposal ($24\,\mathrm{V}$), a circuit with a $DC-DC$ converter to $3\,\mathrm{V}$ ($IF\,0505S$) has been implemented (figure 3.10), taking into account that the diode in the laser pointer is very sensitive to sudden variations in current and voltage[37].

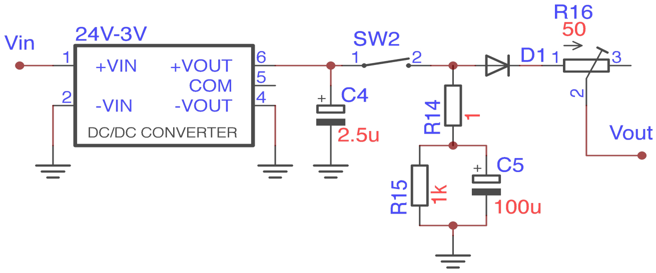

Figure 3.10: Circuit schematic of the laser pointer power supply. A DC-DC converter lowers down the voltage to the required value ($3\,\mathrm{V}$). Several precautions are then taken to prevent the laser pointer from being damaged.

After the capacitor C_4, which is used to buffer the ripple of the $DC-DC$ converter output voltage, the switch $SW2$ allows the laser pointer to be

---

[36] $R_{13} = 50\,\Omega$ has been chosen in such a way that it is low enough to prevent a high drop of voltage and, at the same time, high enough to prevent the op-amp from damage in case of an accidental short of the $OP4$ output to GND. C has been chosen consequently.

[37] Note that normally the laser pointer is "buffered" by the high capacitance of the batteries.

switched off after the alignment of the optical fiber. Besides avoiding to waste power, this is important as the (red) light back-reflected by the fiber coupler is aligned with the whole setup (see figure 3.5) and consequently affects all the measurements.

The series between R_{14} and the parallel $R_{15} - C_5$ is needed to smooth the spikes coming from the switch every time it is switched on and off. The spikes (high frequency signals) within the time constant $\tau = R_{14}C_5 = 100\,\mu\text{s}$ are absorbed by the capacitor, preventing therefore the laser pointer from the risk of being damaged[38].

Since the $DC - DC$ converter actual output (3.3 V without load) was still a bit high, a Si diode ($D1$) – which causes a voltage drop of $\approx 0.6\,\text{V}$[39] – has been used. Despite the supply voltage (2.7 V) was less than the required one, the laser pointer output power (above 50 mW) was too high: as a last precaution, a $50\,\Omega$ trimmer has been used in series before the laser pointer in order to lower its power down to $\approx 40\,\text{mW}$.

3.3.3 Photodetectors

In order to monitor the light coupled into the optical fiber and to detect the signals from the Rb cell and the optical cavity, three photodetectors have been built. The use – for all of them – of an integrated circuit (OPT101) – that is a photodiode with on-chip transimpedance amplifier and that stands 24 V as power supply – made possible the circuits to be very simple and the physical sizes to be quite limited (3 x 2 x 1.5 cm^3). The circuit schematic of the photodetector for the Rb spectroscopy is shown in figure 3.11 (on the left). On the right of the same figure a picture (from behind) of one of the

---

[38] Note that $R_{14} = 1\Omega$ has been chosen in such a way that it is low enough to prevent too much current to flow in the laser pointer and, at the same time, high enough to prevent the $DC - DC$ converter output current ($I = 3.3\,V/1\,\Omega = 3.3\,\text{A}$) from damaging it. Note also that, when the circuit is open (and without load), R_{15} allows C_5 to discharge fast enough ($\tau = 100\,\text{ms}$) without allowing a significant amount of current coming from the converter to pass through ($R_{15} \gg R_{laserpointer}$).

[39] 0.6 V is approximately the direct bias voltage needed for Si diodes to start conducting. Note that due to the exponential shape of the diode $I - V$ curve, no matter how intense the current, the voltage drop keeps almost the same.

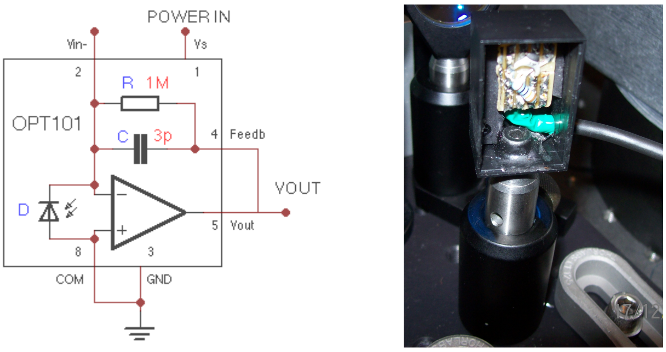

Figure 3.11: Circuit schematic of the photodetector for the Rb spectroscopy (left). The chip – composed of a photodiode and a transimpedance op-amp – has also been used with an external resistance to increase the bandwidth for the Fabry-Pérot photodetector. A picture of the latter one is also shown (right).

photodetectors is shown as well. With reference to the schematic, the light is detected by the photodiode D and the (current) signal is amplified by the op-amp in inverting configuration with a nominal gain factor of $10^6\,V/A$ and a nominal bandwidth of 23 kHz.

As for the Fabry-Pérot photodetector, it must be fast enough to resolve the width ($\gamma \approx 600\,\mathrm{MHz}$) of the resonance curve during the scan across it. If we define the scanning rate of the piezo over a frequency range $\Delta\nu$ – let's say – of a FSR as[40]

$$\alpha = 2f \cdot \Delta\nu = 150\,GHz \tag{3.25}$$

the time over which the Fabry-Pérot is on resonance during the scan of the cavity length is[41]:

$$\tau_{res} = \gamma/\alpha \approx 4\,\mu s \tag{3.26}$$

The photodetector bandwidth BW must be then grater than

$$BWmin = \gamma \cdot \frac{\tau_s}{\tau_{res}} \approx 39\,kHz \tag{3.27}$$

---

[40] The factor 2 in equation 3.25 arises from the fact that the scan is only over half ramp period $1/f$.

[41] In other words, τ_{res} is the time over which the cavity length is such that, according to equation 3.1, the light can constructively interfere and be transmitted.

where, according to equation 3.11, $\tau_s \simeq 1/(2\pi\gamma) \approx 260\,\text{ns}$ is the cavity storage time[42]. As a consequence, for the cavity signal features not to be limited by the finite bandwidth of the photodetector, its gain has been reduced[43]. This has been achieved by simply connecting – as feedback for the op-amp – an external resistor of $100\,k\Omega$ between pins 2 and 5 of the IC. As a result, a reduction by a factor of ten in the gain, led – according to the datasheet – to a bandwidth twice higher ($BW = 44\,\text{kHz}$).

Monitor photodetector: switching the sensitivity

For monitoring the light coupled into the optical fiber, a photodetector with adjustable sensitivity has been built. This required the use of an extra

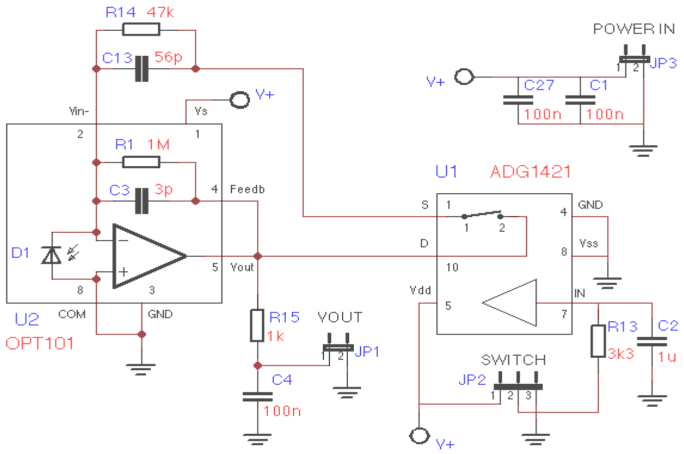

Figure 3.12: Circuit schematic for the photodetector monitoring the light coupled into the optical fiber. Besides the monolithic photodiode with on-chip transimpedance op-amp, an analog switch is used to allow a reduction of the photodetector gain.

IC – i.e. an analog switch ($ADG1421$) – which allows reducing the photodetector gain when the quantity of light coupled into the optical fiber is too

---

[42] Note that since ($\tau_{res} \gg \tau_s$) the light intensity is stationary at every point of the resonance curve during the scan, meaning that the linewidth can't be broadened by the cavity.

[43] The criterion 3.27 ensures that even when the scan is performed over the full FSR the peaks are not broadened by more than a factor of 2.

high and the photodiode saturates. A schematic of the circuit is shown in figure 3.12 while its layout is reported in appendix B. In normal conditions, the $OPT101$ chip works in the same way as for the spectroscopy photodetector, i.e. with a gain of $10^6\,V/A$ given by its internal resistor R_1. When, by means of a mechanical switch, a signal V_+ (which as usual is the 24 V voltage supply) is sent to the analog switch (pin 5), the device closes the circuit by shorting pins 1 and 10. As a result, the op-amp's external resistance $R_{14} = 47\,k\Omega$ is connected in parallel with the much higher internal resistance ($R_1 = 1\,M\Omega$) leading to a gain for the photodetector about 20 times lower.

A low pass filter for both the analog switch input (IN) and for the photodetector output, has been used. The former to "buffer" the analog switch, the latter (with a cut-off frequency $f_c = 1/(2\pi C_4 R_{15}) \simeq 3\,\mathrm{kHz}$) to reduce the high frequency noise.

3.4 Measurements and data analysis

In order to perform the measurements with the LPSA, some light from the beam paths of the lasers used for the BEC, has been diverted and coupled into the optical fiber of the spectrum analyzer according to the procedure described in section 3.2.3.

3.4.1 Characterizing the Fabry-Pérot

By applying a voltage ramp to scan the cavity piezo, several Fabry-Pérot transmission signals have been recorded. One of them showing two peaks defining the optical cavity FSR is reported in figure 3.13[44]. As it can be seen, a FSR of the cavity can be scanned by the piezo with a voltage ramp of $(10.50 \pm 0.05)\mathrm{V}$[45]. This result can be used as a *calibration* factor

---

[44] Note that the time scale provided by the oscilloscope has been converted into a frequency scale by using the known value ($FSR = 750\,\mathrm{MHz}$) for the frequency difference between the two peaks.

[45] The voltage value and its error – which is mostly due to the non perfect linearity of the voltage ramp – have been calculated respectively as the mean value and the standard deviation obtained from 10 measurements.

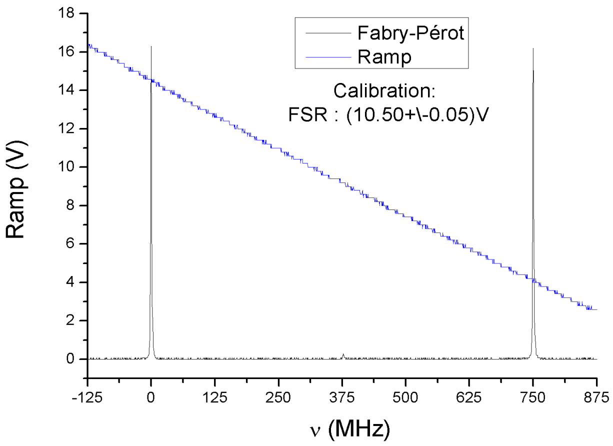

Figure 3.13: Transmission signal of the confocal Fabry-Pérot interferometer with two peaks defining the FSR and the much less intense ($\approx 3\%$) odd modes peak lying exactly at halfway. Note that, as the Fabry-Pérot does *not* provide an *absolute* frequency value, the origin of the frequency scale has been chosen arbitrarily in correspondence of the first peak. The calibration given by the voltage ramp needed to scan a FSR is also shown.

($71.4 MHz/V$) to measure the linewidth of the transmission peaks and therefore calculate the Fabry-Pérot Finesse.

Finesse measurements

In measuring the linewidth, care was taken to zoom-in on the peak (figure 3.14) not by decreasing the oscilloscope time scale but rather by decreasing the ramp voltage amplitude in such a way that the broadening of the peak, due to the quite high scanning rate α of the piezo (equation 3.25), reduced. By using the voltage ramp with the voltage-frequency conversion factor, the x-scale (with arbitrary origin) has been calibrated.

In agreement with equation 3.9 a Lorentzian fit has been performed. The repetition of the procedure for ten acquisitions led to a mean value of the *linewidth* of

$$\gamma = (1.36 \pm 0.18) MHz \tag{3.28}$$

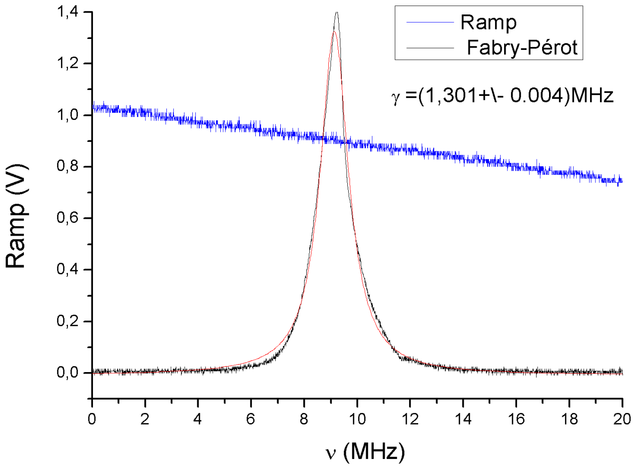

Figure 3.14: Transmission peak of the Fabry-Pérot interferometer. The voltage ramp, together with the calibration factor given in the previous figure, are used to calibrate the frequency axis. The peak linewidth γ ($FWHM$) resulting from a Lorentzian fit is also reported.

where the error is not that one calculated by the fit procedure[46] shown in figure, but arises from the statistics. According to equation 3.10, this linewidth corresponds to a *Finesse*:

$$F \approx 600 \tag{3.29}$$

that is about two times lower than the theoretical one (equation 3.5). One of the main reasons why the experimental linewidth results (about two times) broader than the theoretical one ($\gamma_{th} \approx 600\,\mathrm{kHz}$) most likely is the fact that what one actually measures is not simply the cavity transmission peak but rather its convolution with the laser one[47]. Another reason explaining this broadening could be the diffraction losses of the cavity (see note 5).

A measurement of the Finesse has also been performed by using a laser whose amplitude modulation produces first order *sidebands* 10 MHz apart

---

[46] Note that as the fit procedure doesn't take into account the correlation between the fit degrees of freedom, its error is reasonably underestimated.

[47] By a beatnote measurement the laser linewidth resulted to be less than 500 kHz and if we suppose both the peak shapes to be Lorentzian, then their linewidths must be summed linearly.

from the carrier (figure 3.15). As the distance between the peaks is known

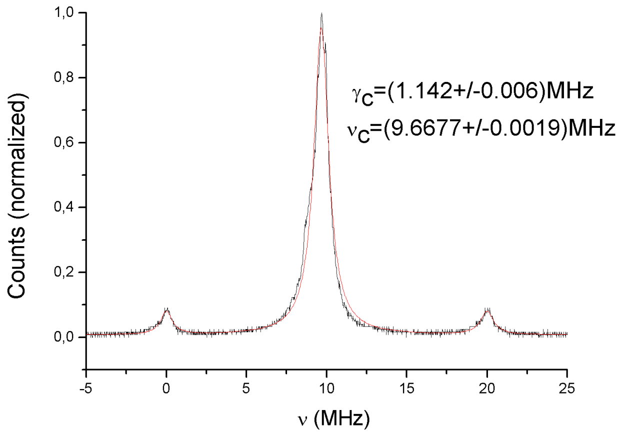

Figure 3.15: Transmission peak of the Fabry-Pérot interferometer with 10 MHz sidebands. The sidebands provide a convenient frequency reference for the measurement of the *carrier* linewidth γ_c. The three peaks are fitted with Lorentzian functions.

such sidebands allow for a direct calibration of the x-axis. The statistics over ten measurements led to a linewidth $\gamma = (1.31 \pm 0.12)$MHz that is consistent with 3.28.

Non confocal configuration

By displacing the mirror sitting on the cavity extra mount (figures 3.6, 13) up to its edge, i.e by a quantity $\delta \simeq 1.25\,\text{cm}$, the Fabry-Pérot has been set up in a *non confocal* configuration. A spectrum corresponding to such configuration is shown in figure 3.16 (on the left). On the right of the same figure, a zoom-in on the even k modes is shown as well. The transverse TEM_{pl} modes – that are not mode degenerate any longer – are displaced – with respect to the longitudinal modes – according to equation 3.14. In particular, with a separation of the mirrors $L = R_C + \delta$, the frequency shift of the second order modes ($k = 2$), can be approximated for $\delta \ll R_C$ as

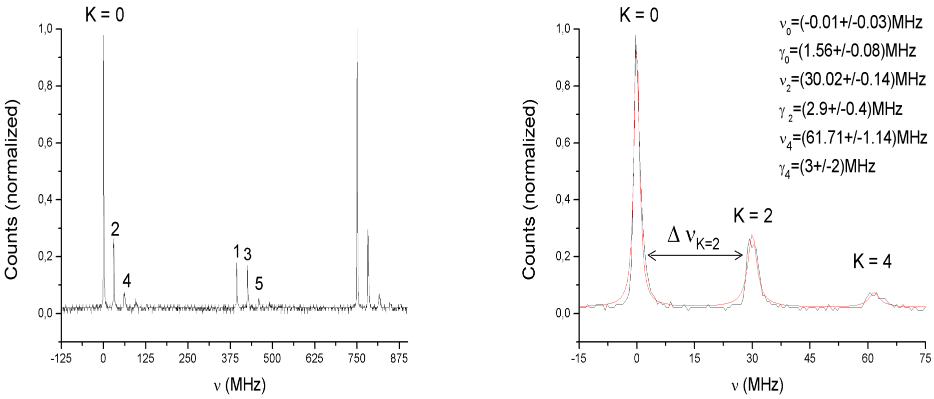

Figure 3.16: Fabry-Pérot spectrum for a non confocal configuration with $L \gtrsim R_C$. A set of even and a set of odd transverse modes are visible (left); a zoom-in on the former ones is also shown (right). A fit with three Lorentzian functions provides the relative distance between the even modes and highlights the peak broadenings due to the fine splitting of the transverse modes.

follows[48]:

$$\Delta\nu_{k=2} \approx \frac{c}{2L}\,\frac{2\,\delta}{\pi R_C} \simeq 30\,MHz \qquad (3.30)$$

This result is in agreement with that one obtained with the fit reported in figure.

Note also the fine splitting of the higher order modes that, according to equation 3.13, should be degenerate[49]. As a matter of fact, especially in high Finesse cavities, this degeneracy is removed when any detachment of the mirror surfaces shape from the spherical one occurs (symmetry breaking).

Finally note the asymmetry of the longitudinal mode: in agreement with what said in section 3.3.3 for a scan of a full FSR, the tail at the right side of the peak is due to the finite detector speed.

---

[48] If $L = R_C + \delta$ with $\delta \ll R_C$ the *arccos* function in equation 3.14 can be expanded as $arcocos(-\delta/R_C) = \pi/2 - arcsin(-\delta/R_C) \approx \pi/2 + \delta/R_C$. By taking into account that the Airy function repeats itself after each FSR, the result 3.30 is easily obtained.

[49] For instance, in the $k = 2$ peak, two TEM_{pl} modes are actually distinguishable, i.e. the TEM_{10} and the TEM_{02} modes.

3.4.2 Rb saturation spectroscopy

The Rb saturation spectroscopy signals can be obtained by turning off the voltage ramp of the cavity piezo and by directly scanning the frequency of the laser light ($\lambda = 780\,\text{nm}$) coupled into the optical fiber of the LPSA. This frequency scan has been achieved by applying a voltage ramp to the piezo of the laser grating. While monitoring on the oscilloscope (trigged at the scanning frequency) the signals coming from both the interferometer and the Rb cell, the laser parameters – such as the injection current, the voltage offset applied to the piezo of the laser grating and if necessary the temperature – have been adjusted in order to change the laser frequency and find the Rb D_2 absorption lines. As an example the line correspondent to the transition from the level $F = 2$ of the ^{87}Rb is shown – together with the Fabry-Pérot transmission signal – in figure 3.17. The Fabry-Pérot transmission signal has been used to calibrate the frequency axis. Note that three

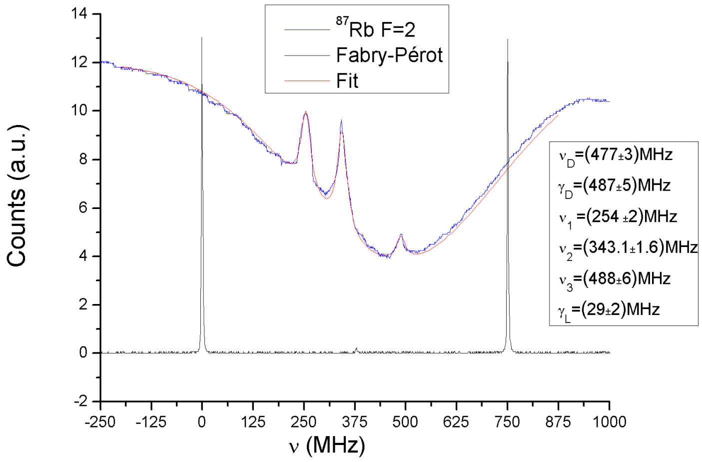

Figure 3.17: Sub-Doppler absorption spectrum correspondent to the transition from the level $F = 2$ of the ^{87}Rb and related Fabry-Pérot spectrum used for the calibration of the frequency axis. A fit with a function combination of a Gaussian function for the Doppler background and three Lorentzian functions for the visible Lamb-dips, is reported in red.

(out of six[50]) hyperfine structure peaks are probably too weak to be clearly distinguished within the Doppler background. As a consequence a fit with a combination of a Gaussian function and only three Lorentzian functions has been performed[51]. The resulting peaks (relative) positions and linewidths are shown in figure 3.17. Note that, in agreement with the predictions (equation 3.17), the Doppler linewidth is $\gamma_D = (487 \pm 5)\,\mathrm{MHz}$.

3.4.3 Other applications

One of the main applications of the LPSA is the study of the spectrum purity of the slave lasers used for the achievement of the BEC. For a slave laser to inherit the spectral properties of the single-mode master laser which feeds it, the injection parameters – such as both the angle and the power of injection and both the current and the temperature of the slave laser – must be chosen suitably. In this frame the LPSA provides an effective way to monitor[52] the injection of the slave lasers: it allows to check whether the slave laser is operating in single or multi-mode and to assess, in particular, the stability of the single-mode behavior over an enough wide range of the injection parameters. An example of multi-mode spectrum is reported in figure 3.18.

---

[50] Due to the selection rules the $F = 2$ hyperfine transitions for the D_2 lines are 6: 3 of them towards real levels ($F' = 1, 2, 3$) and other 3 towards fictitious levels which lie exactly halfway of the real ones. The latter ones, called *cross-over* transitions, are made possible by those atoms whose velocity along the counterpropagating beams direction is such that they see both beams (one blue-shifted and the other red-shifted) at resonance frequencies.

[51] As mentioned in section 3.1.2, the thermal agitation of the atoms in the gas leads to a Gaussian-like broadening, whereas the sub-Doppler spectroscopy one is an homogeneous Lorentzian-like broadening due to the fact that all the atomic classes behave statistically in the same way.

[52] Usually the injection of the slave laser is monitored by means of a fluorescence signal from a Rb cell which the slave laser beam is directed through. As the injected laser current is modulated, spikes or dips in the fluorescence signal indicate that the laser is operating in multi-mode, whereas a large plateau in the signal suggests stable single-mode behavior. Nevertheless such procedure doesn't give a high degree of confidence about the stability of the laser operating in single-mode.

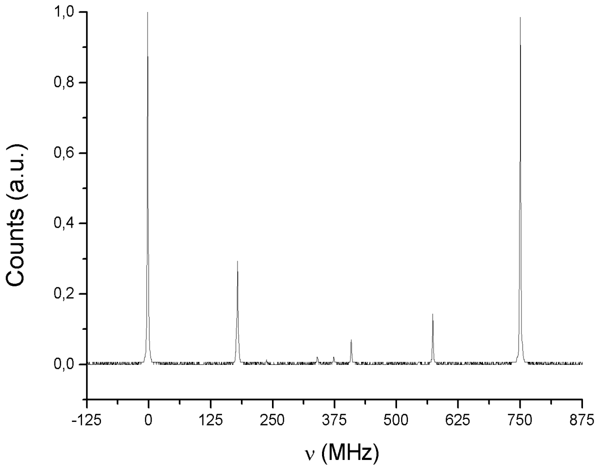

Figure 3.18: (Confocal) Fabry-Pérot spectrum for a laser operating in multi-mode. Besides the longitudinal cavity modes (the two highest peaks) and the odd modes peak (exactly at halfway), many other laser modes are visible.

Besides the slave lasers, the LPSA is also used to monitor the spectrum purity of other diode lasers. For instance, when the lasers investigating the BEC must be tuned in frequency (by adjusting the current and the temperature), part of the light used for the experiment can be sent to the LPSA in order to check, for each frequency, the mode behavior of the laser.

CHAPTER 4

Experimental study of the $\Delta - U$ phase diagram

Contents

In this Chapter we will describe the experimental procedures that we have followed to investigate the phase diagram of a disordered system of ultracold bosonic atoms. In particular, after briefly reporting how we produce a ^{39}K BEC with tunable interaction, we will show the experimental techniques implemented to produce a set of quasi-1D systems with a quasi-periodic optical potential. We will finally report the measurements of the momentum distribution of the atomic sample for different levels of disorder and interaction strength, which provide a first evidence of the phase diagram of the disordered system both in the regime of weak and strong interactions.

4.1 Experimental production of the BEC

The starting point of the experiments described in this thesis is a BEC of Potassium-39 with tunable interactions [44]. ^{39}K has a natural negative scattering length [64][65], corresponding to an attractive interaction, which, as mentioned in subsection 1.1.2, would make the BEC collapse [66][67][68]. Nevertheless, by using a Feshbach resonance, it is possible not only to condense ^{39}K, by tuning the scattering length to positive values, but also to suitably control the interaction energy and reduce it almost to zero. Due to the presence of both a broad resonance and a small background scattering length [69], ^{39}K is actually an excellent sample for the production of a weakly interacting BEC.

At zero magnetic field the collisional properties of ^{39}K do not favour direct evaporative cooling [70][71]. However it is possible to use ^{87}Rb in order to sympathetically cool ^{39}K. In spite of the small heteronuclear scattering length for the ^{39}K - ^{87}Rb collisions [72][73], the sympathetic cooling for ^{39}K has been proven to work efficiently [71]. The experimental setup that has been used to produce the ^{39}K BEC is largely described in previous theses at the "BEC-2" laboratory at LENS [74][75][76][77][78]. In the following we report only a brief summary of the steps performed to experimentally produce the BEC [20]:

1. Laser cooling and trapping of ^{87}Rb and ^{39}K atoms in a magneto-optical trap (MOT) [79].

2. Transfer via optical pumping of the two samples in the magnetically trappable Zeeman state $|F = 2, m = 2\rangle$ (see figure 4.1 for the hyperfine and Zeeman structure of ^{39}K, the case of ^{87}Rb being analogous).

3. Loading of the ^{39}K - ^{87}Rb mixture in a pure (quic) magnetic trap with an average harmonic trap frequency of about 100 Hz.

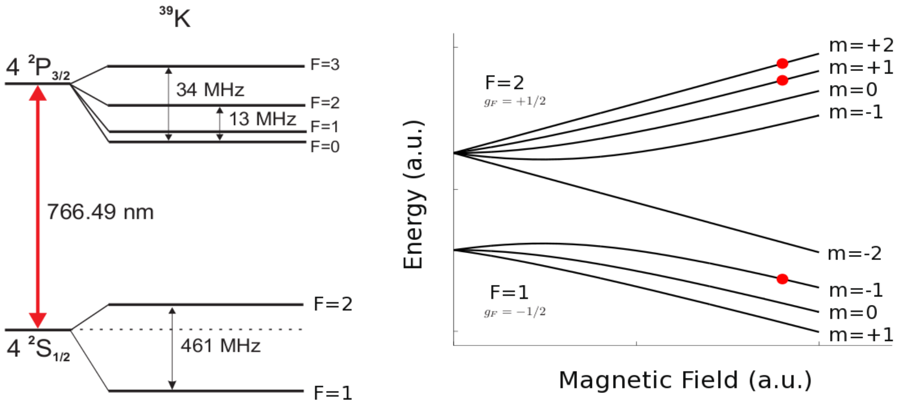

Figure 4.1: Hyperfine structure (**left**) and Zeeman shift of the ground state levels $|F=1\rangle$ and $|F=2\rangle$ (**right**) of ^{39}K. The red dots show the magnetically trappable states.

4. Selective μ-wave evaporation of ^{87}Rb atoms and sympathetic cooling of ^{39}K ones, via ^{87}Rb - ^{39}K collisions. The temperature of the mixture is lowered from about $100\,\mu$K down to $T \approx 1\,\mu$K. At this point it is necessary to use Feshbach resonances in order to further cool down ^{39}K atoms. A different kind of trapping potential, which is compatible with the application of the Feshbach magnetic field, is thus required.

5. Loading of the atoms into an optical dipole trap, which, in agreement with the procedure described in subsection 1.2, is produced with two cross-focused laser beams red-detuned at wavelength $\lambda = 1032\,$nm and with an average harmonic trap frequency of about $50\,$Hz. The experimental setup is sketched in figure 4.2.

6. Transfer of both the ^{87}Rb and ^{39}K atoms in the absolute ground state $|F=1, m=1\rangle$ where ^{39}K has a broad Feshbach resonance around $400\,$G.

7. An homogeneous magnetic field (Feshbach field) is applied in order to tune inter- and intra-specimens interactions. Atoms are further cooled down by reducing the intensity of the optical trap (optical evaporative cooling). The evaporation in the optical trap is performed in two steps.

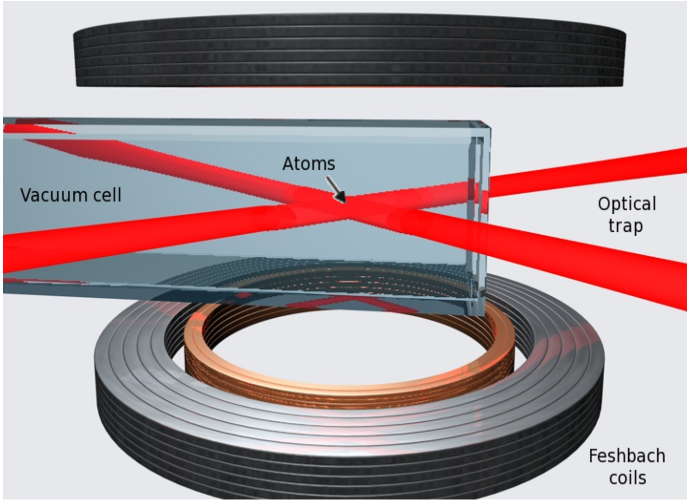

Figure 4.2: Experimental setup. The optical dipole trap is created by means of two focused laser beams (waist $w_0 = 100\,\mu\text{m}$) with $\lambda = 1032\,\text{nm}$, crossing on the horizontal plane. The Feshbach magnetic field B is generated by a couple of coils in Helmholtz configuration with axis in the vertical direction. B can be tuned in the range of $0 \div 1000\,\text{G}$ with an uncertainty $\Delta B \lesssim 0.1\,\text{G}$.

- Firstly the magnetic field is tuned to one of the several heteronuclear Feshbach resonances existing in this mixture [73] (see the blue curve in figure 4.3), resulting in a larger rate of collisions between ^{87}Rb and ^{39}K atoms. The evaporation is performed in order to evaporate atoms in the vertical direction, meaning that mainly the heavier ^{87}Rb atoms evaporate. ^{39}K in this first step is thus sympathetically cooled.
- The magnetic field is then tuned to the homonuclear Feshbach resonance [77] (black curve) in order to get a positive value of a. In this second step, in which ^{87}Rb has completely evaporated from the trap, the cooling of ^{39}K relies only on intraspecies collisions.

Weakly interacting ^{39}K condensate

Once the BEC has been produced (with a typical number of atoms $N \approx 50\,000$), a can be further tuned in order to get a weakly interacting

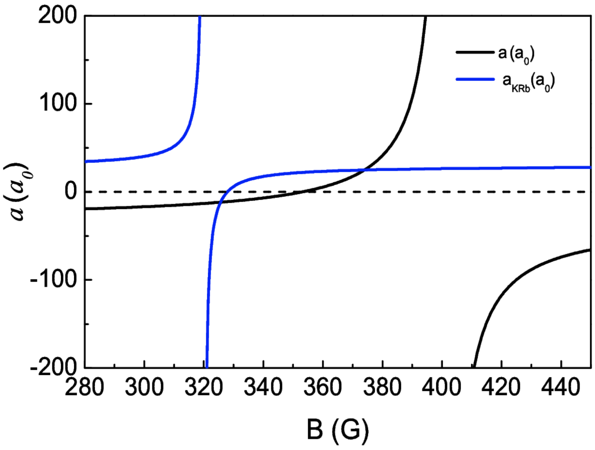

Figure 4.3: Magnetic field dependance of the heteronuclear scattering length a_{Rb-K} (blue curve) and of the homonuclear scattering length a (black curve). The first part of evaporation is performed at the heteronuclear Feshbach resonance ($B = 316\,\mathrm{G}$) where $a = -33\,a_0$ and $a_{Rb-K} = 150\,a_0$. The second part of the evaporation is performed at the homonuclear resonance ($B = 395.2\,\mathrm{G}$) where $a = 180\,a_0$ and $a_{Rb-K} = 28\,a_0$. Figure taken from [20].

condensate. Starting from a magnetic field value $B = 395\,\mathrm{G}$ slightly below the $|1,1\rangle$ resonance, where $a = 180\,a_0$ has been used for the ^{39}K evaporation process, B can be lowered adiabatically[1] down to a value, within the field range 350 G - 395 G, where the scattering length is positive and the condensate is stable. As described in subsection 1.1.3, due to the small ratio a_{bg}/Δ in the $|1,1\rangle$ resonance close to 400 G, the degree of control in the interaction energy is very high[2], the sensitivity around $B_{zc} = 350\,\mathrm{G}$ being $da/dB \simeq 0.56\,a_0/G$. In particular, in our experimental setup the stability of the Feshbach magnetic field is of the order of 0.1 G, meaning that a can be tuned to zero with an uncertainty $\Delta a \lesssim 0.1\,a_0$[3].

---

[1] B is lowered down with a ramp that is a combination between a linear and an exponential ramp in about 100 ms in order to reduce the heating of the atomic cloud.

[2] This degree of control is better than that of most other species, which have narrower resonances Δ and/or larger background scattering lengths a_{bg}. The only sample that could be better than ^{39}K in order to control a around the zero crossing is ^{7}Li [69].

[3] A possible way to accurately approach the zero-crossing magnetic field B_{zc} it is to measure the energy released from the condensate during the expansion from the trapping

4.2 Experimental setup

A 3D optical lattice is produced by means of the laser light generated by a solid state Nd:YAG laser. Such a laser, which is optically pumped by a diode laser, is a very stable and powerful source characterized by a spectral linewidth $\Delta\nu \lesssim 1\,\mathrm{kHz}$ and a maximum emission power $P \simeq 10\,\mathrm{W}$. In agreement with what discussed in subsection 1.2, the laser light wavelength, $\lambda_1 = 1064\,\mathrm{nm}$, is red-shifted with respect to the ^{39}K resonance wavelength, $\lambda_0 = 766.1\,\mathrm{nm}$, in such a way that the atoms can be suitably trapped with the power provided by the laser.

The beam of the Nd:YAG laser is split in three parts by means of $\lambda/2$ waveplates and polarizing beamsplitter cubes. The power of each laser beam is controlled by means of acusto-optical modulators (AOMs), which can be used as fast switches with a commutation time of the order of $10\,\mu\mathrm{s}$. Moreover, such devices, by diffracting the laser light with an acoustic wave at frequency $\omega_A \simeq 80\,\mathrm{MHz}$, allow to shift the laser frequency up to $\pm\,\omega_A$. Each laser beam is then coupled into a polarization-maintaining optical fiber which spatially filter them. With a power of about 1 W out of the optical fiber (when the AOMs are completely open), each beam is sent to the cell with the atoms and then retro-reflected in order to produce the stationary wave forming the optical lattice. Both the incoming and the retro-reflected beams are focused by lenses on the atomic sample with a waist $w_0 \approx 100\,\mu\mathrm{m}$, resulting in an average trap frequency $\omega \simeq 75\,\mathrm{Hz}$. Undesired interference between the laser beams forming the lattices in the three directions can be prevented by rotating the linear polarizations coming out of the fibers in such a way that they are orthogonal with respect to each other. For the same aim, the frequency of the three beams are shifted by $\sim 10\,\mathrm{MHz}$ with respect to each other by means of the AOMs.

In order to produce a disordering optical lattice another laser is required:

---

potential. However, minimizing the decoherence induced by interactions during a Bloch oscillation into a vertical lattice results in a more sensitive procedure [20].

a Ti:Sapphire laser of wavelength $\lambda_2 = 859.6\,\mathrm{nm}$ and variable power up to $P \approx 200\,\mathrm{mW}$ is thus employed. The Ti:Sapphire laser beam, whose power is controlled by an AOM, is sent to the cell with the atoms and superimposed to the 3D optical lattice along the vertical direction. Both the incoming and retro-reflected beams are focused in correspondence of the atomic cloud position with a waist of about $100\,\mu\mathrm{m}$.

4.2.1 The optical lattice setup

With reference to figure 4.4 we describe in this subsection the optical lattice setup employed in the experiments.

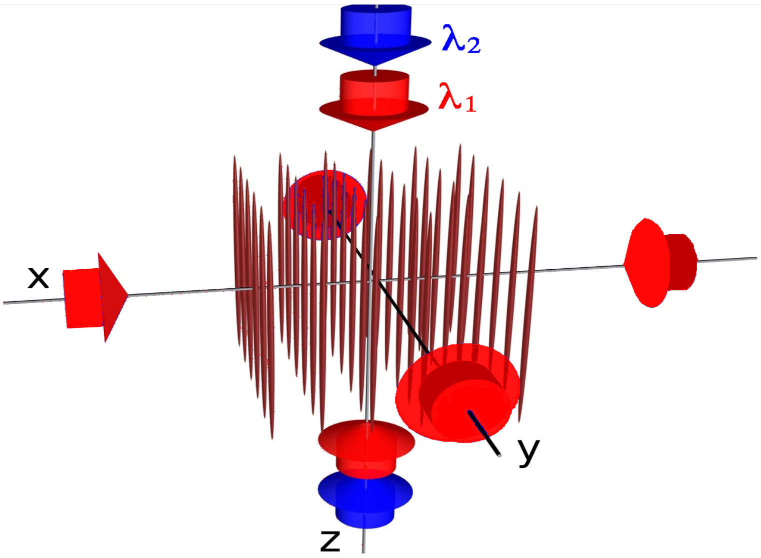

Figure 4.4: Optical lattice potentials. The two horizontal optical lattices ($\hat{x}$ and $\hat{y}$ directions) provide a tight confinement forming an array of 1D independent vertical potential tubes. The vertical quasiperiodic optical potential is formed by superimposing two incommensurate optical lattices: the main one ($\lambda_1 = 1064\,\mathrm{nm}$), which is related to the tunneling energy J, and the secondary one ($\lambda_2 = 859.6\,\mathrm{nm}$), which is related to the disorder amplitude Δ.

Confining optical lattice. By means of a strong 2D optical lattice ($s_x, s_y \simeq 30$) along the $\hat{x}$ and $\hat{y}$ directions, we can produce an array of 1D potential tubes along the $\hat{z}$ direction. Typically, out of a sample of $N \approx 50\,000$ atoms we get approximately $N_{tubes} \approx 500$ tubes with an average number of atoms $\bar{n}_{tube} \approx 100$ each[4]. Since the tunneling of the single particle between different tubes is suppressed on the time scale $t_{exp} \sim 100\,\mathrm{ms}$ of the experiments (i.e. $h/J_{x,y} \sim 1\,s \gg t_{exp}$), we can study the physics along the tubes which can be reasonably thought of as 1D systems (see section 2.5). Moreover, due to the strong confinement along the $\hat{x}$ and $\hat{y}$ directions ($\omega_x = \omega_y \simeq 30\,kHz$) and due to the consequent high density of particles in the tubes, it is possible, by increasing the scattering length with the Feshbach magnetic field, to study the system in a regime of strong interactions[5].

Main optical lattice. Along the tubes direction ($\hat{z}$ direction), we employ the same laser source used for the 2D confining lattice to produce the main optical lattice with spacing $d = \lambda_1/2 \simeq 532\,nm$ and height $s_1 \simeq 10$. According to equation 2.5, such height corresponds to a tunneling energy along the tubes equal to $J/h = 88\,\mathrm{Hz}$.

Assuming for the interacting BEC a Thomas-Fermi density distribution along each tube $\rho(z) = \rho_0(1 - \frac{z^2}{R_z^2})$ with $\rho_0 = \frac{3}{4}\frac{\bar{n}_{tube}}{R_z}$ determined by the normalization condition $\bar{n}_{tube} = \int \rho(z)dz$, we can calculate the average number of atoms per site as $\bar{n} = d \cdot \bar{\rho} = d \cdot \int \rho^2(z)dz = \frac{3}{5}\bar{n}_{tube}\frac{d}{R_z}$. With $R_z \simeq 13\,\mu\mathrm{m}$[6] we get an average site occupancy $\bar{n} \simeq 2.5$.

Secondary optical lattice. Along the same direction of the main lattice, we employ the Ti:Sapphire laser ($\lambda_2 = 859.6\,\mathrm{nm}$) to produce a disordering optical lattice with intensity, in units of recoil energy E_{r2}, up to $s_2 \simeq 1$. The inhomogeneous and non-periodic shift of the energy minima induced by

---

[4] If we approximate the Thomas-Fermi density distribution of the interacting BEC with an homogeneous distribution of radius $R_{TF} = \sqrt[3]{R_x R_y R_z}$, the number of tubes in the $x - y$ plane can be roughly estimated as $N_{tubes} \sim \frac{\pi R_x R_y}{d^2}$, d^2 being the surface area of each tube. With $d = \lambda_1/2 \approx 0.5\,\mu\mathrm{m}$ and $R_x \simeq R_y \approx 5\,\mu\mathrm{m}$ we get $N_{tubes} = 100$. A more accurate calculation, taking into account the parabolic shape of the Thomas Fermy density distribution, yields $N_{tubes} \approx 500$.

[5] We note that for all the measurements performed in this work, the regime of extreme interactions in 1D is never reached, since the maximun value of the interaction parameter in our case is $\gamma \simeq 0.5$.

[6] As we shall see in subsection 4.3.1, after loading the horizontal confining optical lattices which squeeze the tubes along the vertical direction, the Thomas-Fermi radius R_z along $\hat{z}$ results larger than those along the $\hat{x}$ and $\hat{y}$ directions previously used to calculate the average number of atoms $\bar{n}_{tube}$ in a tube.

the secondary lattice (see subsection 1.2.2) results in a separation of neighboring states in the quasi-periodic optical potential of $1/(\beta - 1) \simeq 4.2$ lattice sites (see figure 4.5).

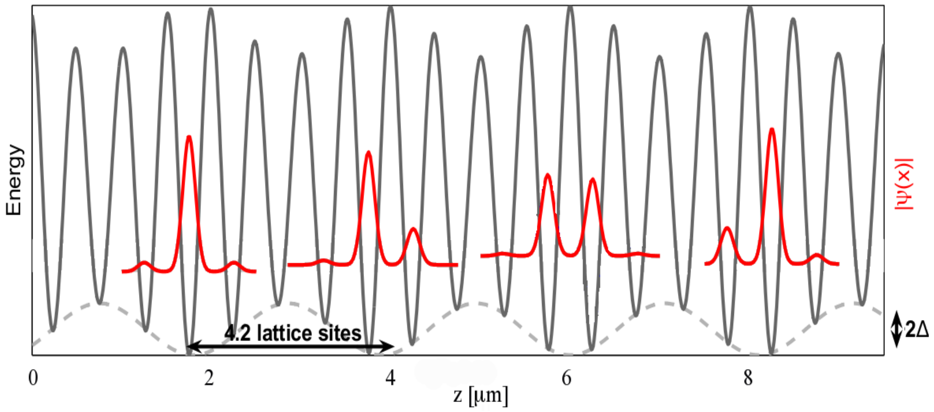

Figure 4.5: Quasi-periodic optical lattice obtained with $\beta = 1.238...$ and a disorder amplitude $\Delta/J \simeq 6$. The quasi-periodic optical potential is characterized by potential wells approximately every $1/(1 - \beta) \approx 4.2$ lattice sites, which arise from the beating of the two optical lattices (grey dashed line). In red, the lowest energy eigenstates of the lattice potential are shown. Note that the lower the site energy level, the larger the correspondent density distribution.

4.2.2 Calibration of the optical lattice height

In principle the height of the optical lattices could be calculated by using equation 1.16. However, the measurement of the actual intensity I_0 experienced by the atoms is affected by systematic errors: small misalignments of the lattice beams or not completely parallel polarizations may result in a different intensity from the one calculated. For this reason the height of the optical lattice is calibrated by using an interferometric in-situ technique relying on the so-called Raman-Nath diffraction.

The idea at the base of this phenomenon is simple: as a standard electromagnetic wave can be diffracted by a grating, in a symmetrical way a BEC, which can be thought of as a matter-wave, can be diffracted by an optical lattice. If a pulse of the laser beam forming the optical lattice is shined on the atoms for a time $T_{lat} \approx 10\mu$s short enough for them not to move along the lattice, the BEC gets diffracted and after a free expansion of $t_{tof} \simeq 20$ ms its density distribution shows a number of interference peaks that, as reported in figure 4.6, increases for increasing lattice height s. More quantitatively, it can be shown [75] that the lattice height s is related to the RMS size of the expanded BEC as follows:

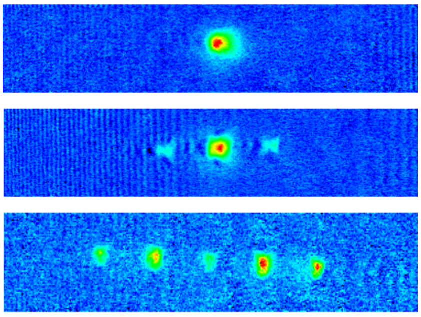

Figure 4.6: Absorption images of the BEC diffracted by a pulse of the optical lattice laser beam for increasing lattice heights ($s = 0, 5, 15$ from top to bottom). The images are taken after a free expansion of $t_{tof} = 16$ ms and with a pulse duration $T_{lat} = 20\mu$s. Note that the larger the optical lattice height s, the larger the number of diffraction peaks.

$$\sigma_{rms}^2 = \sigma_0^2 + \frac{1}{2}\left(\frac{kE_{rec}}{m}\, t_{tof}\, T_{lat}\right)^2 s^2 \tag{4.1}$$

where k is the laser beam wave number, m is the mass of the atoms and $E_{rec} = \frac{\hbar^2 k^2}{2m}$ is the recoil energy. Since the second moment σ_{rms}^2 of the density distribution and the width σ_0 of the central peak are computed, by using equation 4.1 one can get the optical lattice height s.

Besides indirectly measuring the optical lattice height s, this technique can also be used to perform an accurate alignment of the optical lattice beams on the atoms: the laser beams directions are finely adjusted in such a way that the number of diffraction peaks increases.

4.3 Measurements and data analysis

After firstly describing the experimental sequence by which the measurements are performed, in this section we will show a few significant images and the procedure adopted to analyze them in order to obtain the momentum distribution phase diagram reported in section 4.4.

4.3.1 Loading the BEC into the optical lattice

In figure 4.7 we report the temporal sequence with which the optical lattices are ramped up on the atoms. With reference to that figure, the BEC is produced in the optical trap at $t = 0$ with a scattering length $a = 180\,a_0$ (black curve). During the optical lattice loading sequence, the optical trap is kept constant in intensity, with an average trap frequency $\omega \simeq 70\,\text{Hz}$, and thus is not shown in the figure. We have experimentally verified that the heating that the BEC undergoes during the lattices loading is minimized if the magnetic field is linearly ramped down to 370 G, corresponding to a

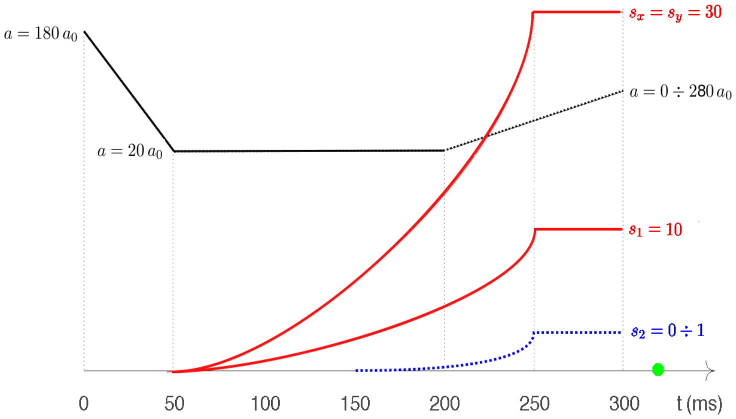

Figure 4.7: Temporal sequence for loading the BEC into the optical lattices. Note that while the confining and the main optical lattices (red curves) are always ramped up to the same values (respectively $s_x = s_y \simeq 30$ and $s_1 \simeq 10$), the final value of the scattering length a (black dotted line) and of the quasi-periodic optical lattice height s_2 (blue-dotted line) are suitable chosen depending on the measurements to be performed.

scattering length $a \simeq 20\,a_0$. At $t = 50\,\mathrm{ms}$, when the interaction of the BEC has thus been reduced, the height of the confining optical lattices (red curve) is adiabatically increased with exponential ramps up to $s_x = s_y \simeq 30$ in 200 ms. At the same time the main optical lattice (dotted red curve) is ramped up to $s_1 \simeq 10$. The exponential ramp of the disordering lattice (dotted blue curve) is performed in 100 ms in such a way that it reaches the desired final value ($s_2 = 0 \div 1$) at the same time of the others ($t = 250\,\mathrm{ms}$). All the optical lattices heights are then kept at their maximum value for 50 ms in order to adiabatically tune the scattering length to the desired value ($a = 0 \div 280\,a_0$) with a magnetic field ramp long enough (100 ms) while the atoms are already partially loaded into the optical lattices. At $t = 300\,\mathrm{ms}$, when the BEC is completely loaded into the optical lattices and the scattering length is set at its final value, the atoms are let free to expand for 16 ms (green dot) in order to perform measurements of momentum distribution, by suddenly switching off all the optical lattices and the trap laser beams.

4.3.2 Measurements of momentum distribution

We will now report the first measurements that we have performed with the experimental setup previously described. So far we have investigated the various zero-temperature quantum regimes described in Chapter 2 by studying the evolution of the momentum distribution of the system. Although other measurements will be needed, such as those related to transport or compressibility, the momentum distribution already gives a strong indication of the system phenomenology.

We switch off all the optical potentials and we let the atoms freely expand for 16 ms after which the density distribution in the coordinate space approaches the one in the momentum space. As described in subsection 2.2 (figure 2.2), if before switching off all the optical lattices the (Wannier) wavefunctions localized in each lattice site are phase-locked to each other, that is the system is a SF, then the Wannier functions interfere each other giving rise to sharp peaks in the density distribution along the direction of the free expansion. In particular, the distance between the peaks corresponds to the size of the Brillouin zone in the momentum distribution, that is $2\hbar\pi/d = 2\hbar k_1$, $d = \lambda_1/2$ being the spacing of the optical lattice generated by the laser beam with wavelength λ_1. Figure 4.8 on the left shows an image of a momentum density distribution in the SF regime taken without either interaction ($a \simeq 0$) or disorder ($s_2 = 0$). Despite the background noise due to the imaging system, three horizontal stripes arising from the matter-wave interference along the tubes direction ($\hat{z}$ direction) can be easily distinguished. By contrast, the broad distribution along the other direction is a clear evidence of the absence of phase coherence between the wavefunctions belonging to different potential tubes. As a comparison, the same figure on the right reports an image taken with the same parameters but without the confining optical lattices forming the potential tubes ($s_x = s_y = 0$). Such configuration corresponds to a system in a unique 3D vertical potential tube.

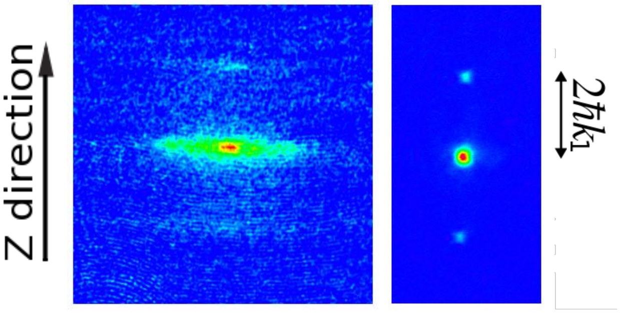

Figure 4.8: Images of momentum density distribution with scattering length $a \simeq 0$ and disordering optical lattice height $s_2 = 0$, taken with (**left**) and without (**right**) the confining optical lattices forming the potential tubes. Note the matter-wave interference fringes along the $\hat{z}$ direction.

As described in subsection 2.2, when the on-site interaction energy U is much larger than the tunneling energy J the system enters the MI phase. Figure 4.9 shows an image of a momentum density distribution in the MI regime taken at a large interaction value ($a \simeq 200\,a_0$) and without disorder ($s_2 = 0$). The loss of phase coherence shown in the broad momentum distribution also along the vertical direction is a proof of the fact that the system

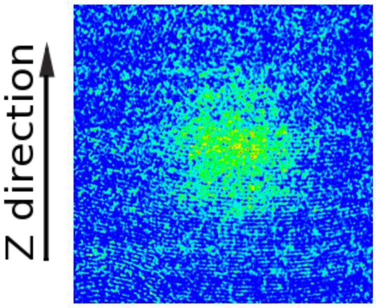

Figure 4.9: Image of momentum density distribution with scattering length $a \simeq 200$ and disordering optical lattice height $s_2 = 0$. Note that the phase coherence is lost also along the $\hat{z}$ direction.

is in an insulating phase.

For a full characterization of the competing roles of disorder and interaction, we have taken several series of images for varying interaction at several values of the disorder strength.

4.3.3 Data analysis

In order to study more quantitatively the crossovers between the SF and the insulating regimes, each image has been analyzed as follows: an intensity profile $P(k)$ along the $\hat{z}$ direction has been obtained by integrating the two-dimensional density distribution along the other direction (see figure 4.10). The linewidth of the central peak is then extracted by fitting it with a gaussian function (red curve)[7]. In the figure the intensity profiles $P(k)$ with the gaussian fits corresponding to both the SF (left) and insulating (right) 1D systems of the previous images are reported.

For a given disorder amplitude $\Delta \simeq \beta^2 s_2 E_{r2}/2$, several images at increasing scattering length a have been taken and analyzed. The width of the

---

[7] In general the shape of the wavefunction depends on the specific quantum phase; for example one expects an exponential shape in a localized phase, or a gaussian in an extended one. However, the measured wavefunction is the result of an average over the wavefunctions of the many potential tubes, each one, in turns, characterized by wavefunctions with in general different shapes for each lattice site. As a consequence we have heuristically fitted the density distributions with gaussian functions.

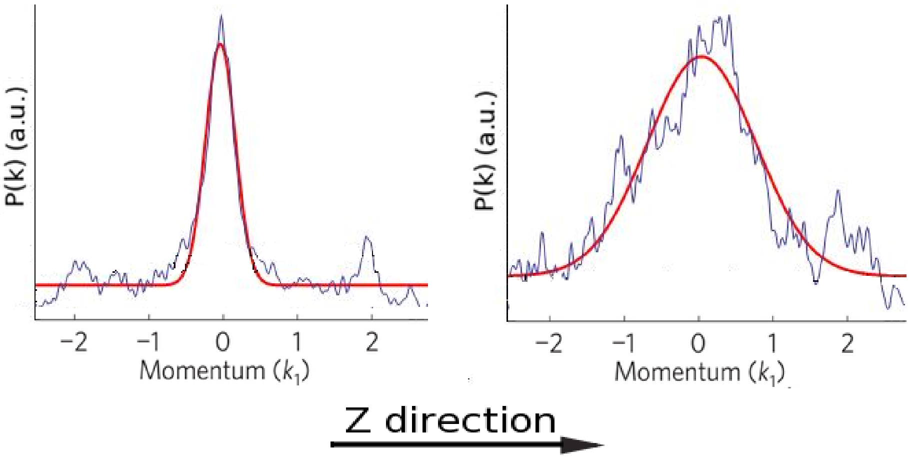

Figure 4.10: Intensity profiles $P(k)$ along the $\hat{z}$ direction of the two-dimensional density distributions of figures 4.8 (**left**) and 4.9 (**right**), as obtained by integrating along the other direction. A gaussian fit of the central peak – performed to extract its width – is shown in red.

momentum distribution central peak is reported in figure 4.11 as a function of the scattering length a obtained for two sets of measurements without disorder ($\Delta/J = 0$) and with $\Delta/J = 10.6$. In the case $\Delta/J = 0$ (blue dots), the momentum distribution broadens as the interaction increases. As previously said this corresponds to the crossover from the SF to the MI phase. At large disorder (red triangles), the width of the momentum distribution, which is large (about half the Brillouin zone) in the non interacting regime, decreases for small interactions and then increases again in the regime of strong interactions. Such behaviour at small a is in agreement with the delocalizing effects of a weak interaction on a disordered system discussed in subsection 2.3.1. The broadening at large a instead is compatible with the fact that the system enters the insulating BG phase, as discussed in subsection 2.4.

4.4 $\Delta - U$ Phase diagram

We have repeated the procedure described in the previous section for various values of Δ/J ranging from 0 to about 14. In order to perform a

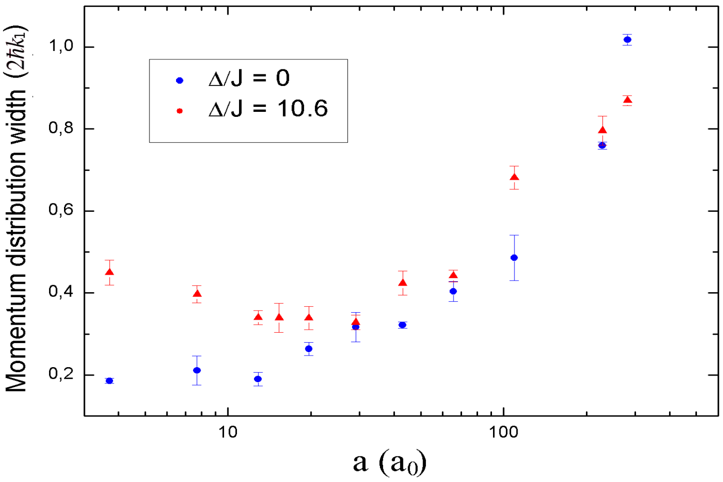

Figure 4.11: Width of the momentum distribution central peak as a function of the scattering length a obtained for two sets of measurements: at $\Delta/J = 0$ (blue dots), the momentum distribution broadens as the interaction increases (SF to MI crossover). At $\Delta/J = 10.6$ (red triangles) the momentum distribution firstly gets narrower (AG to SF crossover) and then broadens again (SF to BG crossover). The uncertainty bars are given by the standard deviation of several measurements performed at a given value of Δ/J and a.

more quantitative analysis, we have converted the scattering length into the interaction energy, by using the second of equations 2.5. In particular, for our experimental parameters we find a conversion $a/a_0 \approx 8\,U/J$.

From the fitted width of the momentum distribution one can build a two dimensional diagram: figure 4.12 shows the momentum distribution (central peak) obtained by interpolating all the sets of measurements, as a function of Δ/J and U/J. The plot is representative of the phase changes occurring in the BEC. At small disorders and interactions, the momentum distribution is narrow (blue zone) and the system is in a SF phase. At larger disorder and interaction values the momentum distribution progressively broadens (green, yellow and red zones) meaning that the system is becoming more and more insulating. Let us now analyze all the several quantum regimes of the phase diagram keeping in mind the theoretical description followed in chapter 2.

Let us thus first consider an ordered system, that is the case $\Delta/J = 0$.

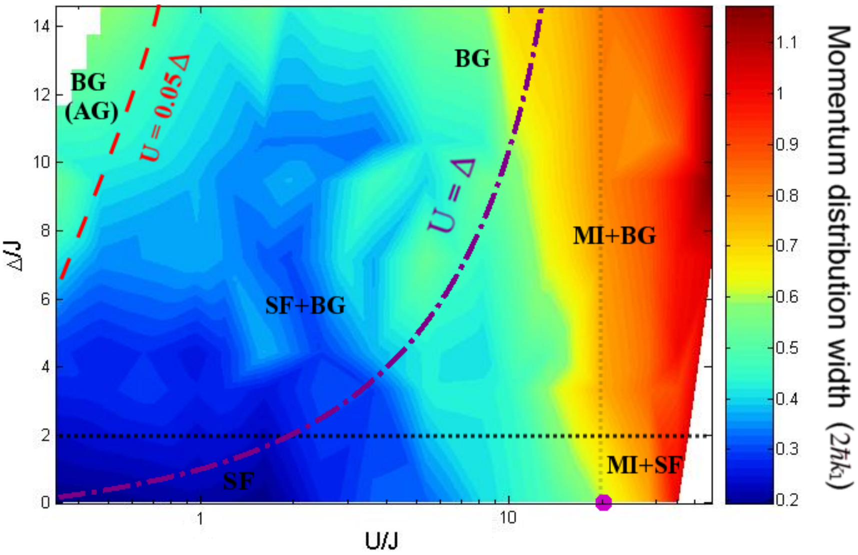

Figure 4.12: Phase diagram. The plot reports the interpolated momentum distribution (central peak), as a function of Δ/J and U/J. The blue zone corresponds to a narrow momentum distribution (SF phase), whereas the green, yellow and red zones correspond to progressively broader momentum distributions (insulating phases). The purple dot represents the center of the crossover between the SF an MI phases calculated assuming a site occupancy $n = 2$ in equation 4.2. The crossover between the BG (AG) phase and the SF one is represented, according to the screening argument [51], by the $U = 0.05\,\Delta$ curve. The $U = \Delta$ curve above which the full BG phase is expected to appear, is shown as well.

As already mentioned, the system undergoes a transition from a SF to a MI phase as the interaction becomes sufficiently large. As we can see, the threshold of the phase transition (which in the following we rather call more properly crossover) is not sharp and well defined but is instead spread over a wide range of U/J. The reason is that the system is not homogenous and as described in subsection 2.2.2, the transition to a MI domain with a small occupancy n occurs at lower interaction values than those required to enter a MI domain with a higher n (see figure 2.4). In particular for a 1D system[8] the transition occurs at the n-dependent critical value [61]:

$$(U/J)_c = 2n\left(1+\sqrt{1+1/n}\right)^2 \tag{4.2}$$

Since in our case we have calculated (subsection 4.2.1) a mean site occupation $\bar{n} = 2.5$, by using $n = 2$ as integer value, we get $\bar{U}_c \simeq 20J$. Such value is reported on the phase diagram as a purple dot.

Let us now consider the regime of weak interactions. In particular, at $U/J \simeq 0$, if we increase the disorder amplitude Δ (normalized by the interaction energy J), the system enters the Anderson localized phase (BG-AG) as discussed in subsection 2.3. We note that the disorder-induced localization in the AG-BG phase (green zone) is less strong than that one of the MI phase (yellow-red zone): while in the MI the localization of the single atom is by definition at the level of the lattice site, in the case of Anderson localization the wavefunction can be localized over more lattice sites, which, within the quasi-periodic lattice well, are almost degenerate in energy (see figure 4.5).

As expected, at a given large disorder Δ/J, the system delocalizes when we add a weak interaction. Such result is in good agreement with the experiments previously performed with a 3D system [50] and thus in agreement with the screening argument [51] discussed in subsection 2.3.1, according to which the AG-SF crossover occurs at an interaction energy $U = 0.05\,\Delta$ (red-dashed curve).

---

[8] In the general case, the factor 2 in equation 4.2 must be replaced by the number of neighboring sites.

Finally, let us consider the strong-interaction regime. Due to the inhomogeneity of the confined sample, when the system is strong interacting ($U > U_c$) and not disordered ($\Delta/J < 2$), the MI and SF phases coexist in the so called wedding cake structure (see figures 2.7 and 2.14a). For a given interaction energy U, if we move vertically on the phase diagram towards larger Δ/Js we note that the momentum distribution broadens, meaning that the SF component of the wedding cake structure is localizing due to the disorder. This fact seems to suggest that a mixture of MI and BG phases forms (see figure 2.14b). If we then move towards a disorder amplitude Δ larger than the interaction energy U (see the dot-dashed purple curve $U = \Delta$), then the system is expected to be in the full BG phase (see figure 2.14c) where the localization of the atoms is due only to the disorder whereas the effect of the interaction is negligible: for large Δ/J values our phase diagram shows a continuity (green zone) with the BG phase of the weak interaction regime.

In conclusion, the measurements of momentum distribution performed so far are compatible with the presence of both the MI and BG insulating quantum phases. The observed evolution of the momentum distribution width in the $\Delta - U$ plane is in qualitative agreement with both previous measurements of figure 2.13 and the theoretical phase diagrams of figure 2.15, if we take into account the inhomogeneity of our system. Further investigation is however needed to better characterize and distinguish the BG from the MI phase. In particular, an investigation of the compressibility and/or of the excitation spectrum of the system might provide a better distinction of the the two insulating phases in presence of strong disorder.

Conclusions

Ultracold atoms in disordered optical potentials are a powerful tool for studying the physical properties of condensed matter systems. While in nature both disorder and interaction are intrinsically present but quite not easily controllable, conversely, when working with Bose-Einstein condensates in optical lattices, such properties can be manipulated in a controlled way. In particular, our experimental setup, thanks to both a 3D optical lattice and a broad Feshbach resonance of ^{39}K, allows us to study the interplay between disorder and interaction with a high degree of control.

In this thesis work we reported the results of the first investigation of the phase diagram describing the behaviour of a Bose-gas in a disordered system, in a regime of both weak and strong interactions. With regard to the weak interaction regime, such phase diagram confirms the results obtained in experiments previously performed at our laboratory, according to which an insulating disordered system can be delocalized by means of a weak interaction.

As for the strong-interaction regime, the phase diagram shows that the insulating features of a disordered system are qualitatively in agreement with those predicted by the theory for a Bose-Glass. Nevertheless, due to the inhomogeneity of the BEC sample in the confining trap, making a comprehensive reference to the theory is a difficult task. As a matter of fact our measurements are a first attempt to characterize the mixture of the diverse quantum phases present in an inhomogeneous system. In particular, the Bose-Glass phase, which is characterized by two features, that is being insulating and compressible, still has to be largely investigated. For the former feature, the transport properties of the system might be verified by diffusion measurements of the BEC into the optical lattice. As for the latter, measurements of compressibility would be determinant to characterize the system and in particular to distinguish the Bose-glass phase from the Mott-insulator one.

Appendices

A Mechanics designs

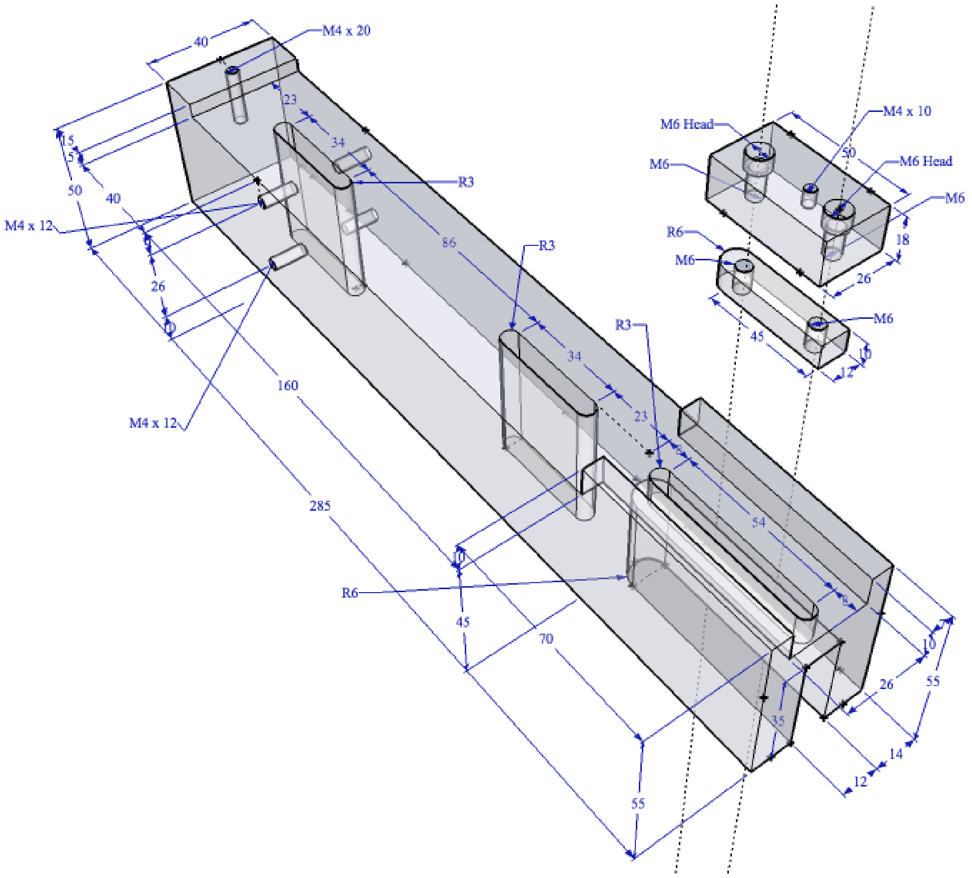

Figure 13: Design of the Fabry-Pérot interferometer mount.

The design of the Fabry-Pérot interferometer mount is shown in figure 13. The mount, 285 mm long, is made to host two equal spherical mirrors with a radius of curvature of 200 mm: while a mirror sits at one edge (top left) and can not move, the second one sits on an extra mount (top right) which has the possibility to slide along a runner in order to provide the desired configuration. Note that the extra mount is linked - by means of two screws which pass through the 54 mm long slit - to the small bar underneath it which allows the extra mount to be fasten when it sits at the desired position.

The two 34 mm long slits allow the mount to be clamped to the breadboard and the $M4$ holes - two for each side - are made to fasten (on the most convenient side) the BNC connector of the cables coming from the piezo-transducer the mirror is mounted on.

The design of the Laser pointer mount is shown in figure 14. The mount

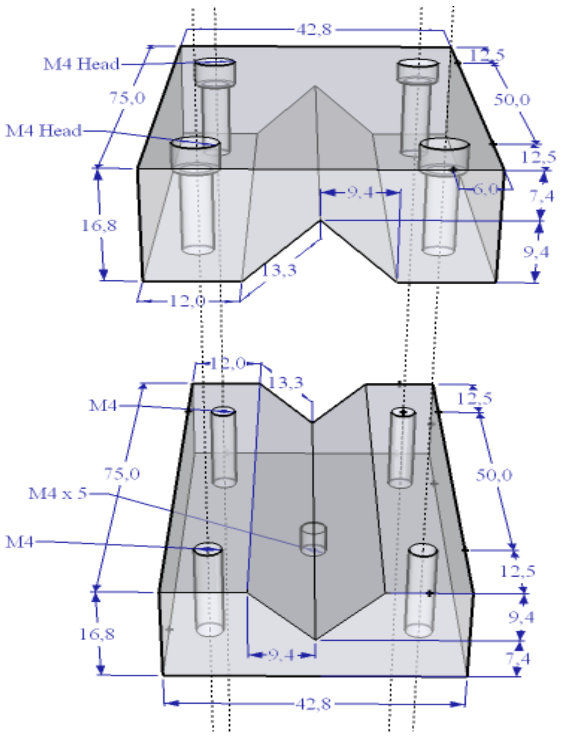

Figure 14: Design of the laser pointer mount.

is made to clamp the laser pointer in the horizontal position at the proper working height (77 mm) taking into account the height (60.2 mm) of the mirror post which has been used to hold the mount (see the $M4 \,\mathrm{x}\, 5$ hole underneath at the center). Insulating tape (underneath) and 3 mm high rubber (above) surrounding the laser pointer have also been used to insulate it and give more mechanical stability.

B Electronics circuit layouts

.

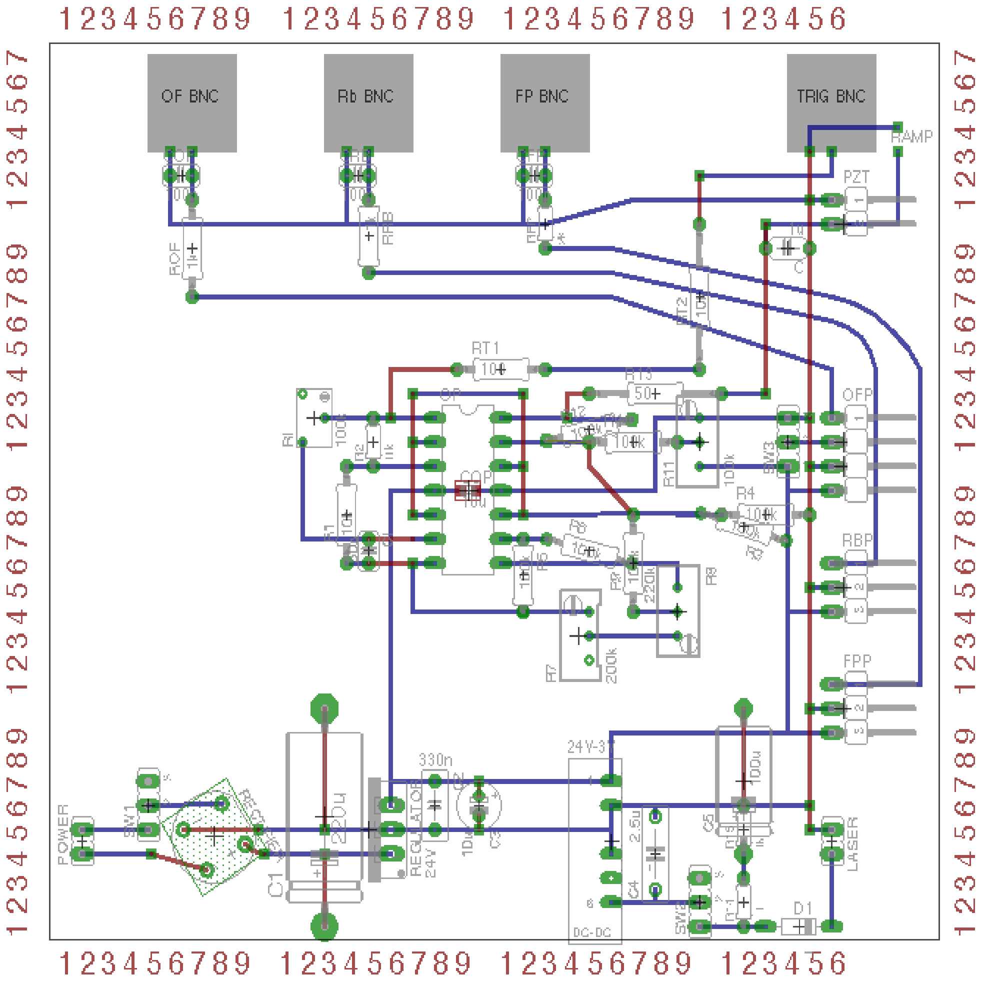

Figure 15: Layout of the electronic circuit.

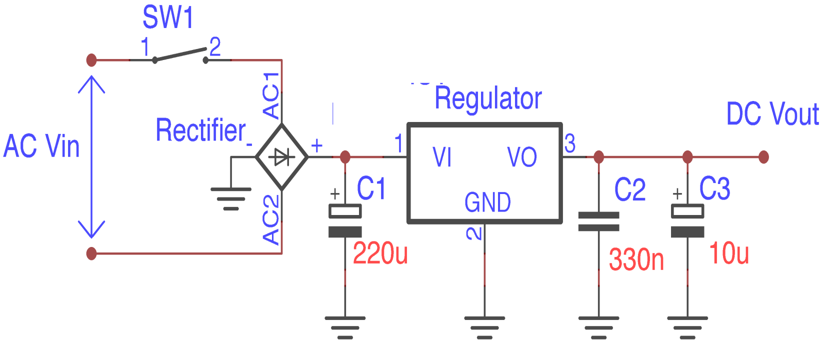

Figure 16: Circuit schematic of the AC-DC converter.

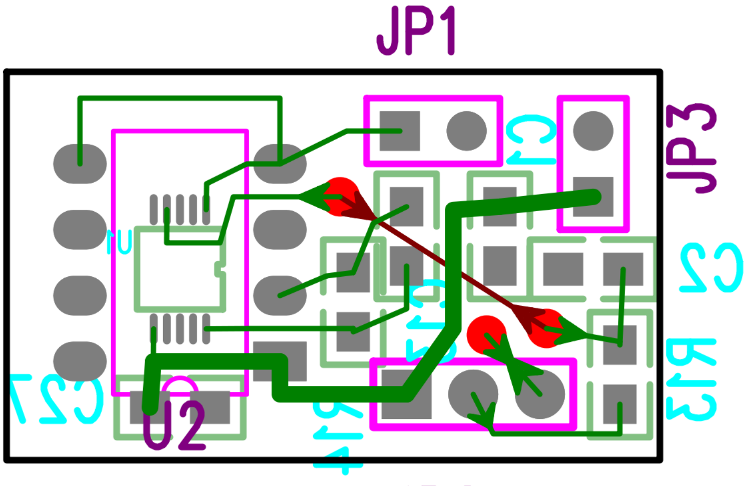

Figure 17: Circuit layout of the photodetector with adjustable sensitivity.

BIBLIOGRAPHY

[1] A. Einstein, Sitzber. *Kgl. preuss. Akad. Wiss.*, 261 (1924); *ibidem*, **3** (1925).

[2] S. N. Bose, *Z. Phys.* **26**, 178 (1924).

[3] M. H. Anderson, J. R. Ensher, M. R. Matthews, C. E. Wieman and E. A. Cornell, *Science* **269**, 198 (1995).

[4] W. Ketterle, D. S. Dur fee, and D. M. Stamper-Kurn. *Making, probing and understanding Bose-Einstein condenstates*, Proceedings of the Inter national School of Physics "Enrico Fermi", course CXL (IOS Press, 1999).

[5] L. D. Landau and E. M. Lifshitz, *Statistical Physics*, Pergamon Press, Oxford,(1969).

[6] L. Fallani, *Bose-Einstein Condensates in Optical Lattices*, PhD Thesis, University of Florence (2002).

[7] F. Dalfovo, S. Giorgini, L. Pitaevskii and S. Stringari, *Theory of Bose-Einstein condensation in trapped gases*, Rev. Mod. Phys. **71**, 463 (1999)

[8] J. Giacomelli, *Localizzazione di un condensato di Bose-Einstein in potenziali ottici*, Diploma Thesis, University of Florence (2007).

[9] E. P. Gross, *Nuovo Cimento* **20**, 454 (1961).

[10] E. P. Gross, *J.Math. Phys.* **4**, 195 (1963).

[11] L. P. Pitaevskii, *Zh.Eksp.Teor.Fiz.*, **40**, 646 (1961); *Sov.Phys.JETP* **13**, 451 (1961).

[12] H. Feshbach, *A Unified Theory of Nuclear Reactions*, Ann. Phys. **5**, 357 (1958).

[13] H. Feshbach, *A Unified Theory of Nuclear Reactions. II*, Ann. Phys. **19**, 287 (1962).

[14] U. Fano, *Sullo spettro di assorbimento dei gas nobili presso il limite dello spettro d'arco*, Nuovo Cimento **12**, 156 (1935).

[15] S. Inouye, M. R. Andrews, J. Stenger, H. J. Miesner, D. M. Stamper-Kurn, and W. Ketterle, *Observation of Feshbach resonances in a Bose-Einstein condensate*, Science **392**, 151 (1998).

[16] S. L. Cornish, N. R. Claussen, J. L. Roberts, E. A. Cornell, and C. E. Wieman, *Stable* ^{85}*Rb Bose-Einstein Condensates with Widely Tunable Interactions*, Phys. Rev. Lett. **85**, 1795 (2000).

[17] C. Chin, V. Vuletić, A. J. Kerman, and S. Chu, *High Resolution Feshbach Spectroscopy of Cesium*, Phys. Rev. Lett. **85**, 2717 (2000).

[18] C. Chin, R. Grimm, P. Julienne, and E. Tiesinga, *Feshbach Resonances in Ultracold Gases*, eprint arXiv:0812.1496 (2008).

[19] A. J. Moerdijk, B. J. Verhaar, and A. Axelsson, *Phys. Rev. A* **51**, 4852 (1995).

[20] C. D'Errico, *Anderson localization of a weakly interacting Bose-Einstein condensate*, PhD Thesis, University of Florence (2009).

[21] C. Cohen-Tannoudji, *Nobel lecture* **70**, 707 (1998).

[22] R. Grimm, M. Weidemüller, and Y. B. Ovchinnikov, *Optical dipole traps for neutral atoms*, Advances in Atomic, Molecular and Optical Physics **42**, 95 (2000).

[23] I. Bloch, Ultracold quantum gases in optical lattices, *Nature Physics* **1**, 23 - 30 (2005)

[24] C. Kittel, *Quantum Theory of Solids*, John Wiley and Sons, New York, (1963).

[25] N. W. Ashcroft and N. D. Mermin, *Solid State Physics*, Saunders College Publishing (1976).

[26] W. S. Bakr, *Microscopic Studies of Quantum Phase Transitions in Optical Lattices*, PhD thesis, Harvard University (2011).

[27] P. A. Lee and T. V. Ramakrishnan, *Rev. Mod. Phys.* **57**, 287 (1985).

[28] L. Fallani, C. Fort, and M. Inguscio, *Bose-Einstein condensates in disordered potentials*, eprint arXiv:0804.2888 (2008).

[29] J. W. Goodman, *Speckle Phenomena in Optics: Theory and Applications*, Roberts and Company Publishers, (2007).

[30] J. W. Goodman, J. C. Dainty *Laser speckle and related phenomena*, Springer-Verlag, Berlin, (1975).

[31] M. Francon, *La Granularité Laser (speckle) et ses applications en optique*, Masson, Paris, (1978).

[32] S. Aubry and G. André, *Ann. Israel Phys. Soc.* **3**, 133 (1980).

[33] D. R. Grempel, S. Fishman, and R. E. Prange, *Phys. rev. Lett.* **49**, 833 (1982);

[34] V. Guarrera, L. Fallani, J. E. Lye, C. Fort and M. Inguscio, *New J. of Phys.* **9**, 107 (2007).

[35] M. P. A. Fisher, P. B. Weichman, G.Grinstein, and D. S. Fisher, *Phys.Rev. B* **40**, 546 (1989).

[36] D. Jacksch, C. Bruder, J. I. Cirac, C. W. Gardiner and P. Zoller, *Phys. Rev. Lett.* **81**, 3108 (1998)

[37] G. Roux, T. Barthel, I. P. McCulloch, C. Kollath, U. Schollwöck and T. Giamarchi, *Phys. Rev. A* **78**, 023628 (2008).

[38] M. Greiner, O. Mandel, T. Esslinger, T. W. Hansch and I. Bloch, *Nature* **415**, 39 (2002).

[39] W. S. Bakr, A. Peng, M. E. Tai, R. Ma, J. Simon, J. I. Gillen, S. Folling, L. Pollet, and M. Greiner, *Probing the Superuid to Mott Insulator Transition at the Single Atom Level*, arXiv:1006.0754v1 (2010).

[40] C. Fort, L. Fallani, V. Guarrera, J. Lye, M. Modugno, D.S. Wiersma, and M. Inguscio, *Phys. Rev. Lett.* **95**, 170410 (2005).

[41] I. Bloch, J. Dalibard, and W. Zwerger, Many-body physics with ultracold gases, *Rev. Mod. Phys.* **80**, 885 (2008).

[42] P. W. Anderson, *Absence of Diffusion in Certain Random Lattices*, Phys. Rev. **109**, 1492 (1958).

[43] B. Kramer, and A. MacKinnon, *Rep. Prog. Phys.* **56**, 1469 (1993).

[44] G. Roati, M. Zaccanti, C. D'Errico, J. Catani, M. Modugno, A. Simoni, M. Inguscio, and G. Modugno, *Bose-Einstein Condensate with Tunable Interactions*, Phys. Rev. Lett. **99**, 010403 (2007).

[45] C. Aulbach, A. Wobst, G. L. Ingold, P. Hanggi, and I. Varga, *New J. Phys.* **6** (2004).

[46] E. Abrahams, P. W. Anderson, D. C. Licciardello, and T. V. Ramakrishnan, *Phys. Rev. Lett.* **42**, 673 (1979).

[47] G. Roati, C. D'Errico, L. Fallani, M. Fattori, C. Fort, M. Zaccanti, G. Modugno, M. Modugno, and M. Inguscio, *Nature* **453**, 895 (2008).

[48] J. Zhong *et al.*, *Phys. Rev. Lett.* **86**, 2485 (2001).

[49] P. Pedri, *et al.*, *Phys. Rev. Lett.* **87** 220401 (2001).

[50] B. Deissler, M. Zaccanti, G. Roati, C. D'Errico, M. Fattori, M. Modugno, G. Modugno and M. Inguscio, *Nature Phys.* **6**, 354 (2010).

[51] L. D. K. K. and J. M. F. Gunn *J. Phys.: Condens. Matter* **2** 7753-7768 (1990).

[52] R. T. Scalettar, G. G. Batrouni and G. T. Zimanyi, *Phys. Rev. Lett.* **66**, 3144-3147 (1991).

[53] B. Damski , J. Zakrewski, L. Santos, P. Zoller and M. Lewenstein *Phys. Rev. Lett.* **991**, 080403 (2003).

[54] P. Lugan, D. Clément, P. Bouyer, A. Aspect, M. Lewenstein and L. Sanchez-Palencia, *Phys. Rev. Lett.* **98**, 170403 (2007).

[55] L. Fontanesi, M. Wouters and V. Savona, *Phys. Rev. Lett.* **103**, 030403 (2009).

[56] G. Modugno, C. D'Errico, B. Deissler, E. Lucioni, M. Modugno, M. Moratti, G. Roati, L. Tanzi, M. Zaccanti, and M. Inguscio, *Exploring disorder physics with Bose-Einstein condensates*, (2011).

[57] L. Fallani, J. E. Lye, V. Guarrera, C. Fort, and M. Inguscio, *Ultracold Atoms in a Disordered Crystal of Light: Towards a Bose Glass*, Phys. Rev. Lett. **98**, 130404 (2007).

[58] M. Girardeau, *J. Math. Phys.* **1**, 516 (1960).

[59] E. H. Lieb, W. Liniger, *Phys. Rev.* **130**, 1605 (1963).

[60] B. Paredes et al., *Nature* **429**, 277 (2004)

[61] C. J. Pethick, H. Smith, *Bose-Einstein condensation in Diluite Gases*, Cambridge University Press (2001).

[62] F. L. Pedrotti, *Introduction to optics*, Pearson international, 2007

[63] K. Kernera, S. M. Rochestera, V. V. Yashchuka, and D. Budkera, *Variable Free Spectral Range Spherical Mirror Fabry-Perot Interferometer*, University of California at Berkeley.

[64] H. Wang, A. N. Nikolov, J. R. Ensher, P. L. Gould, E. E. Eyler, and W. C. Stwalley, *Ground-state scattering lengths for potassium isotopes determined by double-resonance photoassociative spectroscopy of ultracold*, Phys. Rev. A **62**, 052704 (2000).

[65] T. Loftus, C. A. Regal, C. Ticknor, J. L. Bohn, and D. S. Jin, *Resonant Control of Elastic Collisions in an Optically Trapped Fermi Gas of Atoms*, Phys. Rev. Lett. **88** 173201 (2002).

[66] Y. Kagan, E. L. Surkov, and G. V. Shlyapnikov, *Evolution and Global Collapse of Trapped Bose Condensates under Variations of the Scattering Length*, Phys. Rev. Lett. **79**, 2604 (1997).

[67] C. A. Sackett, H. T. C. Stoof, and R. G. Hulet, *Growth and Collapse of a Bose-Einstein Condensate with Attractive Interactions*, Phys. Rev. Lett. **80**, 2031 (1998).

[68] M. Ueda and A. J. Leggett, *Macroscopic Quantum Tunneling of a Bose-Einstein Condensate with Attractive Interaction*, Phys. Rev. Lett. **80**, 1576 (1998).

[69] L. Khaykovich, F. Schreck, G. Ferrari, T. Bourdel, J. Cubizolles, L. D. Carr, Y. Castin, and C. Salomon, *Formation of a Matter-Wave Bright Soliton*, Science **296**, 1290 (2002).

[70] M. Prevedelli, F. S. Cataliotti, E. A. Cornell, J. R. Ensher, C. Fort, L. Ricci, G. M. Tino, and M. Inguscio, *Trapping and cooling of potassium*

isotopes in a double-magneto-optical-trap apparatus, Phys. Rev. A **59**, 886 (1999).

[71] L. De Sarlo, P. Maioli, G. Barontini, J. Catani, F. Minardi, and M. Inguscio, *Collisional properties of sympathetically cooled*, Phys. Rev. A **75**, 022715 (2007).

[72] F. Ferlaino, C. D'Errico, G. Roati, M. Zaccanti, M. Inguscio, and G. Modugno, *Feshbach spectroscopy of a K-Rb atomic mixture*, Phys. Rev. A **73**, 040702(R) (2006).

[73] A. Simoni, M. Zaccanti, C. D'Errico, M. Fattori, G. Roati, M. Inguscio, and G. Modugno *Near-threshold model for ultracold KRb dimers from interisotope Feshbach spectroscopy*, Phys. Rev. A **77**, 052705 (2008).

[74] G. Roati, *Quantum degenerate Potassium-Rubidium mixtures*, PhD Thesis, University of Trento (2003).

[75] F. Ferlaino, *Atomic Fermi gases in an optical lattice*, PhD Thesis, University of Florence (2004).

[76] E. de Mirandes, *Bloch oscillations of ultracold atoms*, PhD thesis, University of Florence (2005).

[77] C. D'Errico, *Osservazione di Risonanze di Fano-Feshbach in miscele atomiche K-Rb*, Master Thesis, University of Florence (2005).

[78] M. Zaccanti, *Tuning of the interactions in ultracold K-Rb quantum gases*, PhD thesis, University of Florence (2007).

[79] E. L. Raab, M. Prentiss, Alex Cable, Steven Chu, and D. E. Pritchard, *Trapping of Neutral Sodium Atoms with Radiation Pressure*, Phys. Rev. Lett. **59**, 2631 (1987).